

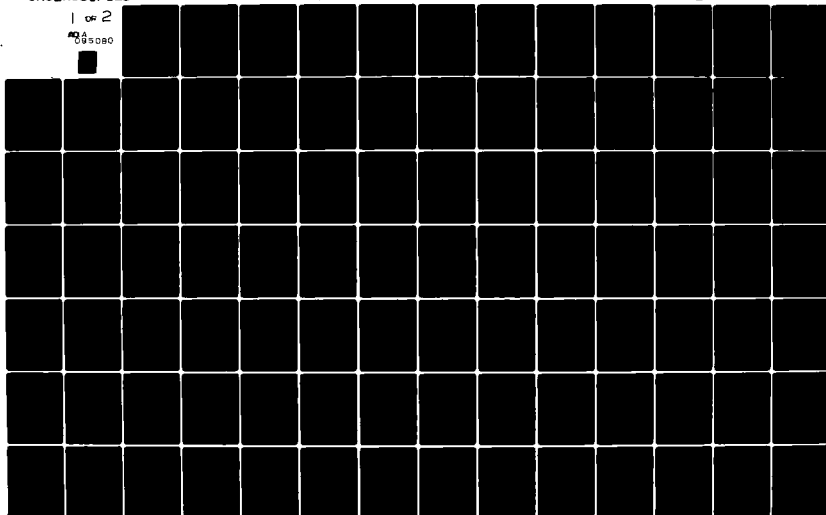
AD-A095 080

PENNSYLVANIA STATE UNIV UNIVERSITY PARK APPLIED RESE--ETC F/G 21/5  
COUPLING OF UNSTEADY LIFT TO ACOUSTIC DUCT MODES IN AN AXIAL FL--ETC(U)  
SEP 80 C S LEE  
N00024-79-C-6083  
ARL/PSU/TM-80-188  
NL

UNCLASSIFIED

1 of 2

ADA  
095080



AD A095080

LEVEL

12

COUPLING OF UNSTEADY LIFT TO ACOUSTIC DUCT  
MODES IN AN AXIAL FLOW FAN

C. S. Lee

Technical Memorandum

File No. TM 80-188

Sep 1980

Contract No. N00024-79-C-6043

Copy No. 1615

DTIC

ELECTE

FEB 18 1981

E

The Pennsylvania State University  
APPLIED RESEARCH LABORATORY  
Post Office Box 30  
State College, PA 16801

Approved for Public Release  
Distribution Unlimited

NAVY DEPARTMENT

NAVAL SEA SYSTEMS COMMAND

DDC FILE COPY

81 2

17 077

SECURITY CLASSIFICATION OF THIS PAGE (When Data Entered)

REPORT DOCUMENTATION PAGE		READ INSTRUCTIONS BEFORE COMPLETING FORM
1. REPORT NUMBER TM 80-188	2. GOVT ACCESSION NO. AD-A095 080	3. RECIPIENT'S CATALOG NUMBER
4. TITLE (and Subtitle)  COUPLING OF UNSTEADY LIFT TO ACOUSTIC DUCT MODES IN AN AXIAL FLOW FAN		5. TYPE OF REPORT & PERIOD COVERED  Technical Memorandum
		6. PERFORMING ORG. REPORT NUMBER
7. AUTHOR(s)  C. S. Lee		8. CONTRACT OR GRANT NUMBER(s)  N00024-79-C-6043
9. PERFORMING ORGANIZATION NAME AND ADDRESS Applied Research Laboratory Post Office Box 30 State College, PA 16801		10. PROGRAM ELEMENT, PROJECT, TASK AREA & WORK UNIT NUMBERS
11. CONTROLLING OFFICE NAME AND ADDRESS Naval Sea Systems Command Department of the Navy Washington, DC 20362		12. REPORT DATE September 15, 1980
		13. NUMBER OF PAGES 131
14. MONITORING AGENCY NAME & ADDRESS (if different from Controlling Office)		15. SECURITY CLASS. (of this report)  UNCLASSIFIED
		15a. DECLASSIFICATION DOWNGRADING SCHEDULE
16. DISTRIBUTION STATEMENT (of this Report)  Approved for Public Release. Distribution unlimited. Per NAVSEA - October 15, 1980		
17. DISTRIBUTION STATEMENT (of the abstract entered in Block 20, if different from Report)		
18. SUPPLEMENTARY NOTES		
19. KEY WORDS (Continue on reverse side if necessary and identify by block number) axial flow fan, unsteady lift, acoustic pressure		
20. ABSTRACT (Continue on reverse side if necessary and identify by block number) By using distortion screens, plane (0,0) and spinning (-1,0) acoustic modes were generated in an axial flow research fan. The unsteady lift on the rotor blade and the acoustic pressure along the duct were measured simultaneously by a lift gage sensor and a flush-mounted microphone respectively. The screens were calibrated by circumferentially traversing a five-hole probe. The typical background noise of unsteady lift and acoustic pressure was well below the desired signals. A phase-locked ensemble averaging technique was used to obtain the amplitude and phase of the periodic unsteady signals.		

20. The measured acoustic pressures were decomposed into modal pressures and compared with theoretical prediction; a reasonable trend was reached, but the discrepancies were large. The unsteady lift measurements of (-1,0) mode generation agreed with predictions except near the cutoff frequency indicating a back-reaction effect of considerable magnitude. The predictions overestimated the unsteady lift for the condition of "aerodynamic resonance" when the plane wave was generated.

## ABSTRACT

By using distortion screens, plane (0,0) and spinning (-1,0) acoustic modes were generated in an axial flow research fan. The unsteady lift on the rotor blade and the acoustic pressure along the duct were measured simultaneously by a lift gage sensor and a flush-mounted microphone respectively. The screens were calibrated by circumferentially traversing a five-hole probe.

The typical background noise of unsteady lift and acoustic pressure was well below the desired signals. A phase-locked ensemble averaging technique was used to obtain the amplitude and phase of the periodic unsteady signals.

The measured acoustic pressures were decomposed into modal pressures and compared with theoretical prediction; a reasonable trend was reached, but the discrepancies were large. The unsteady lift measurements of (-1,0) mode generation agreed with predictions except near the cutoff frequency indicating a back-reaction effect of considerable magnitude. The predictions overestimated the unsteady lift for the condition of "aerodynamic resonance" when the plane wave was generated.

Accession For	
NTIS GRA&I	<input checked="" type="checkbox"/>
DTIC TAB	<input type="checkbox"/>
Unannounced	<input type="checkbox"/>
Justification	<input type="checkbox"/>
By	
Distribution	
Availability Codes	
Avail and/or	
Dist	Special
A	

## TABLE OF CONTENTS

	<u>Page</u>
ABSTRACT. . . . .	iii
LIST OF FIGURES . . . . .	vii
LIST OF TABLES. . . . .	x
LIST OF SYMBOLS . . . . .	xi
ACKNOWLEDGMENTS . . . . .	xv
I. INTRODUCTION. . . . .	1
1.1 Introduction and Previous Investigation. . . . .	1
1.2 Previous Theoretical Work. . . . .	5
1.2.1 Unsteady Lift . . . . .	6
1.2.2 Acoustic Generation . . . . .	8
1.2.3 Acoustic Transmission . . . . .	8
1.3 Previous Experimental Work . . . . .	8
1.4 Present Work . . . . .	10
II. EXPERIMENTAL ASPECTS. . . . .	12
2.1 Introduction . . . . .	12
2.2 Apparatus. . . . .	12
2.3 Instrumentation. . . . .	19
2.4 Calibration. . . . .	23
2.4.1 Five-Hole Probe Calibration . . . . .	23
2.4.2 Strain Gage Calibration . . . . .	23
2.4.3 Microphone Calibration. . . . .	23
2.4.4 Signal Processor Calibration. . . . .	27
2.5 Measurement. . . . .	28

	<u>Page</u>
2.6 Experimental Accuracy and Repeatability . . . . .	34
2.6.1 Velocity Survey . . . . .	34
2.6.2 Unsteady Lift and Pressure Measurements. . .	34
2.7 Data Validity . . . . .	35
III. RESULTS AND COMPARISON WITH THEORY . . . . .	39
3.1 The Sound Field in a Duct . . . . .	39
3.2 Aerodynamic Lift Prediction . . . . .	42
3.3 Coupling of Unsteady Lift to Acoustic Modal Pressures	43
3.4 Comparison of Experimental Results with Theoretical Predictions . . . . .	49
3.4.1 Distortion Screens . . . . .	49
3.4.2 Unsteady Lift. . . . .	54
3.4.3 Acoustic Pressure. . . . .	64
IV. CONCLUSIONS AND RECOMMENDATIONS. . . . .	77
4.1 Conclusions . . . . .	77
4.2 Recommendations . . . . .	79
REFERENCES . . . . .	81
APPENDIX A: DESIGN OF THE ROTOR . . . . .	85
A.1 Mean Radius . . . . .	85
A.1.1 Velocity Diagram . . . . .	85
A.1.2 Number of Rotor Blades . . . . .	86
A.1.3 Blade Geometry . . . . .	86
A.1.4 Stall Limit. . . . .	87
A.2 Spanwise Variation. . . . .	87
APPENDIX B: SELECTION OF MICROPHONE LOCATIONS . . . . .	89
APPENDIX C: DESIGN OF DISTORTION SCREENS. . . . .	91
APPENDIX D: SIGNAL PROCESSING CONSIDERATIONS. . . . .	96

Page

APPENDIX E: COMPARISON OF NOISE PREDICTION SCHEME AND EXACT SOLUTION TO SOUND GENERATION EQUATION. . . . .	99
APPENDIX F: THE EFFECT OF REFLECTION ON ACOUSTIC MODE DECOMPOSITION. . . . .	102
F.1 Reflection of the Duct Opening . . . . .	102
F.2 Reflection of the Rotor Blade Row . . . . .	104
F.3 Modal Decomposition with Reflection. . . . .	109
APPENDIX G: CALIBRATION OF UNSTEADY FORCE GAGE . . . . .	111



## LIST OF FIGURES

<u>Figure</u>	<u>Page</u>
1. Transmission of the Acoustic Duct Modes . . . . .	4
2. General Disturbance Flow in a Cascade . . . . .	7
3. Schematic Diagram of Fan Noise Mechanism and Experimental Measurement. . . . .	13
4. Instrumented Rotor Blade. . . . .	14
5. Axial Flow Research Fan . . . . .	15
6. Location of Disturbance Screen, Rotor, and Microphone .	18
7. Instrumentation Block Diagram for Velocity Measurement.	20
8. Instrumentation Block Diagram for Unsteady Pressure Measurement . . . . .	22
9. Calibration Plot of the Five-Hole Probe . . . . .	24
10. Dynamic Response of the Lift Gage . . . . .	25
11. Spectrum of Microphone Calibration. . . . .	26
12. Correlation of $\Delta P_s / \rho$ and $\bar{V}_x$ for Distortion Screens. . .	30
13. Spatial Relation for Phase Angle Measurement. . . . .	32
14. Background Noise of Microphone Measurement. . . . .	36
15. Background Noise of Unsteady Lift Gage Measurement. . .	37
16. Resolution of Unsteady Lift to Acoustic Wave Front of Higher Order Modes . . . . .	45
17. Flow Chart of Acoustic Modal Pressure Prediction. . . .	46
18. Fourier Harmonics of Nine-Cycle Screen versus Mean Axial Velocity. . . . .	47
19. Fourier Harmonics of Ten-Cycle Screen versus Mean Axial Velocity. . . . .	48
20. Amplitudes of Fourier Harmonics of Nine-Cycle Screen. .	50

<u>Figure</u>	<u>Page</u>
21. Amplitudes of Fourier Harmonics of Ten-Cycle Screen. .	51
22. Decay Rate of Modal Pressure in the Axial Flow Research Fan (AFRF) . . . . .	53
23. Typical Spectrum of Lift Gage Measurement (Function 4)	56
24. Typical Wave Form of Lift Gage Measurement (Function 12)	57
25. Typical Fourier Harmonics of Lift Gage Measurement (Function 13). . . . .	58
26. Unsteady Lift of Nine-Cycle Screen versus Rotor Speed ( $\phi = 0.70$ ) . . . . .	59
27. Unsteady Lift of Nine-Cycle Screen versus Rotor Speed ( $\phi = 0.56$ ) . . . . .	60
28. Unsteady Lift of Ten-Cycle Screen versus Rotor Speed ( $\phi = 0.70$ ) . . . . .	61
29. Unsteady Lift of Ten-Cycle Screen versus Rotor Speed ( $\phi = 0.56$ ) . . . . .	62
30. Typical SPL Measurements versus Rotor Speed. . . . .	65
31. Decomposed Modal Pressure of Nine-Cycle Screen ( $\phi = 0.70$ )	69
32. Decomposed Modal Pressure of Nine-Cycle Screen ( $\phi = 0.56$ )	70
33. Decomposed Modal Pressure of Ten-Cycle Screen ( $\phi = 0.70$ )	71
34. Decomposed Modal Pressures of Ten-Cycle Screen ( $\phi = 0.56$ )	72
35. Reflection Coefficient of Duct Opening . . . . .	74
C1 Theoretical and Designed Variation of Resistance Coefficient for Nine-Cycle Screen. . . . .	94
C2 Theoretical and Designed Variation of Resistance Coefficient for Ten-Cycle Screen . . . . .	95
D1 Effect of Tracking Ratio Tuner Divider N on Spectrum Resolution . . . . .	98
F1 Steady State Wave Form after Reflections for Plane Wave	107
F2 Steady State Wave Form after Reflections for (1,0) Mode	108
G1 Instrumentation of Dynamic Calibration of Unsteady Force Gage . . . . .	113

<u>Figure</u>		<u>Page</u>
G2	Dynamic Calibration of Unsteady Force Gage . . . . .	114
G3	Instrumentation of Static Calibration of Unsteady Force Gage . . . . .	115
G4	Static Response of Unsteady Force Gage . . . . .	116

## LIST OF TABLES

<u>Table</u>	<u>Page</u>
I Geometric Parameters of Nine-Bladed Cambered Rotor. . .	17
II Test Matrix of Unsteady Pressure Measurements . . . . .	31
III Unsteady Lift Coefficients of the Test Cases. . . . .	55
IV Sound Pressure Level Measurements — Nine-Cycle Distortion Screen . . . . .	66
V Sound Pressure Level Measurements — Ten-Cycle Distortion Screen . . . . .	67

## LIST OF SYMBOLS

<u>Symbol</u>	<u>Description</u>
A	amplitude of Fourier harmonic
a	coefficient of wave number in axial direction
B	number of rotor blades
C	chord length
$C_i$	cosine integral function
$\tilde{C}_L$	unsteady lift coefficient
$C_{mn}$	normalization constant of radial modal distribution
c	speed of sound
D	diffusion factor
d	wave front vector
$E_{mn}$	radial distribution function of (m,n) mode
F	force
f	frequency
$f^*$	cutoff frequency
h	annulus width
i	incidence angle
J	Bessel function of first kind
$J'$	derivative of J
$\bar{J}$	integration of J
K	coefficient of flow resistance
k	wave number
$k'$	normalized wave number

<u>Symbol</u>	<u>Description</u>
$L$	length
$\epsilon$	lattice coefficient
$\tilde{L}$	unsteady lift
$M$	Mach number
$m$	circumferential mode order
$N$	number of summations in Fourier series
$n$	radial mode order
$P$	static pressure
$p$	acoustic pressure
$Q$	rate of introduction of mass per unit time
$Q_{mn}$	characteristic constant of (m,n) mode
$R$	reflection coefficient
$r$	radius
$r_o$	root mean square of hub and tip radii
$S$	blade spacing
$S_i$	sine integral function
$T_{ij}$	fluid stress tensor
$t$	time
$U$	blade rotational velocity
$V$	flow velocity
$W$	relative velocity
$x$	axial coordinate
$y$	circumferential distance
$Y$	Bessel function of second kind
$\alpha$	helix angle

<u>Symbol</u>	<u>Description</u>
$\beta$	relative flow angle
$\gamma$	cutoff ratio
$\delta$	deviation angle
$\delta(x)$	delta function
$\theta$	circumferential coordinate
$\xi$	stagger angle
$\rho$	air density
$\sigma$	hub-tip radius ratio
$\tau$	acoustic resistance
$\phi$	flow coefficient
$\phi_{mn}$	phase angle of (m,n) mode
$\chi$	acoustic reactance
$\omega$	rotor rotational speed
$\overline{\omega}$	integration of Weber function
$\mu$	dimensionless constant in the calculation of reflection coefficient

#### Subscripts

$o$	plane wave mode
$1$	(1,0) mode
$a$	hub radius
$b$	tip radius
$d$	disturbance
$e$	rotor exit
$f$	fundamental
$i$	rotor inlet

<u>Subscripts</u>	<u>Description</u>
m	mean radius
mn	mode order
r	reflected wave
s	static
x	axial direction
$\mu\nu$	mode order and degree in orthogonality relation



## ACKNOWLEDGMENTS

This study was conducted under the sponsorship of Naval Sea Systems Command through the Applied Research Laboratory, The Pennsylvania State University (ARL/PSU) which made the facilities used available.

The author wishes to express his sincere appreciation to his advisor, Dr. Frank S. Archibald, for his guidance, assistance and encouragement throughout the investigation. The helpful suggestions of Professor Robert E. Henderson are also greatly appreciated.

The author also wishes to acknowledge the frequent advice of Dr. Edgar P. Bruce, Mr. George B. Gurney, and Mr. Allen L. Treaster on the operation of the experimental set up.

The frequent aid of Mr. Wilden L. Nuss and Mr. Salvatore E. Alvarez in the operation of the signal analyzer and the calibration of lift gage by Mr. James P. Cowan are also appreciated.

## CHAPTER I

### INTRODUCTION

#### 1.1 Introduction and Previous Investigation

The sound generated by turbomachines is not only of high amplitude relative to the ambient background noise levels, but generally its frequency content is in the range to which the ear is particularly sensitive. At the present time, the increasing size and wider application of such machines has led to increased interest in the reduction of turbomachine noise.

For example, the noise generated by a jet engine involves various acoustic components: externally, the exhaust gas mixing process, and internally, the unsteady flow through the fan stage, compressor, and turbine. A significant part of the engine noise is the discrete frequencies generated by the interaction of the rotating and stationary fan blade rows at the fundamental and harmonics of the fan blade passing frequency (BPF). Currently the BPF generated by the fan in high-bypass ratio engines dominates the acoustic signature of the jet engine. However, as the noise generated by the fan is reduced with acoustic treatment in the fan duct, the tone noise produced by the power turbine becomes increasingly important. Because the mechanism of BPF generation is the same for both engine components the study of the noise generating mechanisms of the fan will lead to a quieter engine. This is one reason why the study of fan noise is of interest.

The emission of fan noise can be divided into three phases:

1. Generation

Fan noise can be characterized in terms of two components: broadband noise of relatively low amplitude and higher amplitude discrete blade passing frequency (BPF) tones. Broadband noise results mainly from (i) the random fluctuation in pressures on the rotor and stator components, and (ii) the turbulent inlet flow to the fan. The mechanism that generates the discrete BPF tones is the periodic interaction of downstream fan components with velocity deficiencies viscously generated by upstream fan components. The rotor and stator components are arranged in the form of a row of airfoils known as a cascade. Each blade in the cascade is, in general, subject to disturbances from the upstream blades as well as the blades in the same row. The unsteady lift force generated on each blade is equivalent to an acoustic dipole when the acoustic wavelength of the unsteady lift is much greater than the blade chord. When this condition prevails, the unsteady lift corresponds to a "compact" source. A compact acoustic dipole is analogous to a pair of pulsating spheres (point sources) separated by a small distance in comparison to the acoustic wavelength. The pulsation of the spheres is in anti-phase and the combination generates a force on the fluid along a line connecting the center of the spheres. This fluctuating force corresponds to the unsteady lift vector.

## 2. Transmission

The transmission of an acoustic wave in a duct can be described in terms of acoustic modes  $(m,n)$ . A specific mode is one of an infinite series of solutions of the wave equation for the specified duct geometry and boundary conditions. If the acoustic pressures at each blade in a cascade are in phase with each other, the acoustic energy will be transmitted along the duct in the plane wave  $(0,0)$  mode. This mode has a uniform distribution of acoustic pressure over the duct radius and all frequencies propagate axially along the duct at the free-field sound speed. It is also possible to transmit acoustic energy along a duct in higher order modes. These higher order modes have a nonuniform spatial distribution of acoustic pressure and above the respective cutoff frequency have a phase speed greater than the free-field sound speed. Higher order modes consist of non-spinning modes  $(0,n)$  and spinning modes  $(m,n)$ , where  $m$  is the number of pressure modes in the radial direction. The wave front of non-spinning modes has a purely axial propagation direction, but the wave front of spinning modes  $(m,n)$  travels in a helix along the duct. The solution of the wave equation indicates that these higher modes will decay exponentially along the duct in the axial direction unless the exciting frequency is greater than the specific modal cutoff frequency. Figure 1 shows the characteristics of the transmission of the plane and spinning acoustic duct modes.

In addition to the plane wave mode this thesis is specifically concerned with the first higher order acoustic

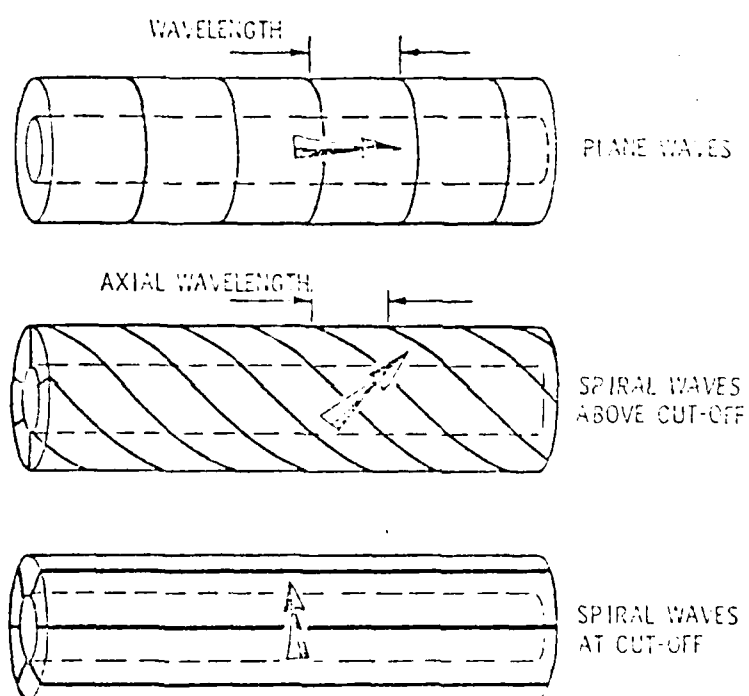


Figure 1 Transmission of the Acoustic Duct Modes

mode  $(-1,0)$ . The minus indicates that the mode is spinning in a circumferential direction opposite to the rotational direction of the rotor. The one indicates there is one sinusoidal cycle of pressure variation circumferentially around the duct. The zero indicates that there are no reversals of the mode pressure along a radius. A further property of all higher order modes is a maximum pressure on the outer wall.

### 3. Radiation

For the propagating modes, there is a strong pressure field at the open end of the duct and this acoustic pressure radiates into free space in a directivity pattern dependent upon the particular mode. For the plane wave mode, the far-field acoustic pressure is a maximum on the duct axis. In contrast, for the propagating  $(1,0)$  mode at cutoff frequency ratios greater than one, cancellation occurs on the duct centerline. For an acoustic dipole, the pressure from the positive and negative sources cancel on the plane normal to the dipole axis. The directivity pattern on the  $(1,0)$  mode at frequencies slightly above cutoff resembles (in a plane passing through the duct centerline) that of an acoustic dipole (lying in this plane) with its axis oriented across the duct opening.

#### 1.2 Previous Theoretical Work

The theoretical analysis of the noise from turbomachines is concerned with the prediction of the unsteady aerodynamic lift and the acoustic far-field pressure as a function of various design parameters.

### 1.2.1 Unsteady Lift

The interaction of a cascade of airfoils with a spatially varying inlet flow is shown in Figure 2. The velocity deficiencies of the upstream flow cause the magnitude as well as the direction of the velocity relative to the airfoils to change with time, thus generating an unsteady lift on the airfoils. The response of an unsteady flow was first solved by Kemp and Sears [1]\*, who considered an isolated, thin, flat-plate airfoil at zero incidence in two-dimensional incompressible flow subject to small velocity perturbations that were normal to the airfoil chord. Later, Horlock [2] analyzed the effect of the disturbances both normal and parallel to the airfoil chord on an isolated flat-plate airfoil. In a cascade of airfoils, the interference between the blades in a row becomes especially significant for high solidity cases. Whitehead [3, 4] analyzed this effect for a single infinite two-dimensional cascade in inviscid incompressible flow. An analysis by Henderson and Daneshyar [5] includes the effects of blade camber and angle of incidence in the cascade response.

Other work has been performed which includes the compressibility of the fluid so that the generated sound waves can be calculated. As an example, Smith [6] considered a cascade of flat plates at zero mean incidence to be replaced by a series of continuous singularity distributions and obtained a closed-form solution for the unsteady lift and acoustic pressure due to several perturbation types. Another example is the work of Kaji and Okazaki [7], who used pressure doublets to represent a flat-plate cascade and treated it by unified linearized

\*Numbers in brackets designate References

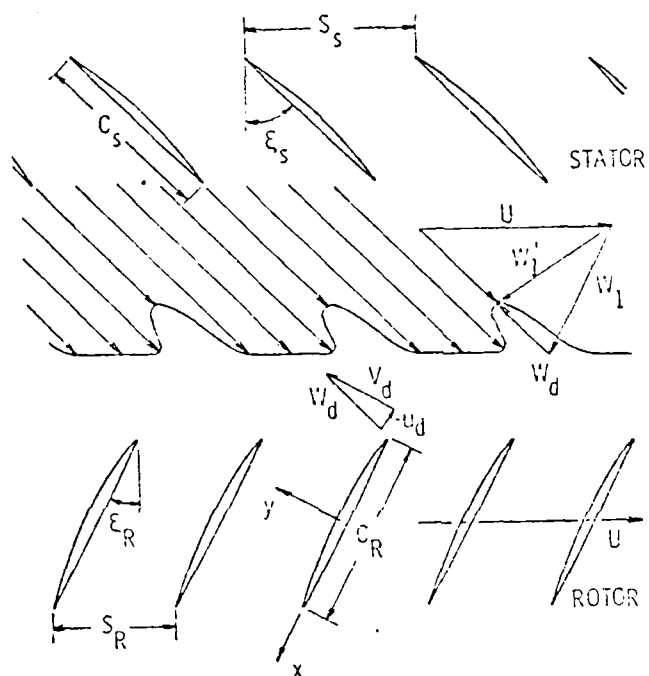


Figure 2 General Disturbance Flow in a Cascade



equations. Mani [8] assumed the blade chord and spacing to be small compared with the wavelength and thus simplified the cascade response problem to that of an actuator disk model. Osborne [9] used the linearized potential flow equation to predict the unsteady lift and moment.

#### 1.2.2 Acoustic Generation

Tyler and Sofrin [10] studied the acoustic excitation and transmission of sound from a known pressure source in an annular duct. They demonstrated that aerodynamic interaction between blade rows could result in a rotating pressure pattern. This rotating pattern could excite propagating spinning modes which require a supersonic tangential phase speed, even though the rotor tip velocity is subsonic.

#### 1.2.3 Acoustic Transmission

The description of the transmission of sound in an infinite duct in terms of Bessel and Neumann functions has been known for some time. More recent work has been performed by Morfey [11], who investigated the reflection and radiation of sound from the end of a duct. The transmission of sound from the end of the duct is the radiation problem and depends on the boundary conditions at the duct exit. For example, Tyler and Sofrin [10] used a baffled duct model to predict the acoustic measurements of a fan for angles not near 90 degrees.

### 1.3 Previous Experimental Work

Experimental work has concentrated on measuring the unsteady lift response of a blade in a cascade to measured inflow distortions without measurement of the acoustic output. In those instances where acoustic

pressures have been measured, only the inflow distortion has been measured; the unsteady lift has not been simultaneously measured. The unsteady lift response of a blade in a cascade has been measured by Bruce [12]. Recently, measurement of the fluctuating pressure on blades has become possible with the development of miniature transducers. Satyanarayana, Henderson, and Gostelow [13] used 'Pitran' pressure transducers inserted in an uncambered stator of 6-inch chord in a single-stage fan. They measured the pressure on both sides of the blade at 15 points along the chord. These measurements were found to be in agreement with the analysis of Reference [4]. Gallus et al. [14] used 'Kulite' transducers to measure the fluctuating pressures on both rotor and stator blades along the chord at the midspan.

Acoustic measurements of the acoustic tonal energy generated by a fan have been performed by several investigators. Early work in this area is that of Sharland [15] who found that the discrete frequency noise from multi-stage fans arose from the aerodynamic interaction of the fixed and rotating blade rows. He also reported that the amplitude of this tone noise was strongly dependent upon the axial spacing between the blade rows.

Other early work is that of Bragg and Bridge [16] who report the results of a panel of experts. They concluded that the tone noise from turbojet compressors was dipole in origin and predominately from the first few stages of the compressor. More recent work on compressor noise is that performed by Lomson [17] and Benzakein [18].

Lipstein and Mani [19] used an array of rods to produce an upstream wake interference in a single-stage axial flow compressor. They measured the far-field acoustic energy which was radiated at the first

two BPF harmonics, and obtained a reasonable agreement with the theory of Reference [8]. Harel and Perulli [20] employed a six-bladed fan at low axial flow speed and measured the frequency spectra, axial, circumferential, and radial wave number of the sound field in order to compare the structure of the acoustic modes in the duct with theory. Smith [6] measured the inflow distortion generated by screens and resulting acoustic pressures in a high hub-to-tip radius ratio rotor. After accounting for reflection at the duct exit, he obtained excellent agreement with his theory. Moore [21] used a microphone cross-correlated with a reference signal to measure the rotating sound field. Yardley [22] proposed a wave number spectrum measurement technique to analyze the acoustic field in a duct.

The possibility that an acoustic field can strongly influence an essentially incompressible hydrodynamic field was suggested by Doak [23]. He called this effect an acoustic back-reaction. Archibald [24, 25] in two companion papers found that indeed a high amplitude acoustic field was able to control the two instability phenomena of vortex shedding and Tollmien-Schlichting waves. Crow and Champagne [26] found that an acoustic field was able to produce a coherent structure in the flow from a low Mach number jet.

In addition to these references which deal directly with the problem under investigation, Morphey [27] and Cumpstey [28] have written critical reviews of engine-related aero-acoustic noise sources.

#### 1.4 Present Work

In surveying the existing knowledge of this field, it appears that there are several prediction formulae for unsteady lift as well as

acoustic modal pressures, and the experimental work is in good agreement with the theory. But, simultaneous detailed measurements of the aerodynamic pressure on the blades and the acoustic modal pressure in a duct are necessary to confirm the theoretical prediction and to find the coupling coefficient of the unsteady lift to acoustic modal pressure. In order to remove the possibility of ambiguity in this matter, the present work has been undertaken to generate and measure the acoustic pressure of duct modes due to the interaction mechanism, and simultaneously to measure the unsteady lift on a rotor blade. This will establish the coupling factor which has not received attention previously, and will permit investigation of any back-reaction effects of the acoustic pressures on the unsteady aerodynamic response.

## CHAPTER II

### EXPERIMENTAL ASPECTS

#### 2.1 Introduction

The experiment was designed to investigate the generation of fan blade passing frequency (BPF) tone noise in a duct. Figure 3 shows the theoretical mechanisms and the measurements that were performed at various positions in the noise generation process. These measurements were used to confirm the theory at many points in the generation process. The velocity field was produced by distortion screens and measured using a five-hole probe. The circumferential velocity profile was then Fourier analyzed. The rotor blades interacting with the distorted velocity profile generate an unsteady lift which excites acoustic modes in the duct and eventually radiate as BPF sound. The unsteady force normal to the chord (lift) was measured using a strain gage sensor installed inside a one-inch spanwise segment at midspan of a rotor blade shown in Figure 4. The acoustic pressure was measured with a flush-mounted 1/8-inch Bruel and Kjaer (B&K) microphone at four locations along the duct to decompose the pressure into duct modes and to find the coupling coefficient between the aerodynamic pressure and the acoustic modal pressure.

#### 2.2 Apparatus

The experiment was performed in the Axial Flow Research Fan (AFRF), a facility of the Garfield Thomas Water Tunnel which is located at The Pennsylvania State University. This facility is shown in Figure 5.

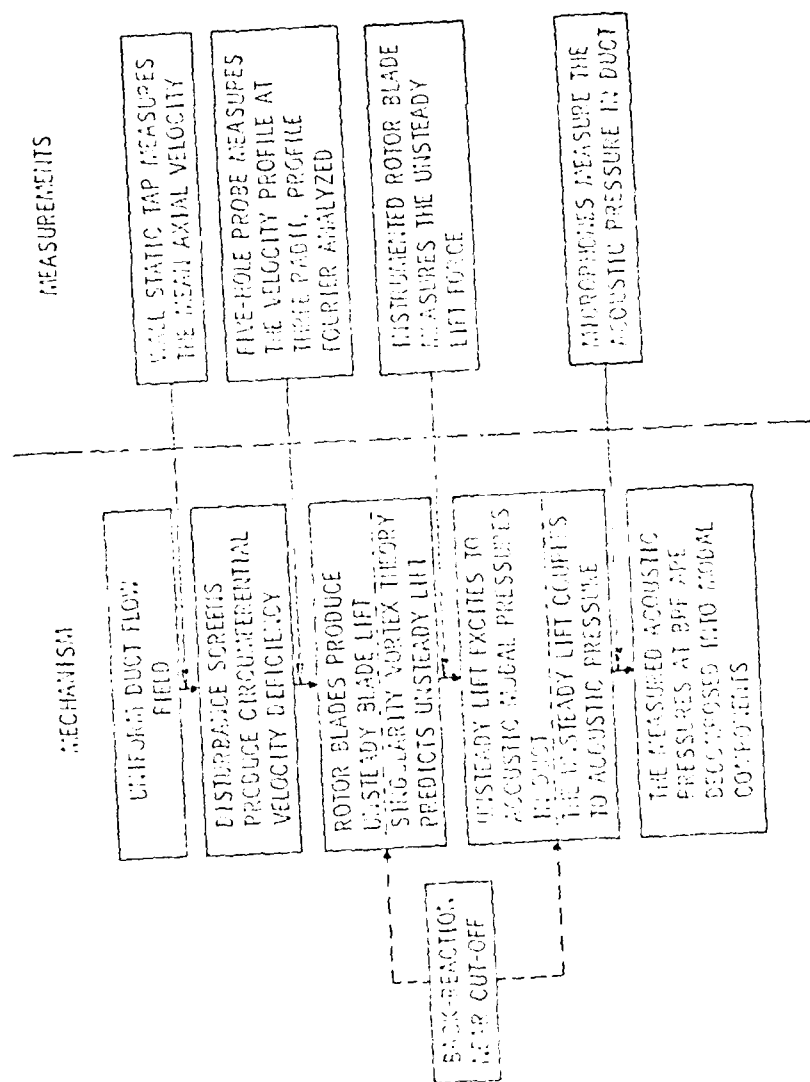


Figure 3 Schematic Diagram of Fan Noise Mechanism and Experimental Measurement

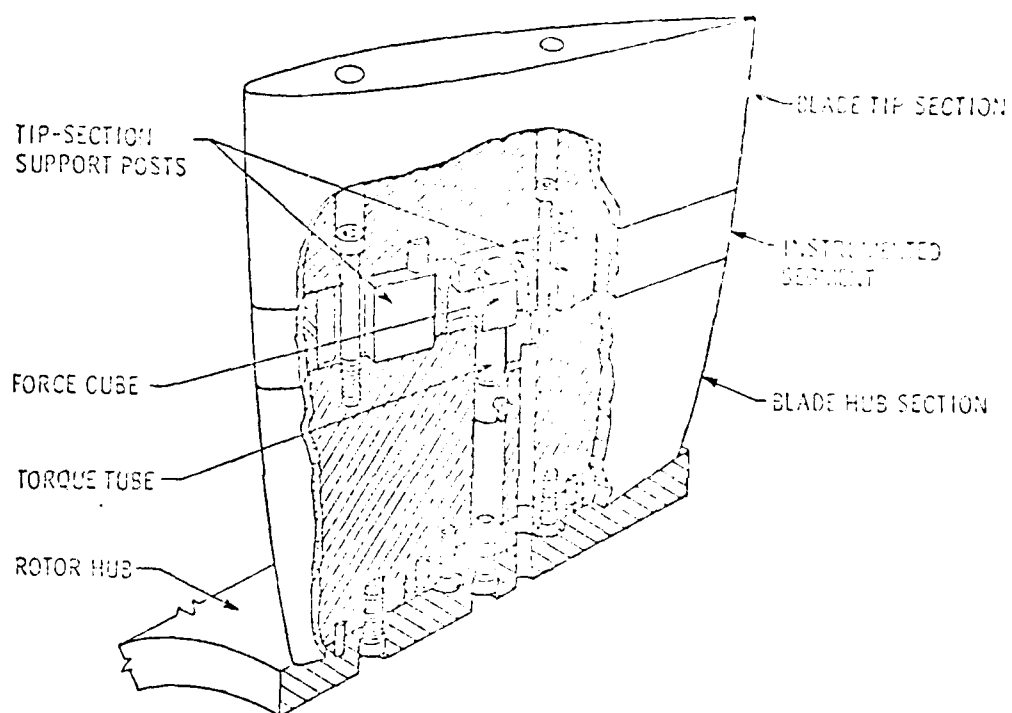


Figure 4 Instrumented Rotor Blade

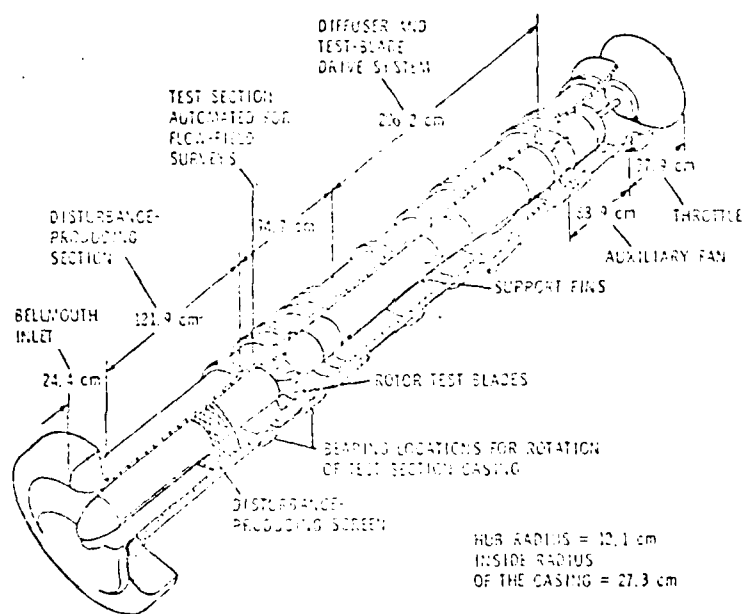


Figure 3 Axial Flow Research Fan



This apparatus has been described by Bruce [29]. The AFRF is 19.6 feet long and consists of a bellmouth inlet leading to an annular flow passage, which contains a test rotor and an auxiliary fan. At the end of the AFRF, there is an exhaust throttle. The facility has a hub radius of 4.75 inches and a tip radius of 10.75 inches. The hub-tip radius ratio is 0.442.

The auxiliary fan is driven by a 70 HP motor and is capable of delivering 1,500 cubic feet of air per minute at a pressure of 3.5 inches of water gage. The research rotor is driven by a separate 20 HP motor; thus, in conjunction with the auxiliary fan, the research rotor can be operated over a range of steady lift coefficients. The research rotor consists of nine cambered blades with a chord length of six inches and a span of six inches. The blade profile was a circular-arc camber-line with 10 percent maximum thickness-to-chord ratio. A list of rotor parameters is given in Table 1 and the details of the rotor design are described in Appendix A.

The four microphone measurement positions were selected to optimize the discrimination between the  $(-1,0)$  and  $(0,0)$  modes after considering acoustic reflection effects from the duct open end and the rotor. The details of the selection of the microphone locations is described in Appendix B. Figure 6 shows the locations of the distortion screen, test rotor, microphones, and static pressure tap at the inlet for determining the mean axial velocity  $\bar{V}_x$ . The design procedure of the distortion screens is presented in Appendix C.

TABLE I  
GEOMETRIC PARAMETERS OF NINE-BLADED CAMBERED ROTOR

Radius (inch)	Chord (inch)	Space- chord Ratio	Maximum Camber (inch)	Camber Angle (deg)	Stagger Angle (deg)	Inlet Blade Angle (deg)	Outlet Blade Angle (deg)
4.75	6.0	0.5526	0.1764	35.64	23.14	40.96	5.27
5.35	6.0	0.6225	0.0876	28.12	31.02	45.58	16.90
6.55	6.0	0.7621	0.0228	17.87	42.44	51.38	33.55
7.75	6.0	0.9018	0.0066	11.74	50.28	56.14	44.39
8.45	6.0	1.0414	0.0020	8.01	55.78	59.63	51.77
10.15	6.0	1.1810	0.0007	5.71	59.85	62.71	57.04
10.75	6.0	1.2508	0.0004	4.80	61.59	63.99	59.19

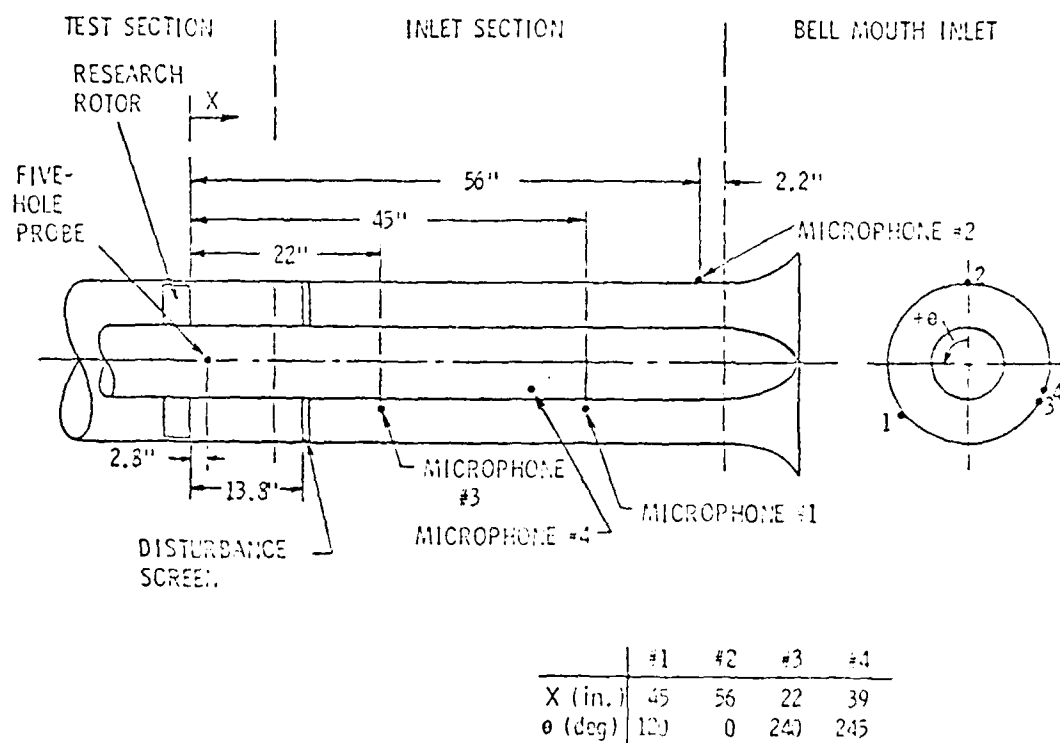


Figure 6 Location of Disturbance Screen, Rotor, and Microphone

### 2.3 Instrumentation

A five-hole probe located in the plane of the rotor leading edge was employed to measure the local velocity with the rotor removed. The pressures from each hole in the probe were converted into DC voltages by using five separate pressure transducers. The voltages were processed by a multi-channel integrating digital voltmeter with the output punched onto a paper tape. The paper tape was then fed into a computer for data reduction. The measured velocity profiles were Fourier analyzed. The magnitude and phase of 30 harmonics were determined. A block diagram of the instrumentation is shown in Figure 7.

A Harrison amplifier was used to amplify the voltage of the AC signal from the instrumented rotor blade by 1,000 times to supply a constant four volts DC to the strain gage through the slip rings inside the hub. A photodiode sensed the light passing through a single slit in a disk on the rotor shaft generating a once-per-revolution pulse as a circumferential position reference. Another photodiode sensed the light passing through an inner row of 60 slots on the same disk. This gave a direct reading of the shaft speed in rpm in a one-second counting period. The unsteady pressure was measured by one 1/8-inch B&K microphone connected to a B&K 2603 amplifier which also supplied the DC voltage to the microphone. This microphone was then moved systematically to the other locations in the duct which were closed with flush fitting inserts.

The signals from the lift gage and microphone were analyzed using a number of the analysis options of the Spectral Dynamics Corporation Model 360 two-channel digital signal processor. The SD-360 has a built-in Fast Fourier Transform (FFT) which can produce an ensemble

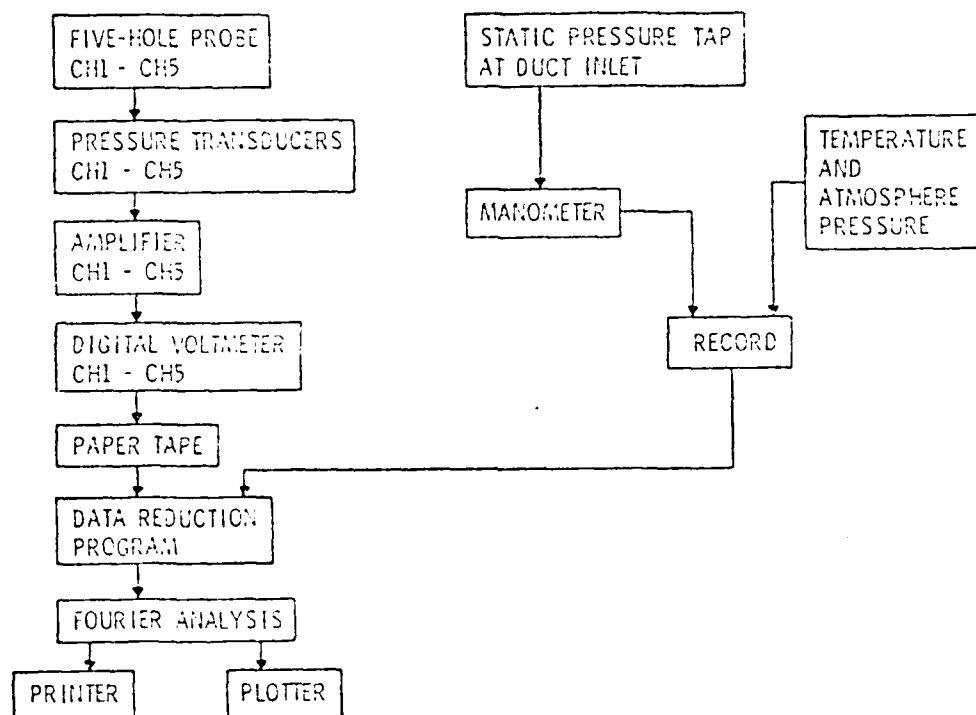


Figure 7 Instrumentation Block Diagram for Velocity Measurement

averaged spectrum (function 4). In conjunction with a Spectral Dynamics SD-134A signal ratio tuner, it can perform phase-locked averaging in the time domain (function 12) and phase-locked averaging/FFT analysis (function 13). The time position reference is the once-per-revolution pulse. Figure 8 shows a schematic diagram of this instrumentation. The tracking ratio tuner, using the once-per-revolution pulse, generates exactly 1024 pulses per revolution of the rotor. These pulses trigger the SD-360 to sample the input signal and completely fill the memory of the analyzer in one shaft revolution. The samples of the signal of each subsequent shaft revolution are added to the average of the previous data in the memory to obtain an ensemble average in the time domain.

The raw signals from the strain gage and microphone were also connected to a two channel oscilloscope for a visual check of the quality of the signals. A pressure transducer and its associated signal conditioning equipment were used to measure the wall static pressure of the duct for calculating the mean axial velocity for each test.

The setting of the frequency range and aliasing filter on the signal processor, and the frequency ratio on the tracking ratio tuner are important for the time domain averaging (functions 12 and 13). A description of the effect of variation in these settings is contained in Appendix D.

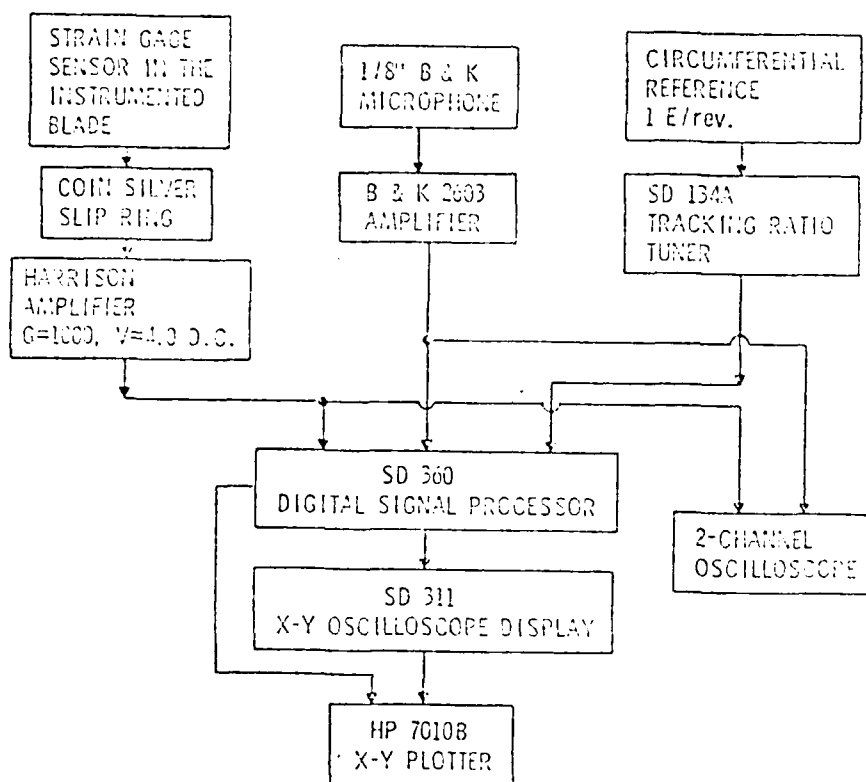


Figure 3 Instrumentation Block Diagram for Unsteady Pressure Measurement

## 2.4 Calibration

### 2.4.1 Five-hole Probe Calibration

The calibration of the probe involved experimentally determining a set of data in a known flow field that was processed by a computer and resulted in a description of the response of the probe. The probe was mounted in a calibration device which permitted a  $\pm 30$ -degree rotation in both the yaw and pitch planes. The pressure coefficient as a function of flow velocity and angle was measured in the potential core of an open-jet facility at each calibration point. A detailed description of the calibration procedure was presented by Treaster and Yocum [30]. The calibration curve for the probe used in this investigation is shown in Figure 9.

### 2.4.2 Strain Gage Calibration

A static calibration of the strain gage was performed by varying the masses loaded on the instrumented blade; this resulted in a sensitivity to a normal force of 0.972 lb/volt. The dynamic response of the gage, shown in Figure 10, was obtained from the broad band envelope of the spectrum of the gage signal when no distortion screen was installed. The resonance of the blade section was found to be on the order of 500 Hz which is well above the cutoff frequency of frequency of the (1,0) mode, i.e., 280 Hz, and also well above the maximum BPF that was investigated in the experiment. See Appendix G for further discussion of the validity of the static calibration.

### 2.4.3 Microphone Calibration

A known acoustic source level of 124 dB (ref 0.0002 pbar) from a 1.5" piston phone calibration Model 4220 was employed to calibrate the



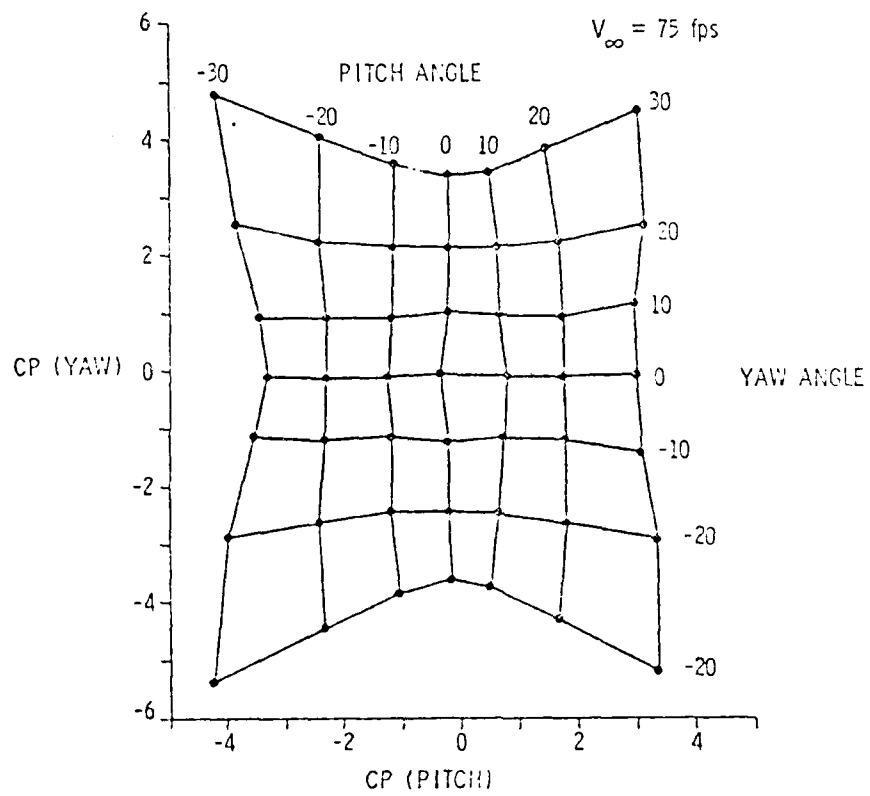


Figure 9 Calibration Plot of the Five-hole Probe

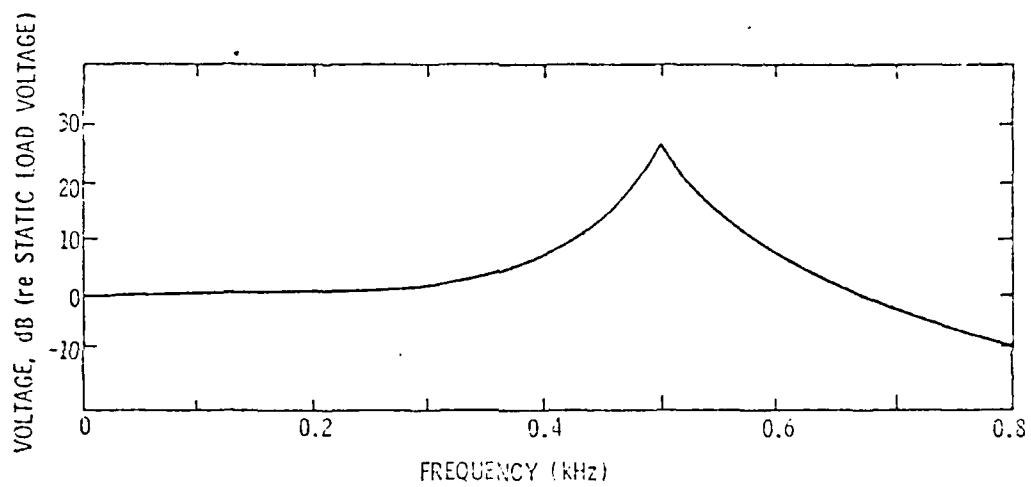


Figure 10 Dynamic Response of the Lift Gage

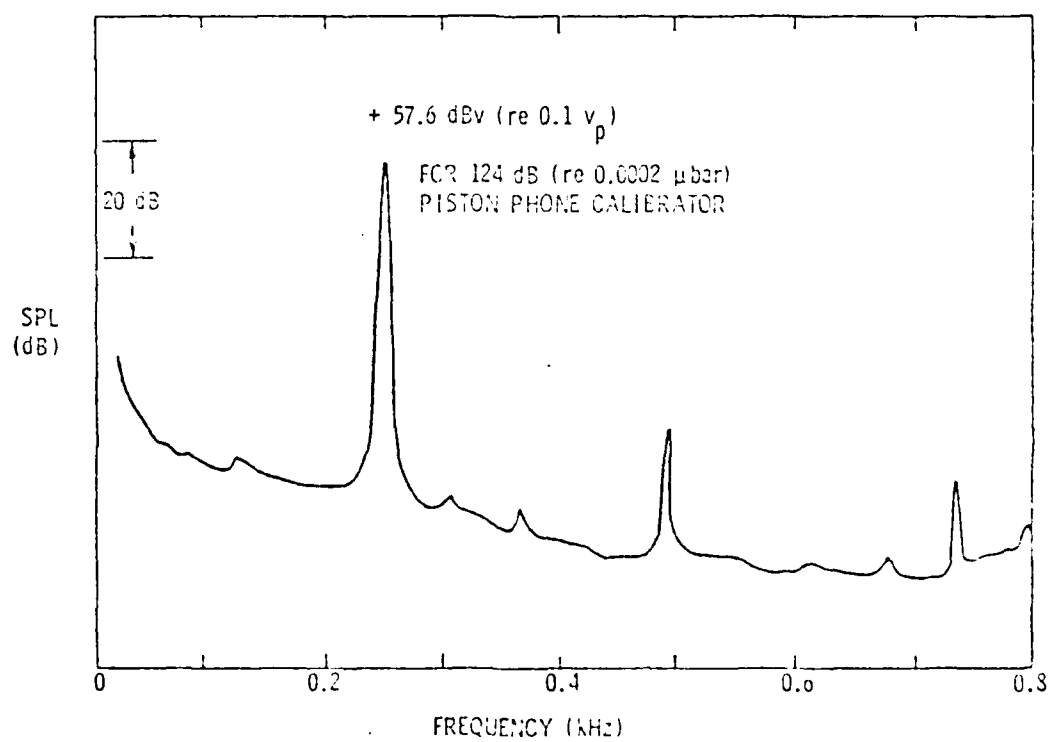


Figure 11 Spectrum of Microphone Calibration

microphone. The spectrum with the piston phone applied is shown in Figure 11 and resulted in a 57.64 dB voltage level (reference to 0.1 volts peak) with the B&K amplifier and SD-360 analyzer attenuators at zero for this end-to-end calibration.

#### 2.4.4 Signal Processor Calibration

The SD-360 provides an internal calibration tone of 0 dB or 676 linear scale units, relative to 0.0707 volts rms at approximately 25 percent of the full frequency range. The 0 dB reference was set using this calibration tone every time the power switch was turned on or a different signal analysis option was selected. A check of the internal calibration was also conducted using a signal generator and voltmeter and it was found that 0.071 volts rms input sinusoidal signal corresponded to 0 dB, or 680 linear scale units. This is the same as the internal calibration within the experimental accuracy.

The calibration of the strain gage and the signal processor was also checked by using the effect of gravity on the instrumented blade segment. The gravitational force produces a one-cycle sinusoidal signal on the lift gage in one revolution of the rotor blade. Therefore, tonal energy at the fundamental (i.e., shaft rate) in the first spectrum of the lift gage signal should be the result of the gravitational force and be independent of rotor speed. The magnitude of this harmonic was found to be 0.053 and 0.060 volts peak for all rotor speeds when the nine- and ten-cycle screens were installed, respectively. The weight of the blade segment was 0.056 pounds. Using this information, a calibration constant of 0.966 or 0.933 lb/volt was obtained for the two separate cases. This is a good confirmation of the static calibration value of

0.972 lb/volt. Confirmation of the validity of the gravitational check is the fact that the phase angle of the first harmonic maintained a constant value of -73 degrees for all rotor speeds. The gravitational force acts downward at the -90 degrees position from the 12 o'clock location of the duct and produces a positive value of lift. Since the once-per-revolution pulse was at -16.2 degrees, the maximum lift should occur at  $(-90 + 16.2) - 73.8$  degrees. Consequently, the effect of gravity is apparently producing the first harmonic on the lift spectrum within the measurement accuracy.

## 2.5 Measurement

The disturbance screens were located at 16.5 inches upstream of the leading edge of the rotor. The distance between screen and rotor is determined by considering the effect of turbulent mixing downstream of the screens. Turbulent mixing tends to reduce large velocity gradients caused by step changes in the flow resistance coefficient,  $K$ , of the screens. Far downstream of the screen the velocity profile becomes smoother, however, the fundamental harmonic,  $A_f$ , also has decayed, which is not desired. The optimal distance is larger for screens with low numbers of circumferential distortion cycles than screens with high numbers of distortion cycles because the velocity gradient is smaller for the low number distortion cycle case and there is consequently less turbulent mixing.

Measurements were conducted to find the characteristics of the flow fields produced by screens as a function of circumferential angle,  $\theta$ , at three radial positions: midspan ( $r = 7.75$  inches), one inch from the rotor tip ( $r = 9.75$  inches), and one inch from the rotor hub

( $r = 5.75$  inches). The circumferential surveys were performed in 2-degree increments by keeping the screen spatially fixed and rotating a downstream portion of the outer casing. The casing portion containing the velocity probe was located in the region of the test rotor. The rotor was removed during the velocity surveys to avoid contaminating the measurement.

The mean axial velocity,  $\bar{V}_x$ , was selected to give the desired incidence angle over the operating speed range of the rotor of the AFRF. The velocity  $\bar{V}_x$  can only be calculated when the velocity profile is known and it is not practical to use the five-hole probe to set  $\bar{V}_x$ . Thus, the static pressure  $\Delta P_s$  measured with a wall static tap just downstream of the duct inlet when the screens were calibrated was used to obtain the desired velocity in the following manner. Temperature and atmospheric pressure were recorded to calculate the air density,  $\rho$ . Using Bernoulli's equation, the  $\bar{V}_x$  can be related to the pressure difference  $\Delta P_s$  and  $\rho$ . The quantity  $\Delta P_s/\rho$  plotted versus  $\bar{V}_x$  is a straight line on log-log paper, which is different for each screen, as shown in Figure 12. When  $\bar{V}_x = 0$ ,  $\Delta P_s/\rho$  represents half the pressure loss due to the distortion screen. By interpolation of these plots, the desired value of  $\Delta P_s$  at each  $\bar{V}_x$  can be obtained for all test conditions. The pressure measured from the tap was then used for setting the operating condition during the unsteady pressure measurements portion of the test.

The zero circumferential position was selected as the 12 o'clock position of the duct. The once-per-revolution pulse was measured to occur at -16.2 degrees relative to this zero position, i.e., 16.2 degrees of rotor rotation prior to the top. Figure 13 shows the spatial position

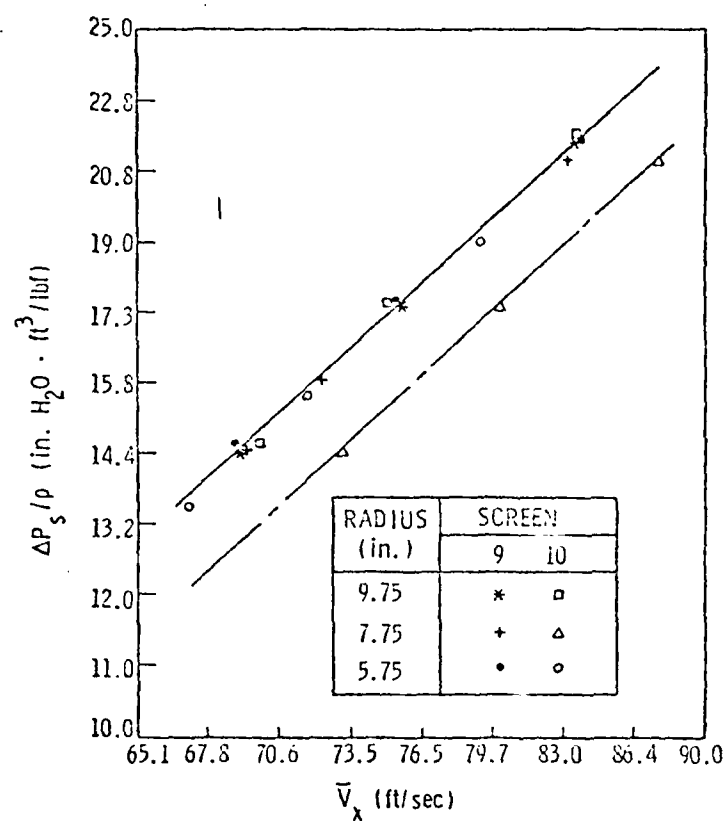


Figure 12 Correlation of  $\Delta P_s / \rho$  and  $\bar{V}_x$  for Distortion Screens

TABLE II  
TEST MATRIX OF UNSTEADY PRESSURE MEASUREMENTS

Test Variable		Measurement	Unsteady Lift			Acoustic Pressure	
Disturbance Screen	Flow Coefficient	Rotor Speed (rpm)	Function			Function	
			4	12	13	4	13
No.	0.56	742	x		x	x	x
		1110	x		x	x	x
		1480	x		x	x	x
	and	1668	x		x	x	x
		1760	x		x	x	x
		1853	x		x	x	x
	0.70	1946	x		x	x	x
		2083	x		x	x	x
		2100	x		x	x	x
9-Cycle	0.56	742	x	x	x	x	x
		1110	x	x	x	x	x
		1480	x	x	x	x	x
		1574	x	x	x		
	and	1621	x	x	x		
		1668	x	x	x	x	x
		1714	x	x	x		
		1760	x	x	x	x	x
	0.70	1854	x	x	x	x	x
		1946	x	x	x	x	x
		2038	x	x	x	x	x
10-Cycle	0.56	742	x	x	x	x	x
		1110	x	x	x	x	x
		1290	x	x	x		
		1432	x	x	x		
	and	1480	x	x	x	x	x
		1668	x	x	x	x	x
		1760	x	x	x	x	x
		1854	x	x	x	x	x
	0.70	1900	x	x	x		
		1946	x	x	x	x	x
		2038	x	x	x	x	x
		2100	x	x	x	x	x





used in the phase measurement of unsteady lift. The phase angle of unsteady lift was defined relative to the leading edge of the blade. When the blade coincides with the minimum axial velocity, a positive upwash and incidence angle is defined. The unsteady lift signal from the lift gage was electrically positive for a positive deflection, which is in the same direction as the positive upwash. The minimum axial velocity of the screen was positioned at the 12 o'clock position. Note that one cycle of the nine-cycle screen only occupies 1/9th of the 360 degrees in the duct, i.e., 40 degrees. Thus, the 16.2 rotor degrees corresponds to  $(16.2/40 \times 360)$  145.8 degrees in the screen or unsteady lift cycle. Similar considerations hold for the ten-cycle screen.

The test matrix of unsteady pressure measurements is shown in Table II. The variables of the test are enumerated below.

1. Number of cycles of the disturbance screen: Nine- and ten-cycle screens were used to generate the plane wave (0,0) mode and the first higher order (-1,0) mode for the nine-bladed rotor. Measurements with no distortion screen were also conducted to find the background noise level.
2. Research rotor speed: Twelve rotor speeds were selected to have the blade passing frequencies (BPF) below, at, and above the (1,0) mode cutoff frequency of the duct.
3. Flow coefficient  $\phi$ : The mean axial velocity,  $\bar{V}_x$ , was set by the auxiliary fan so that the flow coefficient  $\phi = \bar{V}_x / r\omega$  could be selected independently of the research rotor. The mean incidence angle,  $i_m$ , at midspan was determined from velocity triangles. Two flow coefficients  $\phi = 0.70$  ( $i_m = 0.3^\circ$ )

and  $\phi = 0.56$  ( $i_m = 6.0^\circ$ ) were chosen to investigate the effect of steady load on the unsteady lift and acoustic pressure measurements.

## 2.6 Experimental Accuracy and Repeatability

### 2.6.1 Velocity Survey

In the velocity measurements downstream of the distortion screen, the 2-degree circumferential increment of the outer casing was obtained by a Slo-Syn motor. This motor was controlled by an indexer capable of a minimum of 1/80-degree adjustment. Thus, very little error would result from the measurement locations. Measurements were repeated four times at each location; a statistical computer subroutine was then employed to analyze the data. It indicated that the normalized 90 percent error of the mean for the voltage reading corresponding to the velocity in the axial direction was less than 10 percent. This was a typical result for the highly turbulent flow field behind the screens. The amplitude of harmonic numbers N between 20 and 30 were found to be always less than five percent of the fundamental one.

### 2.6.2 Unsteady Lift and Pressure Measurements

The raw signals from the strain gage and the microphone were ensemble averaged 256 times for both the spectrum and the phase-locked option. The phase-locked average (functions 12 and 13) preserves the signal that is periodic with the rotor speed, while random or non-periodic signals will tend to diminish due to the large number of sums in the average. Thus, the magnitude and the phase obtained were due to the periodic interaction between the spatially fixed velocity distortion and the

rotor. Furthermore, the values of the magnitude obtained with the spectrum and phase-locked average were in close agreement, indicating that there was no significant effect of inflow turbulence causing high levels of intermittent spatial distortion.

Each unsteady measurement was repeated at least four times on a different date. It was found that the acoustic pressure repeated very well; the spread in magnitude and phase were less than  $\pm 0.2$  dB and  $\pm 2$  degrees. The differences of magnitude and phase on the unsteady lift were within  $\pm 0.5$  dB and  $\pm 5$  degrees for most cases. However, larger fluctuations of lift were observed for speeds near the cutoff frequency about  $\pm 1.0$  dB and  $\pm 20$  degrees for the worst case. The normalized standard deviation of the unsteady measurement was generally less than 4.5 percent. It increased to 23.4 percent for the largest fluctuation of lift near cutoff.

## 2.7 Data Validity

Figure 14 is a spectral comparison of the acoustic pressure with the rotor operating above cutoff when the nine- and ten-cycle screens were installed. The background noise was measured at the same shaft speed, but with no distortion screen installed. Because the background noise was lower by 30 dB than the signal at BPF, the experimental measurements are considered valid.

Figure 15 is a spectral comparison of the unsteady lift gage with the rotor operating above cutoff when the ten-cycle screen was installed. (The nine-cycle screen gave similar results.) The background noise was measured at the same shaft speed, but with no distortion screen installed. Another form of background noise is the electrical noise due to the slip

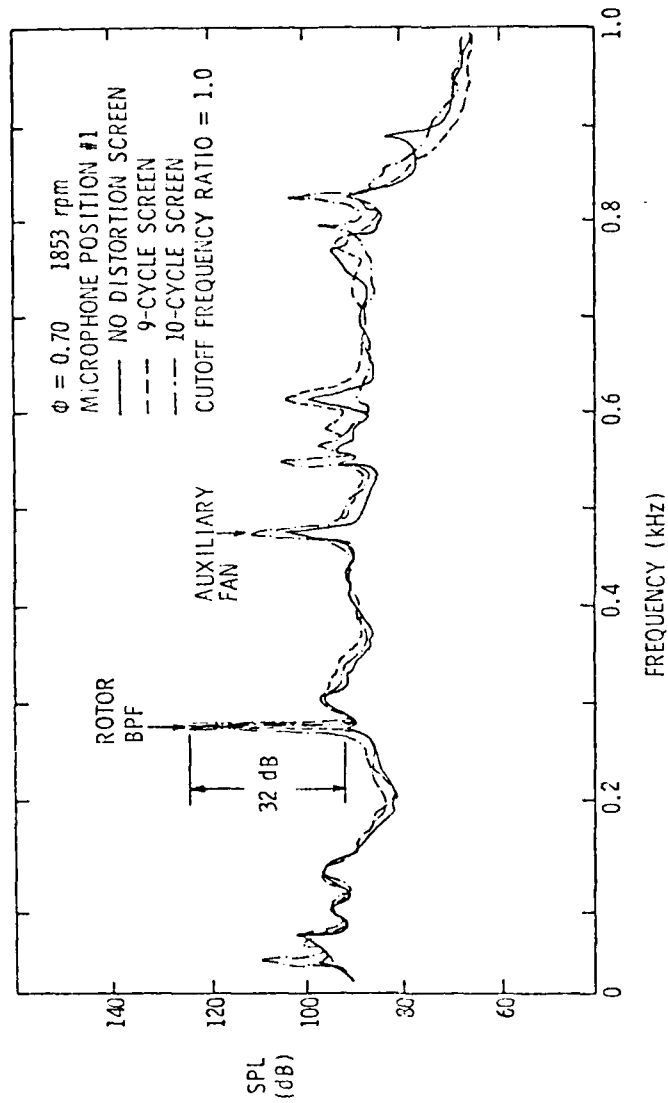


Figure 14 Background Noise of Microphone Measurement

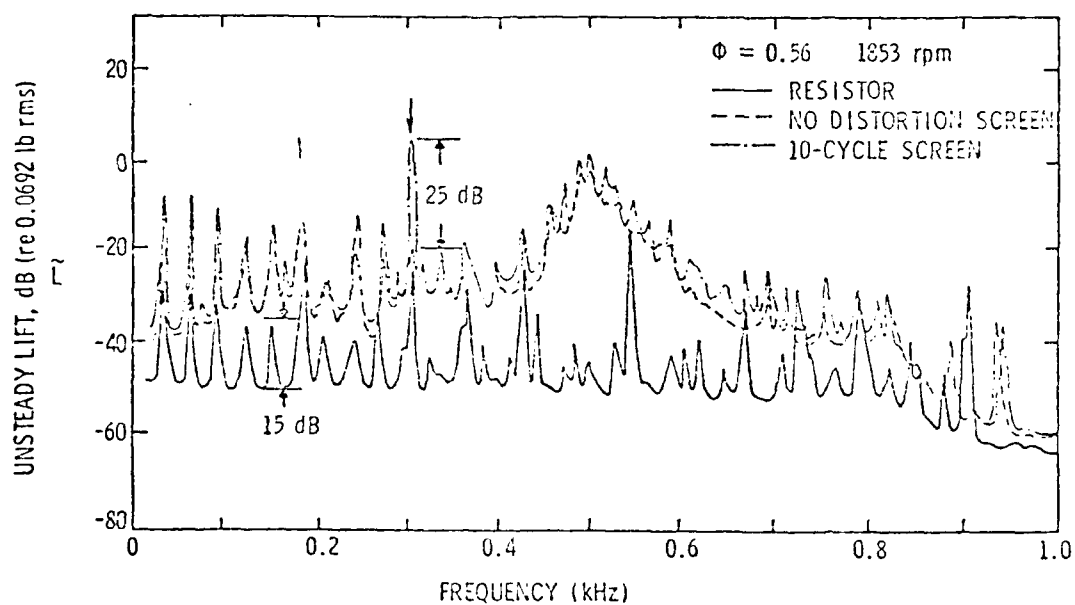


Figure 15 Background Noise of Unsteady Lift Gage Measurement

rings. This was determined by replacing the strain gage with an equivalent resistor bridge. The output of this configuration at the same operating conditions is also shown in Figure 15. Although the tones at integer multiples of the shaft rotation frequency were generally the same with or without the screen present, a 25-dB difference in level was observed at the tenth harmonic of the shaft frequency. Thus, the signal-to-noise ratio is sufficient to make the data valid.

## CHAPTER III

### RESULTS AND COMPARISON WITH THEORY

#### 3.1 The Sound Field in a Duct

The modal structure of the sound field in an infinite-length annular duct with no mean axial flow has been well studied and understood [31, 32]. The resulting sound pressures can be represented in the form of an array of transformed modal distribution functions. The circumferential part is simply a Fourier transformation and consists of corotating and counterrotating modes. The radial transform is more complicated; the resulting characteristic functions depend on circumferential mode number, hub-tip radius ratio, and the radial mode number. The transformed wave number in the axial direction determines the propagation characteristics; the transition from acoustic pressure decay to propagation occurs when the circumferential Mach number of the rotating mode reaches a critical value. Because the axial Mach number was less than 0.2, the effect of the convection velocity was neglected in this initial investigation.

The sound field in an annular duct with no mean flow can be expressed as

$$p(r, \theta, x, t) = \sum_{m,n} p_{mn} E_{mn}(k_{mn}r) \exp i(a_{mn} k_{mn} x + m\theta - \omega t), \quad (1)$$

where  $m$  is the circumferential mode order, which can be positive (corotation) or negative (counterrotation) relative to the direction of rotation of the rotor. The radial mode order is indicated by  $n$ .



The coefficient of the wave number in the axial direction,  $a_{mn}$ , is given by:

$$a_{mn} = \frac{k_x}{k_{mn}} = \sqrt{1 - \frac{1}{\gamma^2}}, \quad (2)$$

where  $\gamma$  is the cutoff ratio, defined by the ratio of the frequency of the rotating mode  $f$  and its cutoff frequency,  $f^*$ . The cutoff frequency is related to the characteristic wave number of the mode  $k_{mn}$  and the sound speed as:

$$f^* = \frac{k_{mn} c}{2\pi}.$$

In equation (1),  $E_{mn}$  is the radial pressure distribution function formed by the Bessel function of the first kind,  $J$ , and the second kind,  $Y$ ; i.e.:

$$E_{mn} = C_{mn} [J_m(k_{mn} r) + Q_{mn} Y_m(k_{mn} r)] \quad (3)$$

The values of  $Q_{mn}$  and  $k_{mn}$  are determined by the boundary conditions. The radial pressure gradient must be zero at the inner and outer walls, therefore:

$$J'_m(k'_{mn}) + Q_{mn} Y'_{mn}(k'_{mn}) = 0$$

and

$$J'_m(k'_{mn} \sigma) + Q_{mn} Y'_{mn}(k'_{mn} \sigma) = 0, \quad (4)$$

where  $k'_{mn}$  is the characteristic wave number,  $k_{mn}$ , normalized by the outer radius,  $r_b$ . The hub-tip radius ratio is  $\sigma$ . The orthogonality

of the characteristic functions requires that

$$\int_{r_a}^{r_b} E_{mn}(r) E_{\mu\nu}(r) 2\pi r dr = \begin{cases} 0 & \mu, \nu \neq m, n \\ 1 & \mu, \nu = m, n \end{cases} \quad (5)$$

The square of the modal pressure represents the power of the modes; thus, the normalized constant,  $C_{mn}$ , ensures that the integral of  $p^2$  across the duct is unity. Combining Equations (3) and (5) gives, for the value of  $C_{mn}$ :

$$\frac{1}{\pi C_{mn}^2} = \left[ 1 - \left( \frac{m}{k'_{mn}} \right)^2 \right] \left[ J_m(k'_{mn}) + Q_{mn} Y_m(k'_{mn}) \right]^2 - \left[ \sigma^2 - \left( \frac{m}{k'_{mn}} \right)^2 \right] \left[ J_m(k'_{mn} \sigma) + Q_{mn} Y_m(k'_{mn} \sigma) \right]^2 \quad (6)$$

If the frequency of the exciting source of a mode exceeds the cutoff frequency of that mode, the acoustic pressure propagates, and the wave front travels at a helix angle,  $\alpha$ , relative to the axial direction. The value of  $\alpha$  is given by:

$$\alpha = \sin^{-1} (1/\gamma) \quad .$$

For the plane wave, the propagation direction is purely axial, i.e.,  $\alpha = 0^\circ$ . For higher order spinning modes just at cutoff, the wave fronts rotate in the circumferential direction, i.e.,  $\alpha = 90^\circ$ .

The value of the characteristic constants for the AFRF geometry are:  $k'_{10} = 1.425$ ;  $Q_{10} = 0.258$ ;  $C_{10} = 1.018$ .

### 3.2 Aerodynamic Lift Prediction

Whitehead [3, 4] represented a thin zero-camber cascade by a number of equally spaced vortices with continuously varying strength to obtain a solution of the chordwise pressure distribution for various forms of perturbation. Smith [6] modified Whitehead's model to include compressibility effects. The unsteady lift results referred to later in this thesis are obtained by integration of the unsteady pressures obtained from Smith's program for the gust perturbation case and are referred to as the Whitehead-Smith Theory.

Using the theory developed by Henderson [5], Shen [33] obtained an explicit solution for the unsteady pressure distribution along the chord of a blade in a two-dimensional cascade caused by spatial inflow velocity variations. The results from this theory are referred to as the Henderson-Shen theory. The method employed is a Singularity Vortex Method, which has been widely used in thin-airfoil theory. However, the solution includes the effects of mean incidence angle, blade camber, and space-chord ratio, which are important parameters in the analysis of the unsteady lift of a blade in a cascade.

Some important assumptions of their model are: (1) the flow is two-dimensional, inviscid, and incompressible, (2) the disturbance velocities are small compared with the mean velocity,  $W_m$ , and (3) the camber of the foil is small so that the boundary condition is considered to be on the chord line rather than the camberline. The resulting unsteady lift  $\tilde{L}$  can be expressed as:

$$\tilde{L} = \tilde{C}_L \pi \rho C A_f W_m \bar{V}_x S \quad , \quad (7)$$

where  $\tilde{C}_L$  is the complex unsteady lift coefficient which is a function of reduced frequency and of the cascade operation parameters. In the present experimental study: (1) the Mach number was less than 0.1 for all test cases; (2) the designed fundamental harmonic,  $A_f$ , of the distortion screens was 0.2; and (3) the maximum camber-to-chord ratio was 0.11 percent at the midspan, i.e., the location of the instrument blade segment. These conditions are considered appropriate for a linearized analysis. Also, the velocity field impinging on the rotor was designed to be purely axial, and the one-inch blade segment was centered at midspan of the rotor where the flow would be two-dimensional.

### 3.3 Coupling of Unsteady Lift to Acoustic Modal Pressures

The unsteady lift can be calculated from the Henderson-Shen prediction program as a function of spanwise location. For plane wave excitation, the velocity distortion harmonic and the rotor blade number are the same, so the lift on all the blades will be in phase. For the higher order (1,0) mode, there is a phase difference between the unsteady lift on each blade since the distortion harmonic is different from the blade number. However, this effect is considered in the lift prediction program by specifying the inter-blade phase angle. The Tyler-Sofrin analysis is then employed to obtain the acoustic pressure so that the total effect can be obtained simply by multiplying the lift from one blade by the total number of blades.

Due to the blade stagger and the propagation helix angles, the lift vector will, in general, not be aligned with the wave front. Consequently, the lift must be resolved into the direction of the wave front as shown in Figure 16. Furthermore, the unsteady lift along

the span of a blade must be weighted spatially by the radial mode shape function  $E_{mn}(r)$  and summed temporally to get the resultant unsteady force. This resultant unsteady force is multiplied by the total number of blades and divided by the duct area to obtain the acoustic modal pressure  $p_{mn}$ , i.e.:

$$p_{mn} = \frac{B}{\pi(r_b^2 - r_a^2)} \sum_{r_a}^{r_b} E_{mn}(r) \tilde{L} \sin(\xi + \alpha) \quad (8)$$

This coupling scheme agrees with the exact solution to the wave equation as described by Mani [8]; the comparison is described in Appendix E.

The flow chart of the noise prediction program is shown in Figure 17. In the experiment, the plane wave and the first higher order mode (1,0) were of main interest. For the nine-bladed AFRF rotor, the velocity distortion harmonics  $A_8$ ,  $A_9$ , and  $A_{10}$  excite the (+1,0) mode, plane wave, and (-1,0) mode, respectively. Figures 18 and 19 show these harmonics versus free-stream velocity at three radial locations. These values were read into the prediction program and were interpolated to obtain the values corresponding to the operating conditions. The local mean axial velocity  $\bar{V}_x$  at each spanwise segment was also obtained from interpolation of the measured velocity profiles.

Because of the duct termination of the inlet opening and the presence of rotor blades, a standing wave will result from the net effect of the outgoing and reflected waves between these two planes. To find the coupling coefficient between the unsteady lift and acoustic modal pressure, it is necessary to decompose the measured acoustic

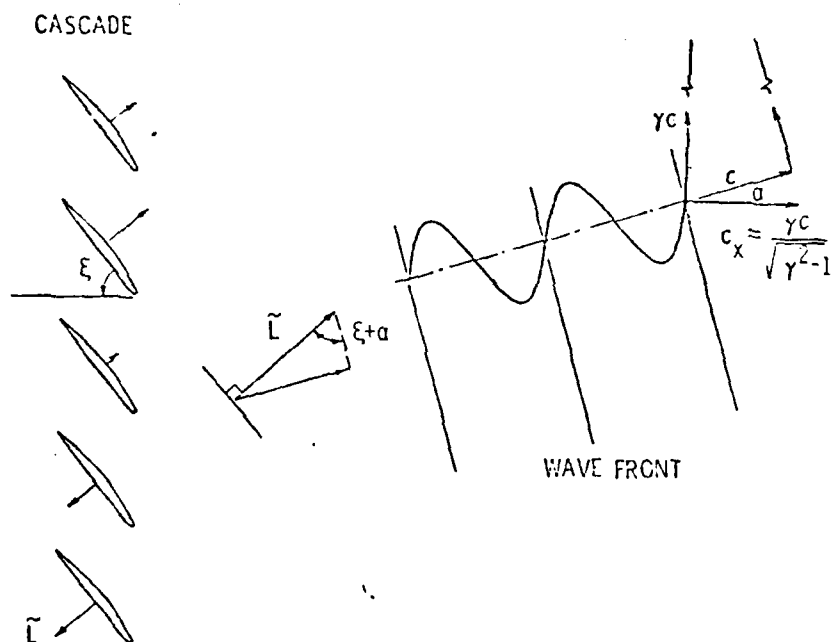


Figure 16 Resolution of Unsteady Lift to Acoustic Wave Front of Higher Order Modes

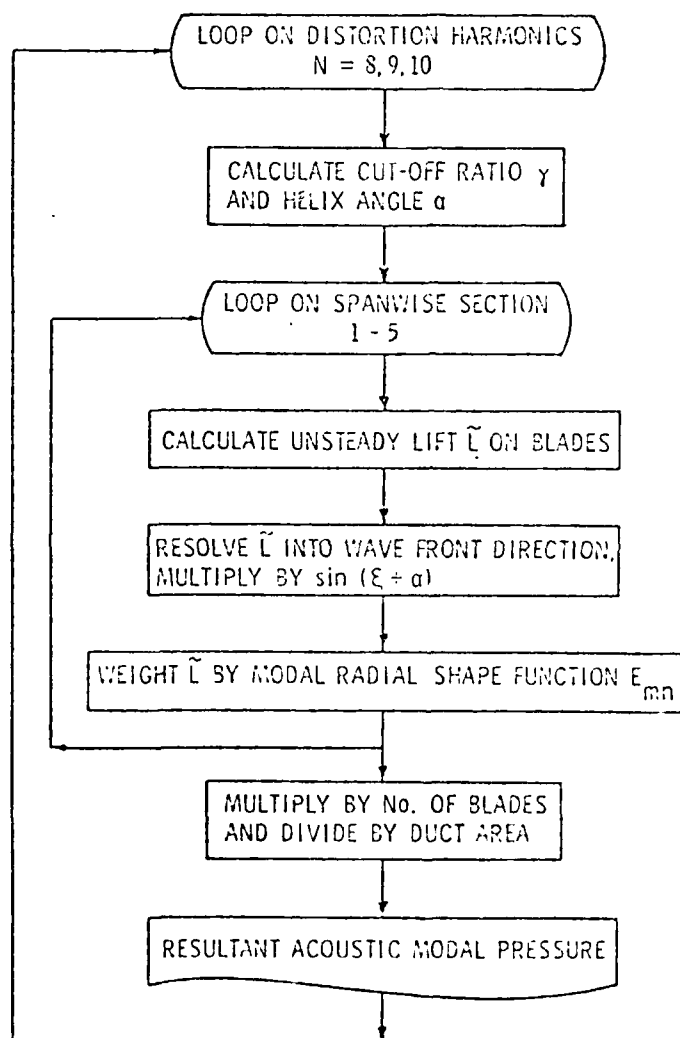


Figure 17 Flow Chart of Acoustic Modal Pressure Prediction

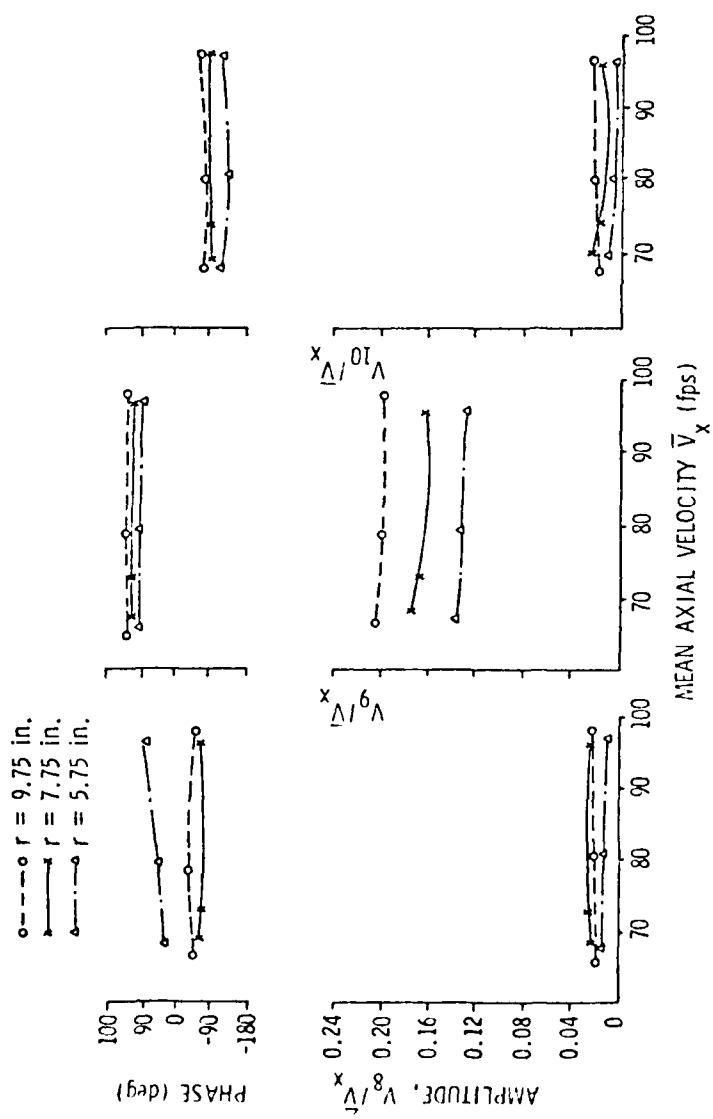


Figure 18 Fourier Harmonics of Nine-Cycle Screen versus Mean Axial Velocity



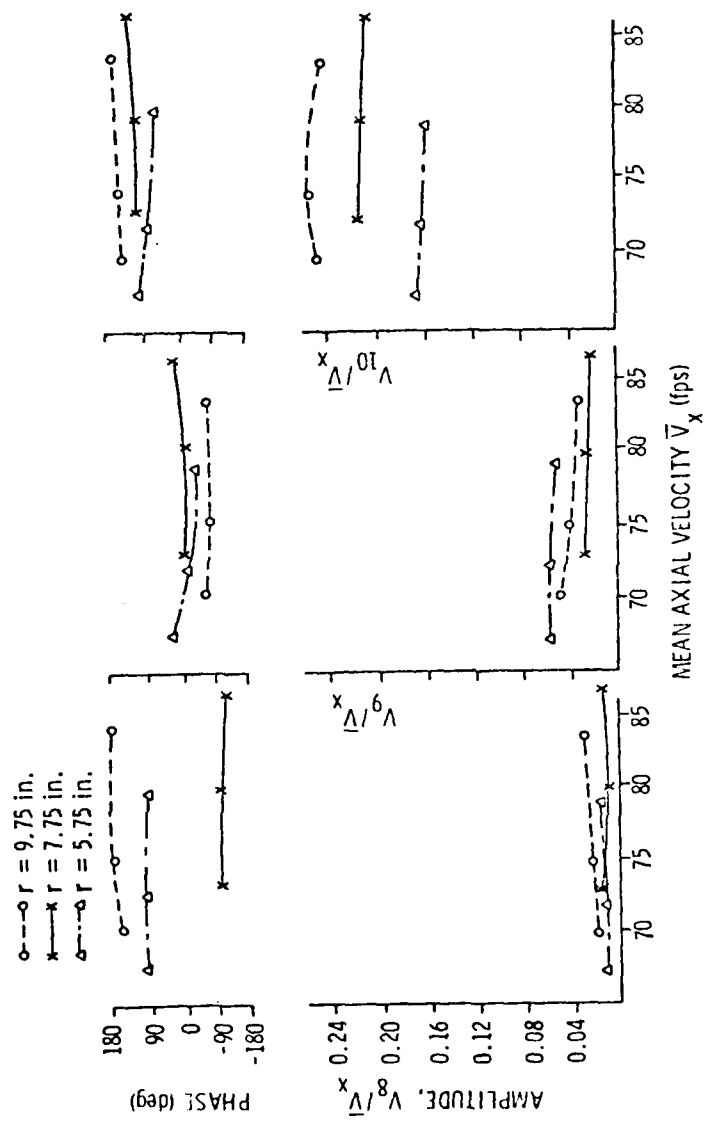


Figure 19 Fourier Harmonics of Ten-Cycle Screen versus Mean Axial Velocity

pressures at BPF into their modal components with the reflection effects removed. A modal decomposition program was written to calculate the modal pressures at the source from the microphone measurements. A detailed discussion of the effect of reflection and modal decomposition is presented in Appendix F.

### 3.4 Comparison of Experimental Results with Theoretical Predictions

#### 3.4.1 Distortion Screens

The desired characteristics of the flow field are that the magnitude of the fundamental harmonic, non-dimensionalized by the free-stream velocity, has a value of 0.2, while all other harmonics are relatively small. In order to obtain a strong discrimination between the plane wave and  $(-1,0)$  mode, the fundamental screen circumferential harmonic must be distinctly larger than its neighboring ones. Specifically,  $A_9$  should be large relative to  $A_8$  and  $A_{10}$  for the nine-cycle screen and  $A_{10}$  should be large relative to  $A_8$  and  $A_9$  for the ten-cycle screen.

The results of the Fourier analysis of the velocity fields downstream of the distortion screens are shown in Figures 20 and 21. It was found that the fundamental harmonics for both screens were near 0.2 as designed. For the plane wave excitation, nine-cycle screen, the largest neighboring distortion harmonic is  $A_8$ , which is 14.6 percent of  $A_9$ . The  $(1,0)$  mode excited by  $A_8$ , in this case, will decay when the BPF is below the cutoff frequency of 280 Hz. Above the cutoff frequency, it will have a contribution to the acoustic measurement.

For excitation of the  $(-1,0)$  mode, the most significant neighboring harmonic is  $A_9$ , which is 36.3 percent of  $A_{10}$  near the hub and 13.8 percent near the tip. The plane wave excited by  $A_9$ , when the ten-cycle

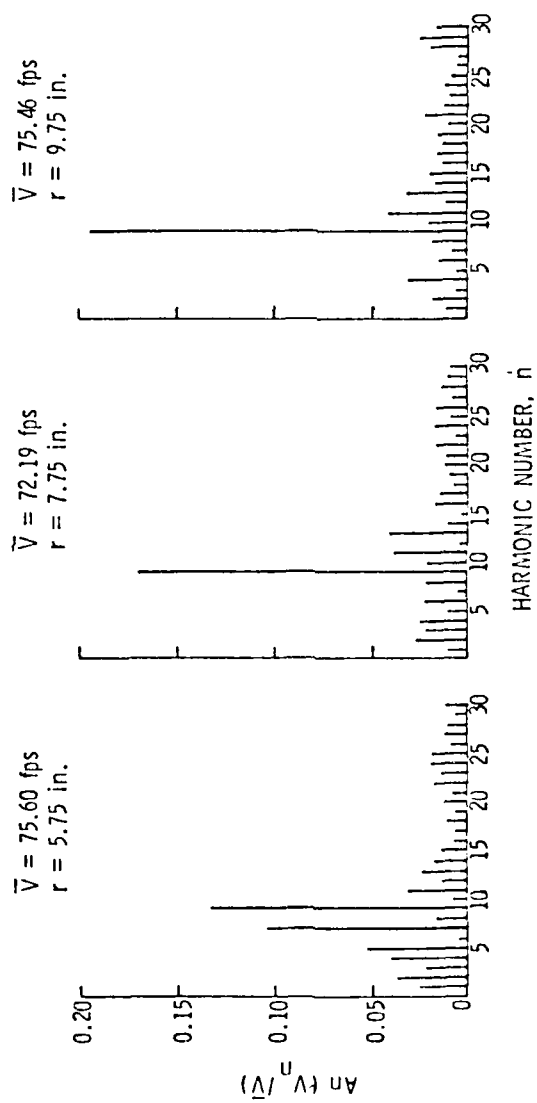


Figure 20 Amplitudes of Fourier Harmonics of Nine-Cycle Screen

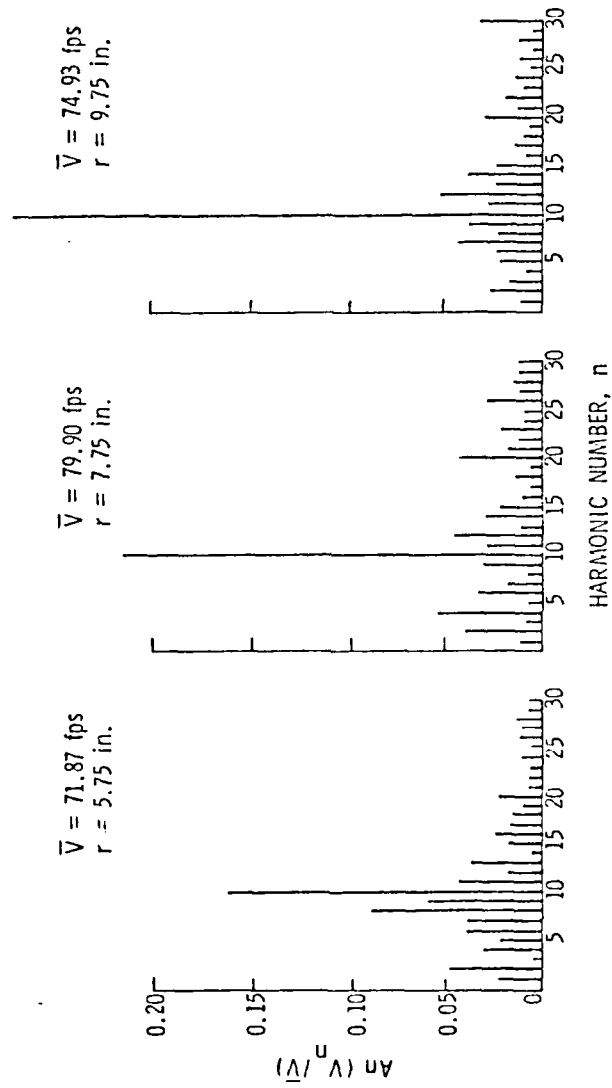


Figure 21 Amplitudes of Fourier Harmonics of Ten-Cycle Screen

screen was used to generate the  $(-1,0)$  mode, will always propagate and, therefore, its presence cannot be neglected. The presence of all these modes was considered in the decomposition of the acoustic pressures, i.e., the measurements were decomposed into the plane wave and the  $(-1,0)$  mode.

The largest harmonic, other than the screen fundamental, appears near the hub. For the nine-cycle screen, it is  $A_7$  which is 85 percent of  $A_9$  and for the ten-cycle screen, it is  $A_8$  which is 55 percent of  $A_{10}$ . However, they only contribute to exciting the  $(+2,0)$  mode. In the experiment, BPF was near 280 Hz which is well below the cutoff frequency of the  $(2,0)$  mode, i.e., 550 Hz.

Tyler and Sofrin [10] gave an expression for the decay rate of the acoustic pressure when the cutoff ratio is less than one:

$$\frac{\Delta \text{dB}}{x} = 8.69 \frac{2\pi}{c} \sqrt{f^{*2} - f^2} \quad (9)$$

A plot of this equation for the various modes of the AFRF is shown in Figure 22. For the  $(2,0)$  mode, the decay rate is 21 dB/ft near 280 Hz and each higher order mode decays even faster. Therefore, all the modes higher than the  $(1,0)$  mode can be neglected over the operating speed range investigated.

Figures 20 and 21 also show that the worst screen performance occurred near the hub. However, the magnitude of the unsteady blade pressure is a minimum at the hub. This follows because the blade chord is constant along the span so the reduced frequency is about the same from hub to tip and, thus, the section lift coefficient is about

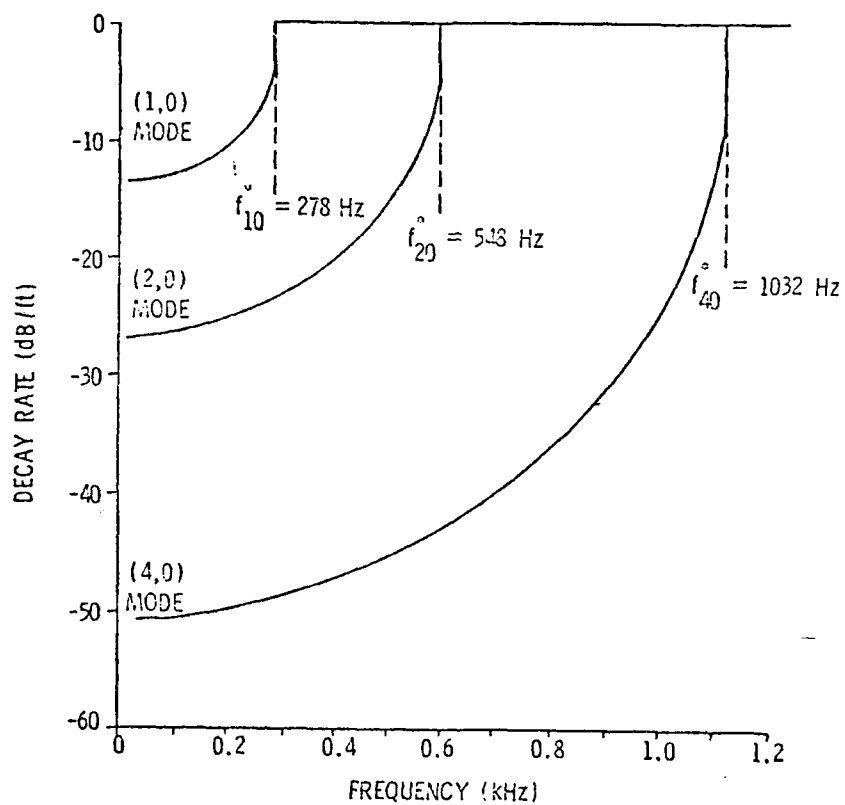


Figure 22 Decay Rate of Modal Pressure in the Axial Flow Research Fan (AFRF)

constant along the span. However, the unsteady lift is proportional to the square of the relative velocity,  $W_m$  for a constant ratio of  $W_d/W_m$  and, thus, the contribution to the unsteady pressure near the hub is small because the local relative velocity is low relative to the remainder of the span.

### 3.4.2 Unsteady Lift

Figures 23 to 25 show typical results of the unsteady lift measurement for the signal analyses: spectrum average (function 4), waveform average (function 12), and waveform average/FFT (function 13), respectively.

In Figure 25, the largest harmonic,  $N = 16$ , resulted from the mechanical resonance of the lift gage near 500 Hz, since 1854 rpm corresponds to 494 Hz for the sixteenth harmonic ( $1854 \times 16/60 = 494.4$ ). This peak moved to higher values of  $N$  as the shaft speed decreased.

Measurement and prediction of unsteady lift versus rotor speed for different test conditions are presented in Figures 26 to 29. It is apparent that there was a strong back-reaction influence on the unsteady lift magnitude as well as phase for both the nine- and ten-cycle screens, which occurred near 245 Hz (1630 rpm for the nine-cycle screen and 1470 rpm for the ten-cycle screen). The theoretical prediction is in good agreement with the measurement for the ten-cycle screen except for the variation caused by the back-reaction effect. However, the discrepancy between measured and predicted lift values were rather large for the nine-cycle screen cases.

The unsteady lift coefficients at different spanwise sections for the test cases are listed in Table III. Operating at the two flow

TABLE III  
UNSTEADY LIFT COEFFICIENTS OF THE TEST CASES

Radius r(inch)	Distortion Harmonic N	Reduced Frequency $\lambda$	Unsteady lift coefficient					
			Whitehead- Smith theory		Henderson-Shen theory			
					$\phi = 0.56$		$\phi = 0.70$	
			Mag.	Phase	Mag.	Phase	Mag.	Phase
5.35	8	2.312	0.099	130.96	0.1614	146.25	0.1976	146.90
	9	2.601	0.0854	144.95	0.2780	128.05	0.3091	130.03
	10	2.890	0.1127	151.85	0.1482	143.47	0.1815	143.71
6.55	8	2.473	0.1744	126.82	0.1633	128.44	0.1942	130.20
	9	2.782	0.1295	135.39	0.3146	91.73	0.3369	95.47
	10	3.091	0.1587	147.33	0.2020	133.40	0.2274	133.76
7.75	8	2.382	0.2085	126.29	0.1580	120.18	0.1863	122.22
	9	2.679	0.1695	129.66	0.3663	85.85	0.3878	89.08
	10	2.977	0.1943	142.28	0.2413	135.42	0.2610	135.17
8.95	8	2.217	0.2362	127.03	0.1695	111.49	0.2554	142.39
	9	2.495	0.2043	126.48	0.4400	94.58	0.4659	96.69
	10	2.772	0.2225	137.67	0.2592	141.51	0.2826	140.46
10.15	8	2.045	0.2574	127.79	0.2098	110.01	0.2446	112.72
	9	2.300	6.2311	12480	0.5244	107.15	0.5544	108.24
	10	2.556	0.2447	134.09	0.2769	148.81	0.3034	146.77



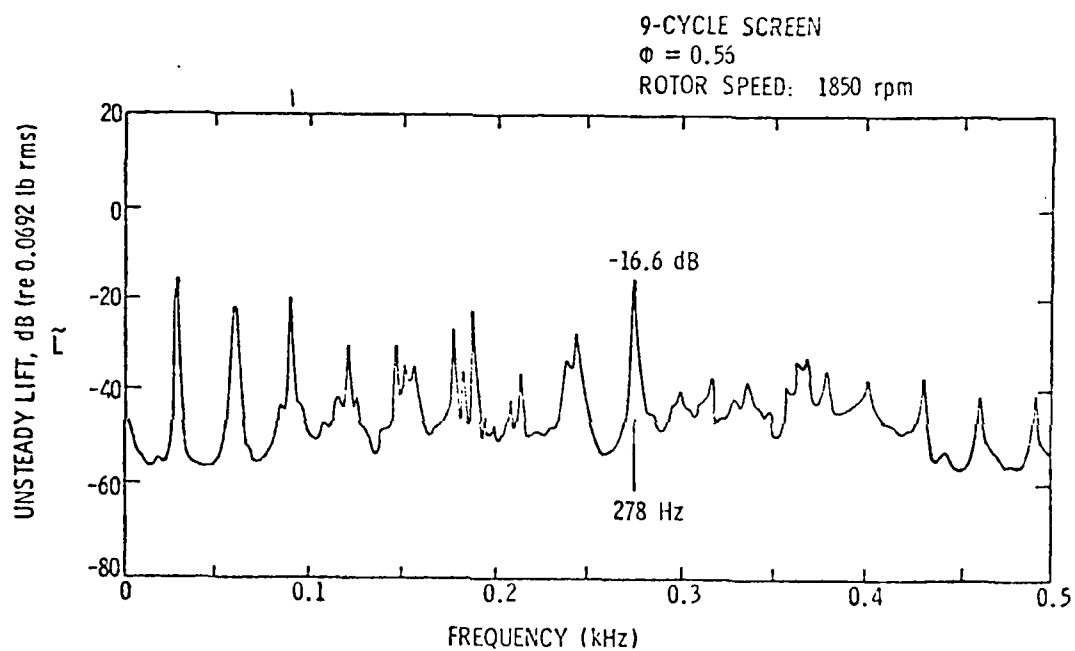


Figure 23 Typical Spectrum of Lift Gage Measurement (Function 4)

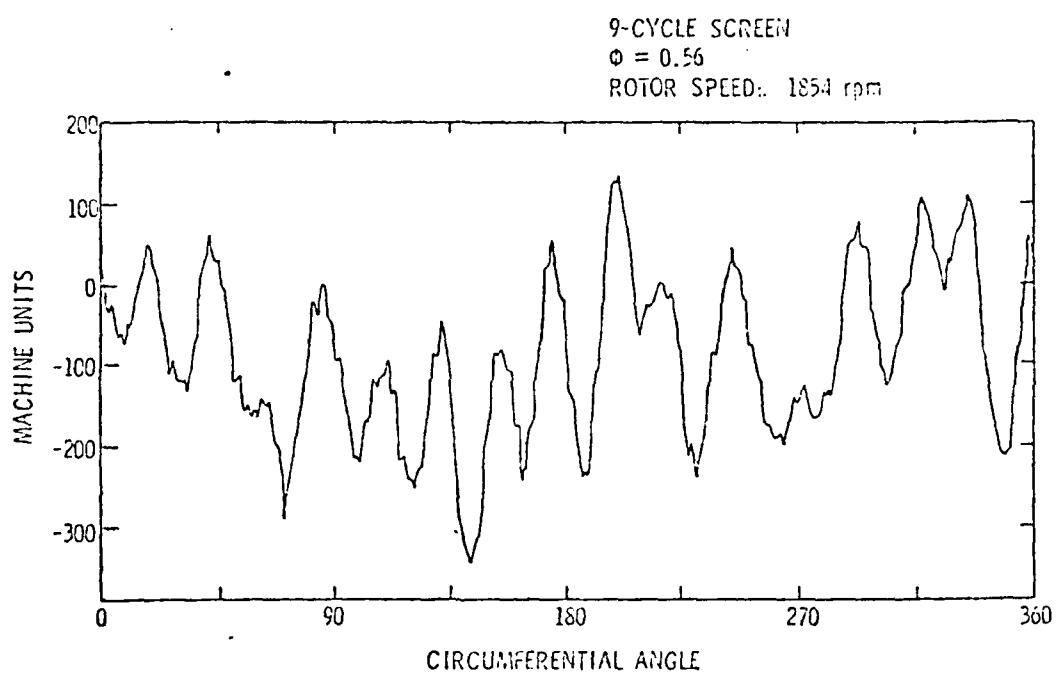


Figure 24 Typical Wave Form of Lift Gage Measurement (Function 12)

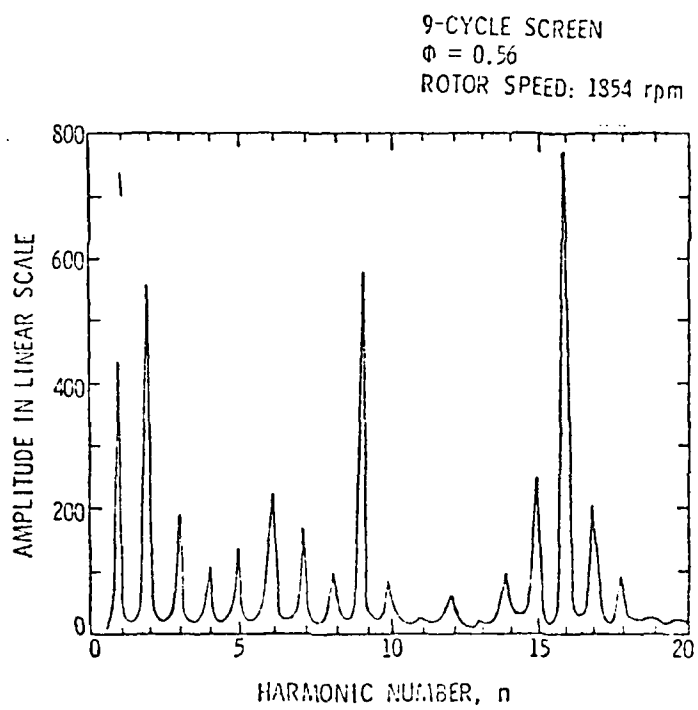


Figure 25 Typical Fourier Harmonics of Lift Gage Measurement (Function 13)

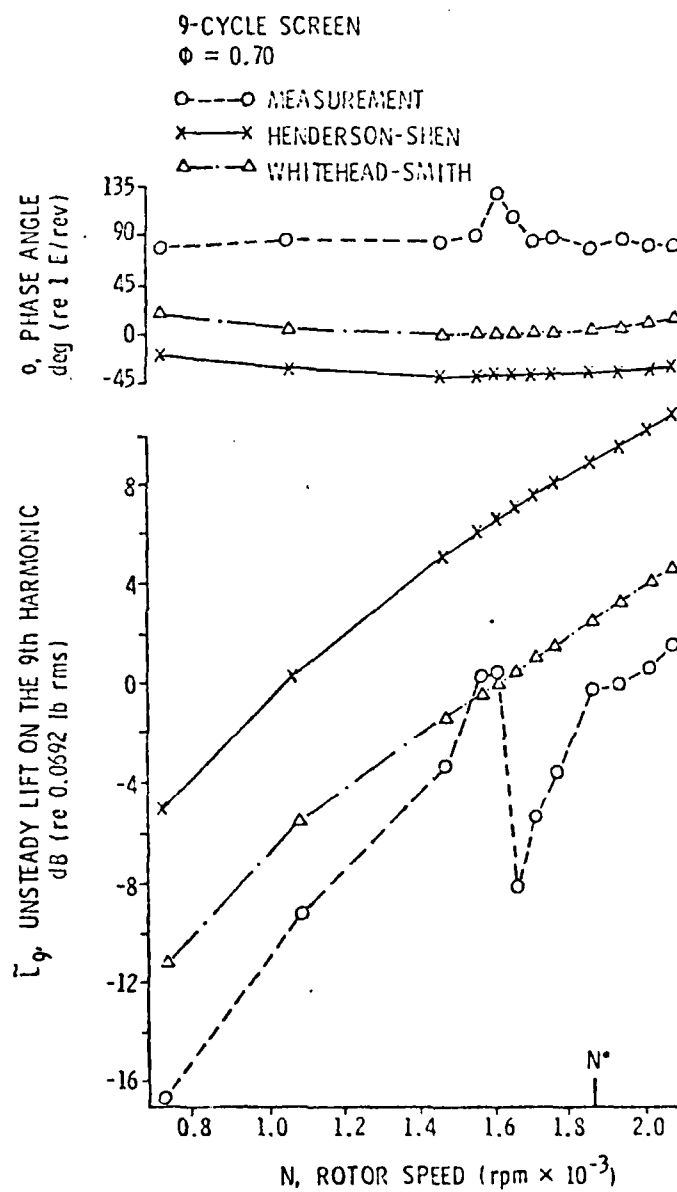


Figure 26 Unsteady Lift of Nine-Cycle Screen versus Rotor Speed ( $\phi = 0.70$ )

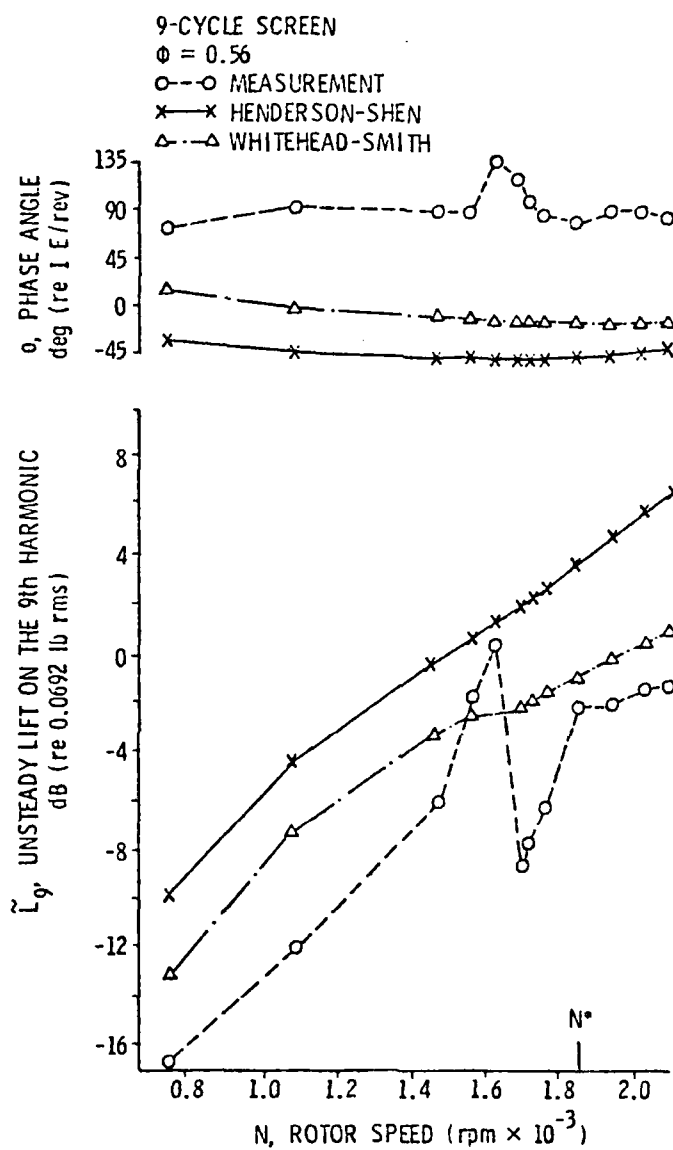


Figure 27 Unsteady Lift of Nine-Cycle Screen versus Rotor Speed ( $\phi = 0.56$ )

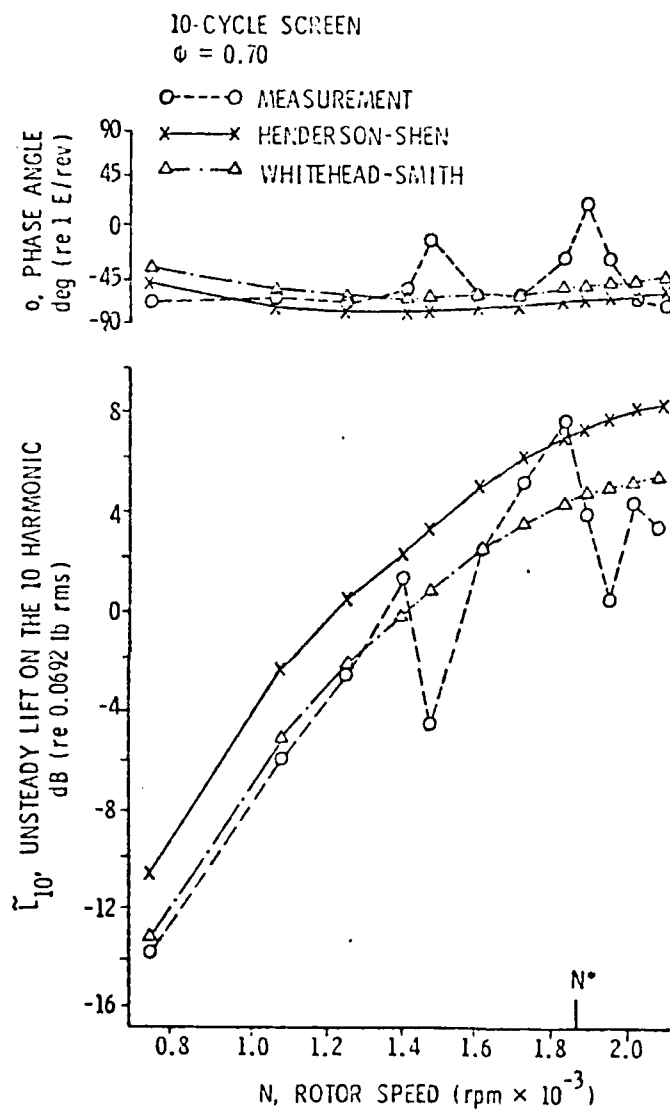


Figure 28 Unsteady Lift of Ten-Cycle Screen versus Rotor Speed ( $\phi = 0.70$ )

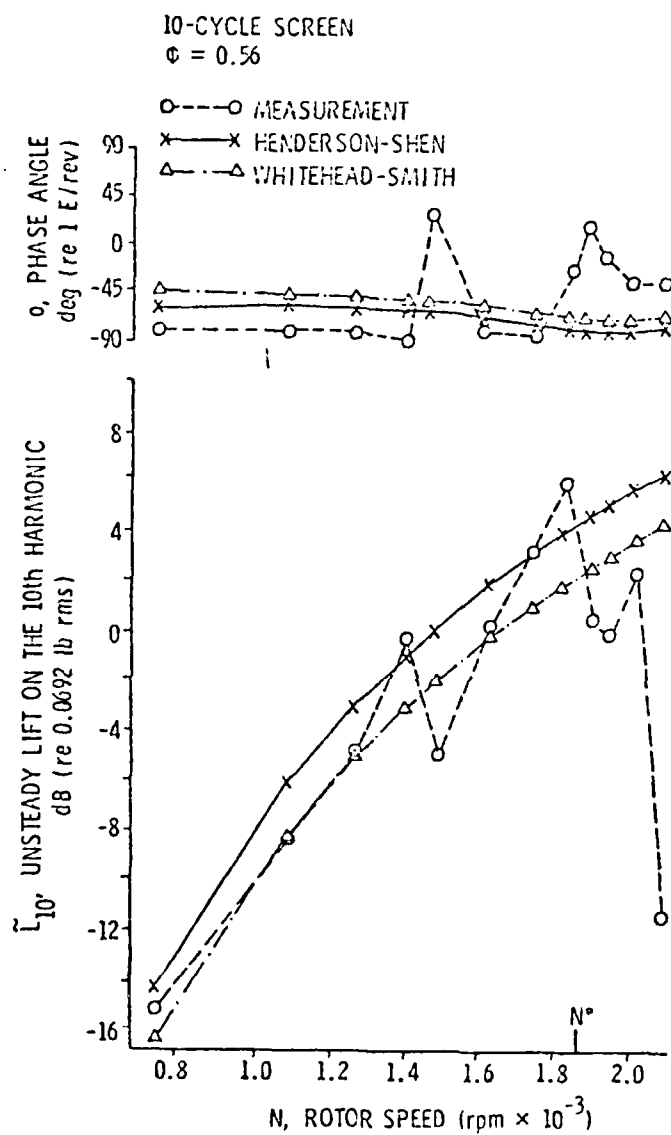


Figure 29 Unsteady Lift of Ten-Cycle Screen versus Rotor Speed ( $\phi = 0.56$ )

coefficients produced different mean incidence angles and, therefore, steady lift values. The steady lift coefficients can be calculated by using the correlation of lift characteristic for blades in cascade, which resulted in values of lift coefficient of 0.328 and 0.683 at midspan for  $\phi = 0.70$  and 0.56, respectively. The mean incidence angles for these flow coefficients are 0.3 and 0.6 degrees, respectively. Note that the steady loading causes a decrease in the magnitude of the unsteady lift coefficient,  $\tilde{C}_L$ , by about ten percent using the Henderson-Shen theory. Because the Whitehead-Smith theory does not include the effect of steady loading on the blades, the value of  $\tilde{C}_L$  remains constant.

When the nine-cycle screen was installed in the nine-bladed fan, the spacing between blades was equal to the wavelength of the distorted inflow, i.e., the interblade frequency approached  $2\pi$ , which is referred to as an "aerodynamic resonance" in a cascade [5]. Henderson-Shen's prediction scheme predicts a significant increase in  $\tilde{C}_L$  near resonance, while the Whitehead-Smith theory does not have a change in  $\tilde{C}_L$  at this resonance point. The measurements showed that  $\tilde{C}_L$  changed in magnitude and phase for the nine-cycle screen relative to that of the ten-cycle screen, and both analyses did not predict this reduction or change in phase angle.

For the ten-cycle cases, the agreement between the Whitehead-Smith theory is excellent when the rotor speeds were less than 1450 rpm. The unsteady lift fluctuated at higher rotor speeds, which apparently is the result of the back-reaction of the strong acoustic field. The Henderson-Shen theory overestimates  $\tilde{C}_L$  by 15 dB in the magnitude; however, the prediction of the phase angle is good. The larger discrep-



ancies in the phase angle from the Whitehead-Smith theory for the cases  $\phi = 0.56$  are expected, since the mean incidence angle was 6.0 degrees, which departed from the zero steady loading of their model.

Bruce [12] has conducted a series of experiments in the AFRF to measure the unsteady lift and moment generated by the disturbance flow field. The comparison of the data measured by Bruce and the predictions [12, 27] also showed the theories tend to overestimate the magnitude of the unsteady lift, while the measured and predicted phase angles were in good agreement even near the aerodynamic resonance. However, the reduced frequencies in Bruce's experiment were 0.2 to 2.0, which were lower than the range of reduced frequencies, 2.7 to 3.0 used in this study. In particular, the reduced frequency near the aerodynamic resonance was 1.3 in Bruce's experiment and 2.7 in this experiment.

#### 3.4.3 Acoustic Pressure

Figure 30 shows the sound pressure level measured at microphone position one over the speed range for the case  $\phi = 0.70$ . The measurements show that the acoustic pressure measured with the nine-cycle screen is practically the same over a large range of rotor speeds. For the ten-cycle screen, a cutoff phenomenon was observed near 1850 rpm as predicted. Thus, the acoustic pressure was dominated by the plane wave mode for the nine-cycle screen and by the  $(-1,0)$  mode for the ten-cycle screen, as designed.

The complete data of the magnitude and phase angle of the acoustic pressures measured at four microphone locations are listed in Table IV and V. These data were used as the input to the modal decomposition program described in Appendix F. The resulting decomposed modal

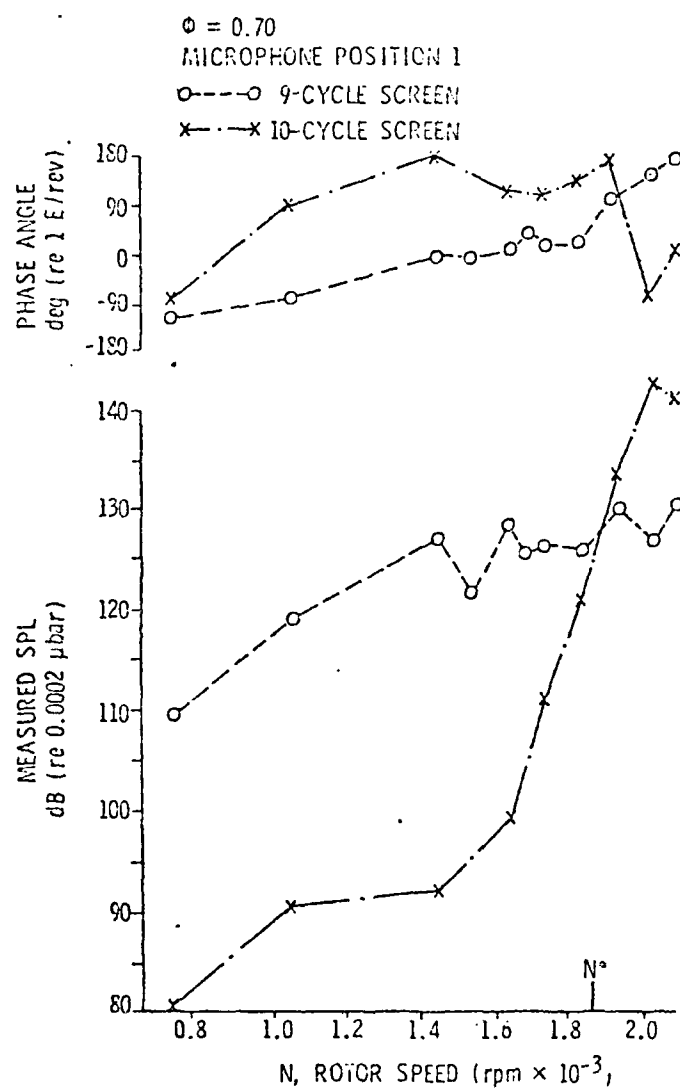


Figure 30 Typical SPL Measurements versus Rotor Speed

TABLE IV  
SOUND PRESSURE LEVEL MEASUREMENT — NINE-CYCLE DISTORTION SCREEN

Flow Coefficient				0.56						0.70							
Microphone Position		1		2		3		4		1		2		3		4	
RPM/SPL	dB	deg.		dB	deg.	dB	deg.	dB	deg.	dB	deg.	dB	deg.	dB	deg.	dB	deg.
2100.	128.4	133.1	120.8	-126.6	123.6	-64.5	126.8	85.6	128.9	140.9	121.2	-165.1	125.6	-53.8	124.3	99.1	
2038.	123.5	122.8	125.6	-129.2	125.5	-50.8	128.0	103.0	124.6	120.6	125.5	-121.9	126.0	-65.4	129.4	103.4	
1948.	126.1	63.8	127.4	-142.2	123.4	-111.0	127.1	68.1	128.0	68.3	128.5	-147.8	124.4	-125.4	128.0	71.7	
1854.	123.6	48.4	121.8	153.6	123.4	-113.5	124.7	9.3	124.4	1.8	123.4	152.8	124.1	-117.4	126.3	9.6	
1760.	124.5	51.4	123.1	144.9	122.4	-118.7	124.6	11.3	124.9	4.0	123.4	146.5	123.3	-120.0	125.8	13.8	
1714.	123.2	19.1	124.7	137.6	125.6	-120.3	124.5	37.8	124.2	18.8	125.9	137.7	126.3	-122.3	125.8	36.4	
1668.	126.0	40.3	124.9	129.8	123.0	-177.8	126.5	-6.7	126.7	-1.8	126.0	128.9	123.6	-172.5	127.4	-11.4	
1574.	119.4	-25.9	120.4	3.2	120.1	-141.7	118.9	-41.3	120.6	-28.9	121.8	3.2	121.2	-137.5	120.1	-41.2	
1480.	121.0	-10.3	117.7	76.7	120.8	-109.0	122.2	-25.0	122.3	-18.1	118.0	71.3	121.3	-114.0	122.7	-22.0	
1110.	116.2	-91.7	118.8	-75.3	118.1	94.2	115.1	-98.9	118.2	-96.7	120.8	-71.2	119.9	99.3	117.0	-105.5	
742.	108.4	-148.6	107.0	-143.9	100.2	168.2	108.4	-138.1	109.4	-168.4	107.3	-144.6	100.3	169.5	109.4	-136.5	

TABLE V  
SOUND PRESSURE LEVEL MEASUREMENT — TEN-CYCLE DISTORTION SCREEN

Flow Coefficient Microphone Position		0.56								0.70							
		2				3				4				1			
		dB	deg.	dB	deg.	dB	deg.	dB	deg.	dB	deg.	dB	deg.	dB	deg.	dB	deg.
2100.	137.5	-15.8	135.2	112.6	123.0	166.6	136.7	-169.6	139.6	-22.8	137.5	111.7	124.2	152.4	137.9	-166.6	
2038.	139.2	-107.5	137.6	18.5	136.3	100.9	139.0	91.2	142.0	-110.9	139.8	18.1	138.2	110.1	141.0	98.3	
1946.	130.5	141.7	128.1	-69.2	135.5	14.8	131.6	9.8	132.1	143.7	126.9	-64.6	135.3	21.8	131.7	19.2	
1854.	119.8	110.6	117.8	-136.8	131.1	-25.1	124.6	-13.4	121.4	112.9	117.8	-134.5	133.0	-29.2	124.6	-16.8	
1760.	107.5	77.2	99.5	-153.3	119.2	-38.1	110.1	-84.8	109.4	76.8	102.8	-150.2	121.8	-86.5	111.2	-72.9	
1668.	94.7	127.8	95.0	-64.6	113.8	-27.6	101.7	-78.0	97.4	105.9	100.7	-78.8	116.4	-39.8	104.8	-48.6	
1480.	82.0	162.8	89.8	-90.0	105.0	-18.0	88.8	-47.2	92.2	148.8	93.7	-86.1	108.1	-35.2	92.8	-149.4	
1110.	83.6	142.1	90.2	-168.5	98.0	-13.0	81.4	128.3	91.0	99.3	93.5	134.9	101.3	-45.4	86.4	107.6	
742	69.1	-148.8	73.8	-129.0	89.6	-39.5	75.4	34.2	79.2	-97.6	74.9	-23.6	89.6	-51.2	76.8	27.0	

pressures are shown in Figures 31 to 34. The plane wave was found to be larger than the  $(-1,0)$  mode by 6 to 11 dB for the nine-cycle screen, and the  $(-1,0)$  mode was larger than the plane wave by 16 to 17 dB for the cases above the cutoff frequency. The discrimination between the two modes had a low value at cutoff, about 6 dB for the nine-cycle screen and 4 dB for the ten-cycle screen.

The reason for the poor discrimination between the two modes at cutoff may be caused by the reflection coefficient of the rotor being large which may be associated with the observed back-reaction effect. The reflection coefficient of the rotor at all other conditions is theoretically very low and, for that reason, it was not included in the decomposition scheme.

It is important to know whether the SPL measured by the microphone was influenced by the unsteady pressure of the aerodynamic field or not. This can be checked by considering the unsteady aerodynamic pressure on the blades as a potential field of a flow passing a wave-shaped wall. Shapiro [34] indicated that the decay rate of hydrodynamic pressure of this field in the direction perpendicular to the wall is  $\exp[-2\pi\sqrt{1-M^2} x/S]$ , where  $M$  is the Mach number of the flow, and  $S$  is the wavelength of the wall, which corresponds to the spacing between the blades in this application. Setting  $S = 0.625$  ft at the tip,  $M \approx 0.17$  at 2100 rpm, the highest circumferential speed of the test cases, the resultant decay rate is -86.0 dB/ft. The highest value of unsteady aerodynamic pressure on the outer one-inch of the blade span is 150 dB at 2100 rpm. Therefore, the above formula indicates it will decay to -7.7 dB when it reaches the nearest microphone position of 22

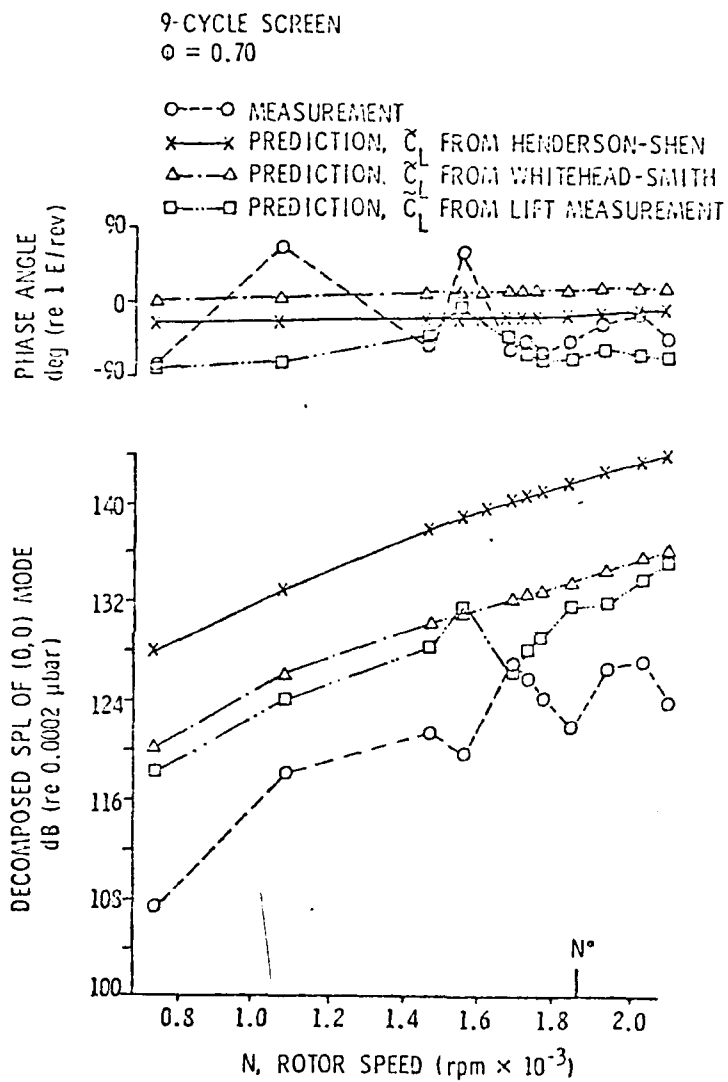


Figure 31 Decomposed Modal Pressure of Nine-Cycle Screen ( $\phi = 0.70$ )

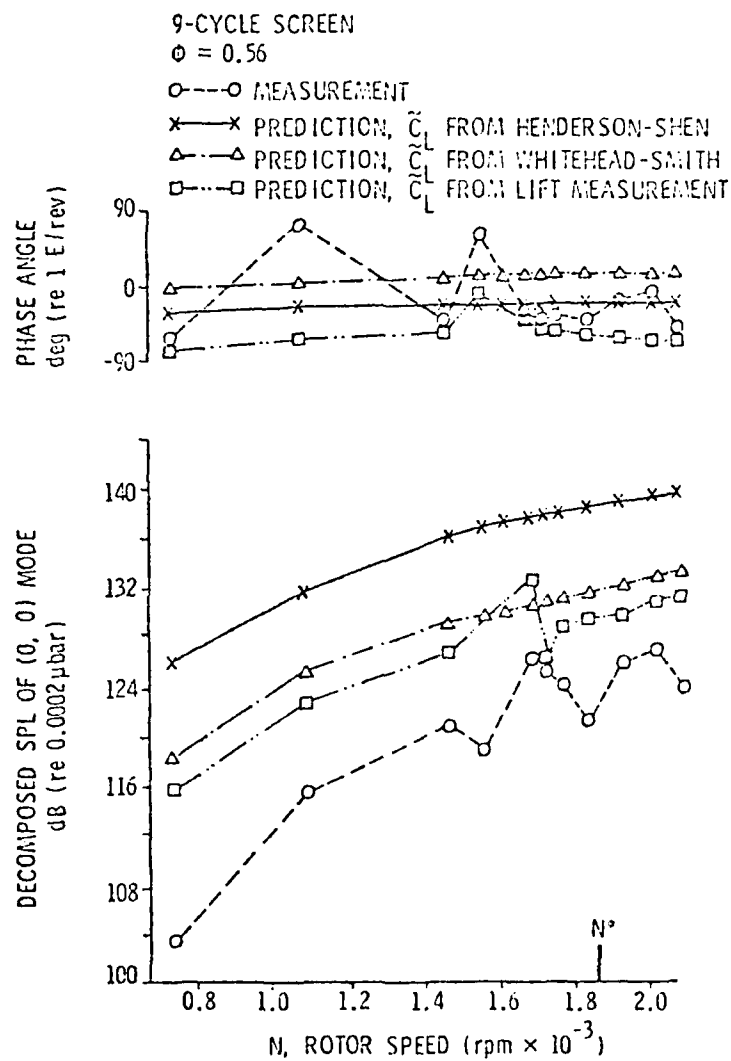


Figure 32 Decomposed Modal Pressure of Nine-Cycle Screen ( $\phi = 0.56$ )

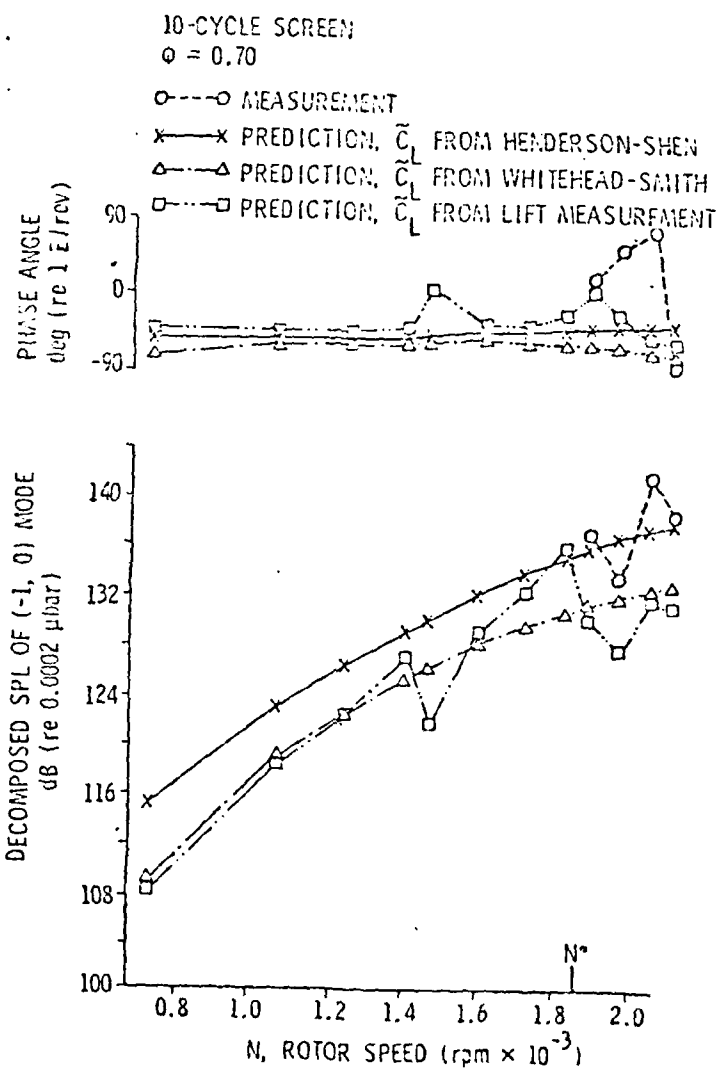


Figure 33 Decomposed Modal Pressure of Ten-Cycle Screen ( $\phi = 0.70$ )



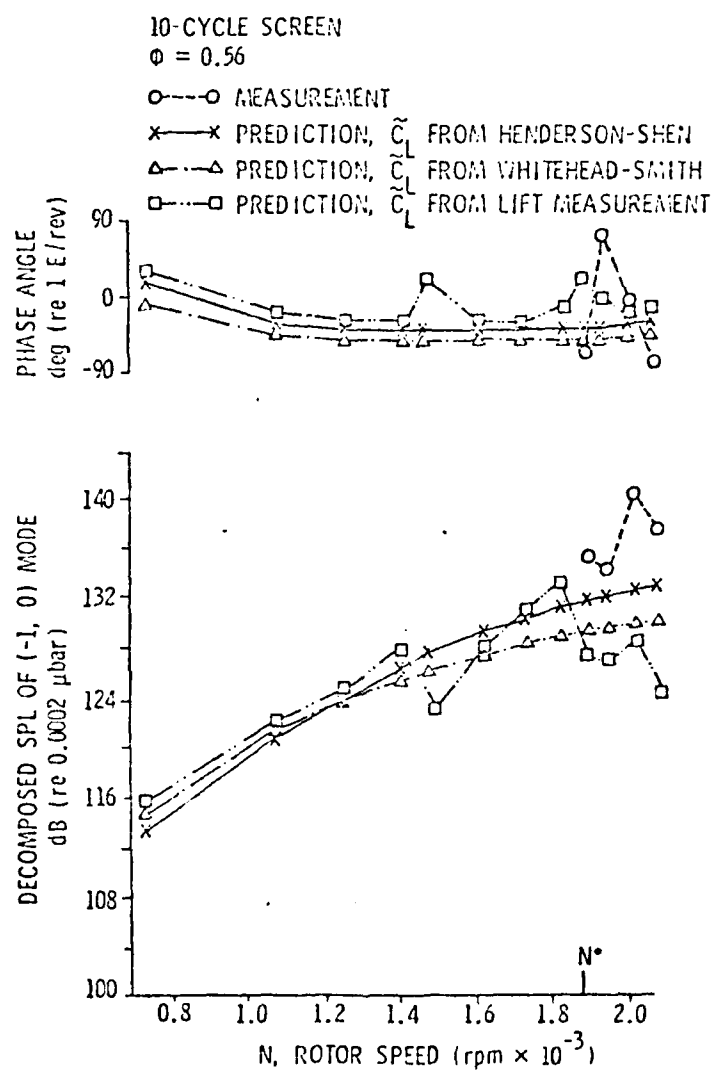


Figure 34 Decomposed Modal Pressure of Ten-Cycle Screen ( $\phi = 0.56$ )

inches from the rotor. This value is well below the typical measured SPL value of 130 dB. Thus, there will be no contribution of the unsteady hydrodynamic field to the acoustic measurement.

The values of the reflection coefficient of the plane wave at the duct opening,  $R$ , obtained from the decomposition program are plotted in Figure 35. It can be seen that  $R$  is always less than unity as expected; however, it varies with the distortion screens and flow coefficient. The solid line represents the prediction of  $R$  by the Morfey theory as described in Appendix F. The large discrepancies between measurement and prediction indicates that the reflection mechanism could be more complicated than the theoretical model considered in the present analysis.

The prediction of the modal sound pressure level (SPL) for different values of unsteady lift coefficient,  $\tilde{C}_L$ , is also plotted in Figures 31 to 34. For the plane wave excitation, the predicted SPL was found to be always higher than the decomposed value. The discrepancy was: about 15 dB using  $\tilde{C}_L$  from the Henderson-Shen theory, and about 9 dB using  $\tilde{C}_L$  from the Whitehead-Smith theory. Prediction of the plane wave pressure using the unsteady lift coefficients obtained from the previous lift gage measurement was also computed, and it was still higher than the decomposed SPL by 7 dB. For the  $(-1,0)$  mode excitation, the decomposed modal pressure can be obtained only when the rotor speed was above cutoff, since the  $(-1,0)$  mode decays quickly along the duct when the cutoff ratio is less than unity. The predicted SPL using the  $\tilde{C}_L$  derived in the three above ways underestimated the modal pressure for most cases. The agreement of the phase angle between prediction and measurement was not good for both screens.

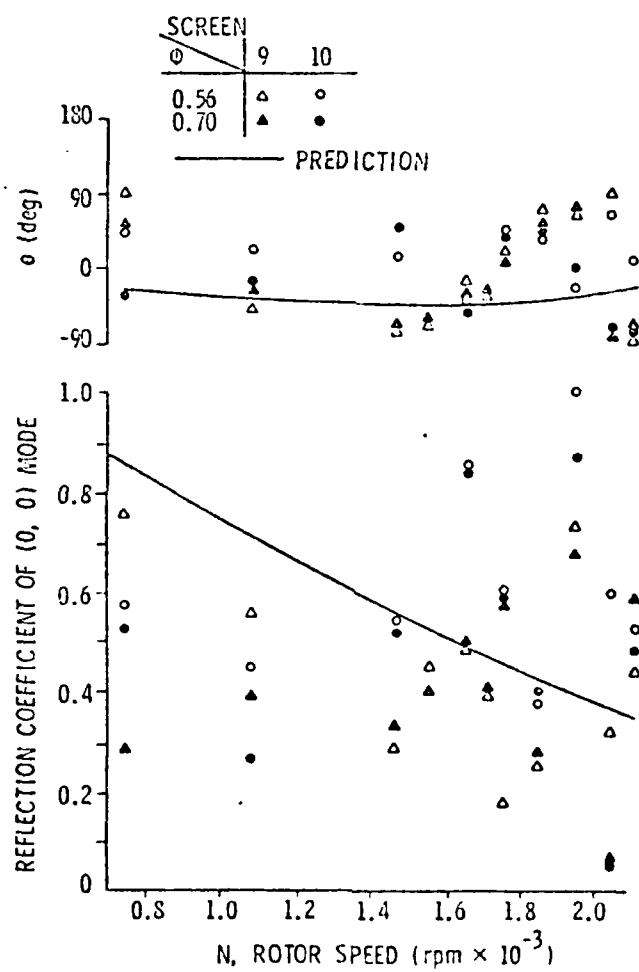


Figure 35 Reflection Coefficient of Duct Opening

It is difficult to explain the reasons for the discrepancy between the predictions of the acoustic pressure and the unsteady lift. Possibly, the reasons are that: (1) The measured SPL is a standing wave which results from the acoustic reflections, and varies from  $(1-R)$  to  $(1+R)$  times the source pressure depending on the measurement location. The large fluctuations of reflection coefficient in Figure 35 shows that a more detailed measurement of the acoustic field in the duct is necessary to get a reliable decomposed modal pressure at the source. (2) The effect of the boundary layer and the tip clearance might not be negligible in calculating the overall SPL at BPF. The local velocity is much smaller than the mean axial velocity in the boundary layer near the tip and hub of the rotor, consequently, the unsteady lift would be lower because the lift is proportional to the square of local axial velocity. The contribution to unsteady lift near the tip is important, since the linear circumferential velocity is a maximum at that point. Therefore, the effect of tip clearance and the velocity discrepancy might have a strong influence when predicting the overall SPL in the duct. For example, the percentage of the total acoustic pressure that is associated with the outer one inch of the blade span is 67%. This is roughly a factor of -3.5 dB. This would reduce the predicted SPL by this same amount and improve the agreement between all the predictions and measurements for the plane wave case. However, for the spinning mode case, the measured acoustic values are distinctly greater than the predicted values. Furthermore, the measured and predicted phase angle is also in distinct disagreement. Again, because the decomposed mode pressure depends upon the reflection coefficients and the theoretically assumed distribution of the mode pressure in the

duct, the possibility of error exists. Acoustic measurements at more locations along the duct would resolve the question of whether the acoustic behavior is as predicted in Appendix F or whether there is an error in the assumptions of the analysis used to predict the acoustic modal pressure from the unsteady lift values. Because there is observed a strong back-reaction of the acoustic pressure on the unsteady lift values, it is quite possible that some modification to the theory will be necessary.

CHAPTER IV  
CONCLUSIONS AND RECOMMENDATIONS

4.1 Conclusions

The following conclusions are drawn from this experimental investigation:

1. In the comprehensive experiment described, velocity perturbations, fluctuating blade lift, and overall noise levels were measured in order to produce a better understanding of the basic fan noise mechanism. By using distortion screens, a plane wave and a spinning wave were excited as designed. There was sufficient signal-to-noise ratio for the unsteady lift and acoustic pressure measurements; thus, it was confirmed that the AFRF is a suitable facility for studying acoustic duct modes.
2. Distortion screens to produce  $\pm 20$  percent sinusoidal velocity profiles were designed, built, and tested. Good agreement was achieved between design and measurement.
3. The lift gage in the instrumented rotor blade was calibrated as described in Appendix G, and its resonance frequency was found to be above the frequency range of interest in this study. The electrical noise from the slip ring was insignificant compared with the unsteady lift signals.

4. Using a phase-locked ensemble averaging technique, the amplitude and phase angle of the unsteady lift and acoustic pressure were measured with good repeatability.
5. A cutoff phenomenon was observed for the  $(-1,0)$  mode. Most of all, a significant back-reaction was observed near cutoff on the aerodynamic lift for both the plane wave and  $(-1,0)$  mode excitation, which had been suggested by Doak [23] and for which no experimental confirmation has been reported.
6. A noise prediction program and a modal decomposition program were written which gave a reasonable trend for the amplitude of the decomposed modes. However, the agreement with the theoretical prediction was poor. The discrepancies are believed to have resulted from the reflection model used in this study not being sufficiently refined to describe the resulting acoustic standing wave.
7. The Whitehead-Smith and Henderson-Shen theories were successful in predicting the unsteady lift on the blade at midspan for the ten-cycle screen. However, both models did not provide a satisfactory prediction for the case of "aerodynamic resonance" when the nine-cycle screen was installed.
8. The modal coupling scheme used in the prediction of SPL is direct, i.e., there is no amplification in amplitude and phase shift from unsteady aerodynamic lift to acoustic modal pressure. Since the result of modal pressure from the decomposition program is doubtful, the coupling coefficient in both magnitude and phase is still undetermined.

#### 4.2 Recommendations

The recommendations for future work are:

1. A fuller knowledge of the effect of acoustic reflection is necessary to decompose the measured acoustic pressures and to couple the unsteady lift to acoustic duct modes. By using a larger number of duct positions (both axially and circumferentially) to measure the amplitude and phase of sound pressure, the modal structure [21, 34], the reflection coefficient, and the distance between successive peaks [6, 11] can easily be obtained with greater accuracy.
2. A detailed measurement of unsteady pressures on the rotor blade by using miniature pressure transducers on both the pressure and suction sides should provide more information on the back-reaction of the acoustic pressure on the aerodynamic field.
3. This investigation used a ten-cycle screen which produced a  $(-1,0)$  rotating mode. An eight-cycle screen should be similarly tested as it will produce a  $(+1,0)$  mode. The difference in direction of mode rotation will change the reflection coefficient of the rotor and may provide some additional insight of the back-reaction behavior near cutoff.
4. An experimental study of the cutoff behavior and back-reaction of higher order modes other than  $(1,0)$  mode is desirable. By increasing the number of rotor blades and stagger angle, it would be possible to reach the cutoff frequencies of these higher order modes and still maintain a nominal zero incidence condition within the capacity of the AFRF.



5. To confirm the validity of the theoretical prediction of unsteady lift coefficient other than the "aerodynamic resonance" condition, a wider range of reduced frequencies should be tested. This can be obtained by changing the stagger angle and the distortion screens. For a detailed check of the validity of the lift theories near aerodynamic resonance, it is also necessary to select a wider range of blade numbers with the same number of cycles in the distortion screen to measure the unsteady lift response.
6. To confirm that the hydrodynamic field does indeed decay to a sufficiently low level at the microphone measurement locations, more measurements close to the rotor are needed.
7. A theoretical model which can describe the characteristics of the back-reaction of the acoustic field on the aerodynamic field should be developed.

AD-A095 080

PENNSYLVANIA STATE UNIV UNIVERSITY PARK APPLIED RESE--ETC F/6 21/5  
COUPLING OF UNSTEADY LIFT TO ACOUSTIC DUCT MODES IN AN AXIAL FL--ETC(U)  
SEP 80 C S LEE  
N00024-79-C-6043  
ARL/PSU/TM-80-188 NL

UNCLASSIFIED

2 OF 2  
AD-A095080




END  
DATE  
FILMED  
DTIC

## REFERENCES

1. Kemp, N. H., and Sears, W. R., "The Unsteady Forces Due to Viscous Wakes in Turbomachines," Journal of the Aeronautical Sciences, Vol. 5, No. 10, pp. 379-390, August 1938.
2. Horlock, J. H., "Fluctuating Lift Forces on Airfoils Moving through Transverse and Chordwise Gusts," Journal of Basic Engineering, ASME Transactions, Vol. 90D, No. 4, pp. 494-550, 1968.
3. Whitehead, D. S., "Force and Moment Coefficient for Vibrating Aerofoils in Cascade," Aeronautical Research Council R and M 3254, February 1960.
4. Whitehead, D. S., "Bending Flutter of Unstalled Cascade Blades at Finite Deflection," Aeronautical Research Council R and M 3396, October 1962.
5. Henderson, R. E., and Daneshyar, H., "Theoretical Analysis of the Fluctuating Lift on the Rotor of an Axial Turbomachine," Aeronautical Research Council R and M 3684, 1972.
6. Smith, S. N., "Discrete Frequency Sound Generation in Axial Flow Turbomachines," Aeronautical Council R and M 3709, 1973.
7. Kaji, S., and Okazaki, T., "Generation of Sound by Rotor-Stator Interaction," Journal of Sound and Vibration, Vol. 13, No. 3, pp. 281-307, 1970.
8. Mani, R., "Discrete Frequency Noise Generation from an Axial Flow Fan Blade Row," Journal of Basic Engineering, ASME Transactions, Vol. 92D, pp. 37-43, March 1970.
9. Osborne, C., "Unsteady Thin Airfoil Theory for Subsonic Flow," AIAA Journal, Vol. 11, No. 2, pp. 205-209, February 1973.
10. Tyler, J. M., and Sofrin, T. G., "Axial Flow Compressor Noise Studies," SAE Transactions, Vol. 70, pp. 309-332, 1962.
11. Morfey, C. L., "Rotating Pressure Patterns in Ducts: Their Generation and Transmission," Journal of Sound and Vibration, Vol. 1, pp. 60-87, 1964.
12. Bruce, E., P., "Axial Flow Rotor Unsteady Performance," Ph.D. Thesis, Aerospace Engineering, The Pennsylvania State University, 1979.

13. Satyanarayana, B., Henderson, R. E., and Gostelow, J. P., "A Comparison Between Experimental and Theoretical Fluctuating Lift on Cascades at Low Frequency Parameters," ASME Gas Turbine Conference, Zurich, Switzerland, Paper 74-GT-78, 1974.
14. Gallus, H. E., Lambertz, J., and Wallmann, T., "Blade-Row Interaction in an Axial Flow Subsonic Compressor Stage," ASME Gas Turbine Conference, San Diego, California, Paper No. 79-GT-92, 1979.
15. Sharland, I. J., "Sounds of Noise in Axial Flow Fans," Journal of Sound and Vibration, Vol. 1, pp. 302-322, 1964.
16. Bragg, S. L., and Bridge, R., "Noise from Turbojet Compressors," Journal of The Royal Aeronautical Society, Vol. 68, pp. 1-10, 1964.
17. Lowson, M. V., "Theoretical Studies of Compressor Noise," NASA-CR-1287, 1969.
18. Benzakein, M. J., "Research on Fan Noise Generation," Journal of the Aeronautical Society of America, Vol. 51, pp. 1427-1438, 1972.
19. Mani, R., and Lipstein, N. J., "Experimental Investigation of Discrete Frequency Noise Generated by Unsteady Blade Forces," Journal of Basic Engineering, ASME Transactions, pp. 155-164, 1970.
20. Harel, P., and Perulli, M., "Measurement in a Duct of the Space Structure of the Discrete Frequency Noise Generated by an Axial Compressor," Journal of Sound and Vibration, Vol. 23, No. 4, pp. 487-526, 1972.
21. Moore, C. J., "Measurement of Radial and Circumferential Modes in Annular and Circular Fan Ducts," Journal of Sound and Vibration, Vol. 62, No. 2, pp. 235-256, 1979.
22. Yardley, P., "The Application of Time-Domain Averaging Techniques to Fan Noise Measurement," Ph.D. Thesis, University of Southampton, 1973.
23. Doak, P. E., "Some Comments on Possible Back-Reaction Effect of Acoustic Fields on Aerodynamic Sound Sources," Basic Aerodynamic Noise Research, NASA-SP-207, 1969.
24. Archibald, F. S., "Self-Excitation of an Acoustic Resonance by Vortex Shedding," Journal of Sound and Vibration, Vol. 38, No. 1, pp. 81-103, 1975.
25. Archibald, F. S., "The Laminar Boundary Instability Excitation of an Acoustic Resonance," Journal of Sound and Vibration, Vol. 38, No. 3, pp. 387-402, 1975.
26. Crow, S. C., and Champagne, F. H., "Orderly Structure in Jet Turbulence," Journal of Fluid Mechanics, Vol. 48, pp. 547-591, 1971.

27. Morphey, C. L., "Rotating Blades and Aerodynamic Sound," Journal of Sound and Vibration, Vol. 28, pp. 587-617, 1973.
28. Cumpstey, N. A., "REVIEW--A Critical Review of Turbomachinery Noise," ASME Journal of Fluids Engineering, pp. 278-293, 1977.
29. Bruce, E. P., "The ARL Axial Flow Research Fan - A New Facility for Investigation of Time-Dependent Turbomachinery Flows," ASME Joint Fluids & CSME Conference, Montreal, Quebec, Canada, Paper No. 74-FE-27, 1974.
30. Treaster, A. L., and Yocum, A. M., "The Calibration and Application of Five-Hole Probes," ISA Transactions, Vol. 18, No. 3, pp. 23-34, 1979.
31. Doak, P. E., "Excitation, Transmission and Radiation of Sound from Source Distribution in Hard-Walled Ducts of Finite Length (I): The Effects of Duct Cross-Section Geometry and Source Distribution Space-Time Pattern," Journal of Sound and Vibration, Vol. 31, pp. 1-72, 1973.
32. Doak, P. E., "Excitation, Transmission and Radiation of Sound from Source Distribution in Hard-Walled Ducts of Finite Length (II): The Effects of Duct Length," Journal of Sound and Vibration, Vol. 31, pp. 137-175, 1973.
33. Shen, I. C., "Unsteady Pressure Distributions on Airfoils in Cascade," M.S. Thesis, Mechanical Engineering, The Pennsylvania State University, 1980.
34. Shapiro, A. H., The Dynamics and Thermodynamics of Compressible Fluid Flow, Vol. I, New York: The Ronald Press Co., 1953.
35. Moore, C. J., "In-duct Investigation of Subsonic Fan 'Rotor Alone' Noise," Journal of the Acoustical Society of America, Vol. 51, pp. 1471-1482, 1972.
36. Liebliien, S., "Experimental Flow in Two-Dimensional Cascades," NASA-SP-36, Chapter VI, "Aerodynamic Design of Axial Flow Compressors," pp. 183-226, 1965.
37. Howell, A. R., "The Present Basis of Axial Flow Compressor Design: Part I - Cascade Theory and Performance," Aeronautical Research Council R and M 2095, 1942.
38. McCarthy, J. H., "Steady Flow Past Non-Uniform Wire Grids," Journal of Fluid Mechanics, Vol. 19, pp. 491-512, 1964.
39. Bruce, E. P., "Design and Evaluation of Screens to Produce Multi-Cycle  $\pm 20\%$  Amplitude Sinusoidal Velocity Profiles," AIAA 8th Aerodynamic Testing Conference, Bethesda, Maryland, Paper No. 74-623, 1974.

40. Lighthill, M. J., "On Sound Generated Aerodynamically. I. General Theory," Proceedings of the Royal Society, Series A, Vol. 211, pp. 564-587, 1952.
41. Kinsler, L. E., and Frey, A. R., Fundamental Acoustics, Second Edition, New York: Wiley, Inc., 1960.
42. Aimet, R. K., "Transmission and Reflection of Sound by a Blade Row," AIAA 9th Aerospace Sciences Meeting, New York, New York, Paper No. 71-181, 1971.

## APPENDIX A

### DESIGN OF THE ROTOR

The steady state design of the AFRF 6-inch chord rotor was conducted by using Lieblien's [36] correlations, which are based on a minimum loss condition. At this condition, the actual total pressure ratio across the stage is maximized. The rotor blade shapes were specified as having a circular-arc camberline with a 10 percent maximum thickness-to-chord ratio.

The approach used was to apply a correction for spanwise effects to a mean radius design. The mean radius design consists of four aspects: (1) velocity diagram, (2) number of rotor blades, (3) the blade geometry (camber and stagger angle), and (4) the stall limit.

#### A.1 Mean Radius Design

##### A.1.1 Velocity Diagram

The velocity triangle at the rotor inlet is constructed using the axial velocity  $V_x$  calculated from the continuity equation for the design mass flow rate, and the blade rotational velocity  $U$ , determined from the design shaft speed. The change of the absolute circumferential velocity can be calculated from Euler's pump equation for a specified energy input from the drive motor at the design condition; this permits construction of the velocity triangle at the rotor outlet.

### A.1.2 Number of Rotor Blades

Howell [37] correlated the space-to-chord ratio,  $S/C$ , and fluid angle at "nominal deflection" (80 percent of the deflection angle at which the blades start to stall) as:

$$\frac{S}{C} = \left( \frac{1.55}{\tan \beta_i - \tan \beta_e} - 1.0 \right) \times \frac{1}{1.5} \quad , \quad (A1)$$

where  $\beta_i$  and  $\beta_e$  are the fluid angles relative to the rotor at inlet and outlet, respectively, that have been determined from the velocity triangle. Since  $B = 2\pi r_m / S$  is not an integer,  $B$  was taken as the closest integer.

### A.1.3 Blade Geometry

The camber angle correlated by Liebliien [36] can be expressed as:

$$\theta = \frac{(\beta_i - \beta_e) - K_{SH} \bar{K}_j [(i_o)_{10} - (\delta_o)_{10}]}{1 - m + n} \quad , \quad (A2)$$

where  $m, n$  are correlation constants, and  $K_{SH}$  and  $\bar{K}_j$  are shape correction factors. The incident angle  $i$  and deviation angle  $\delta$  can be obtained from

$$i = i_o + n\sigma \quad \text{and} \quad \delta = \delta_o + m\sigma \quad , \quad (A3)$$

where  $i_o$ ,  $\delta_o$ ,  $m$ , and  $n$  are plotted as correlation curves. By definition, the blade angles  $\beta'_i$  and  $\beta'_e$  are:

$$\beta'_i = \beta_i - i \quad \text{and} \quad \beta'_e = \beta_e - \delta \quad , \quad (A4)$$



and the stagger angle is:

$$\xi = \frac{\beta_i' + \beta_e'}{2} \quad . \quad (A4)$$

#### A.1.4 Stall Limit

Liebliien defined the diffusion factor, D, as

$$D = 1 - \left( \frac{\cos \beta_i}{\cos \beta_e} \right) + \left( \frac{S}{C} \right) \frac{\cos \beta_i}{2} [\tan \beta_i - \tan \beta_e] \quad . \quad (A5)$$

For an unstalled condition, it is required that  $D < 0.6$ .

#### A.2 Spanwise Variation

The hub-tip radius ratio for the AFRF is 0.442, which is lower than the limit, 0.7, for a two-dimensional approach, so the radial variation of flow also should be considered. To avoid swirl in the flow, a free-vortex design was employed, i.e.:

$$V_{r_i} r = V_{r_i} r_m = 0 \quad \text{at rotor inlet}$$

and

$$V_{r_e} r = V_{r_e} r_m = \text{const.} \quad \text{at rotor exit} \quad .$$

The fluid angles at different radii can be calculated from

$$\beta_i = \tan^{-1} (r\omega/V_x) \quad ,$$

$$\beta_e = \tan^{-1} [(r\omega - V_{r_e})/V_x]$$

and

$$\alpha_e = \tan^{-1} (V_{r_e}/V_x) \quad (A6)$$

Finally, the blade angle at each radius can be determined in the same way as the midspan analysis, and unstalled conditions checked at each radius.

## APPENDIX B

### SELECTION OF MICROPHONE LOCATIONS

The objective of the microphone measurement is to decompose the measured acoustic pressure into duct modal components and to confirm that the generated pattern is the (0,0) or (-1,0) mode as designed.

The reflection effect of rotor and duct inlet opening was checked by the reflection program described in Appendix F, and it was found that a steady state pressure distribution is calculated after the first reflection by the duct inlet opening for the (0,0) and (-1,0) modes for all conditions including the more critical condition near cutoff in the AFRF as shown in Figure F2. Thus, only the first reflection is considered in the reverse problem of acoustic decomposition.

To determine the number of microphone measurement positions needed for modal decomposition, consider two cases: (i) the cutoff ratio is greater than unity, and the (-1,0) mode will propagate, so there are four unknowns:  $p_0$ ,  $p_1$  [complex pressure for (0,0) and (-1,0) modes], and  $R_0$  and  $R_1$  [complex reflection coefficients of the inlet opening for either mode]. Therefore, at least four measurement points are needed to decompose the modal pressure  $p_0$ ,  $p_1$  and compare  $\bar{R}_0$ ,  $\bar{R}_1$  with the theoretical prediction. In case (ii), the cutoff ratio  $\gamma < 1$ , only the plane wave propagates, so  $p_1$  and  $R_1$  are eliminated and only two measurement points are needed.

To discriminate between the various modes, the microphone axial location should be optimized. This is accomplished by locating the microphone where the desired mode has a higher pressure magnitude relative to all other modal components. In the test program, only (0,0) and (-1,0) modes are of interest. The plots of  $|p_0| - |p_1|$  versus axial position were run for some test cases. The optimized measurement location for the plane wave is where the quantity  $(|p_0| - |p_1|)$  is a maximum, and for the (-1,0) mode, where the quantity  $|p_0| - |p_1|$  is a minimum. However, the standing wave pattern is a function of frequency, i.e., the optimized locations vary with  $\gamma$ , so the four locations were selected for each mode near the optimized positions over the cutoff frequency ratios used in the test. Microphone locations close to the rotor, which are in the near field ( $\leq 1.0$  ft) were avoided to ensure that the near-field hydrodynamic pressure had decayed sufficiently so that it did not contribute to the acoustic measurement.

At the same axial location, different circumferential locations introduce a phase shift in the pressure measurement for the higher order spinning mode when  $\gamma > 1$ . There is no circumferential phase dependence for the plane wave. Consequently, the four selected axial locations were staggered circumferentially to distinguish one mode from the other by examining the phase difference between each measurement location.

APPENDIX C  
DESIGN OF DISTORTION SCREENS

Tyler and Sofrin [10] indicated that the circumferential order of an acoustic mode generated by rotor-stator interaction can be expressed as:

$$m = nB + kV \quad , \quad (C1)$$

where

B = number of rotor blades,

V = number of stator blades or distortions at rotor inlet flow,

n = BPF harmonics

and

k = ... -1, 0, 1 ... arbitrary integer.

For the nine-bladed rotor in the AFRF, this equation shows that the plane wave (0,0) mode and the first higher order (-1,0) mode can be generated by a nine- and a ten-cycle distortion, respectively.

Nine- and ten-cycle distortion screens were employed in the experiment. The screens were designed to produce sinusoidal velocity profiles with  $\pm 20$  percent variation in the mean axial velocity  $\bar{V}_x$ . Sinusoidal velocity distortions are desired because the aero-acoustic analysis is linear. Consequently, knowing the behavior for a pure sine wave permits prediction for more complicated waveforms using superposition. A distortion magnitude of 20 percent was selected as it is a significant distortion, but still small enough to apply linearized theories in predicting the response of the rotor.

For the rotor inlet flow, the spatially-fixed axial velocity  $V_x$  can be decomposed into a Fourier series as:

$$\frac{V_x}{\bar{V}_x} = \frac{A_0}{2} + \sum_{n=1}^{\infty} A_n e^{i(n\theta + \phi_n)} \quad (C2)$$

The desired velocity profile should be dominated by either the ninth or the tenth harmonic in the experiment.

On passing through a screen, the total pressure of the flow is reduced. This pressure drop  $\Delta P$  can be described by a dimensionless resistance coefficient  $K$ , which is based on the local velocity  $V_o$  normal to the screen:

$$K = \frac{\Delta P}{\frac{1}{2} \rho V_o^2} \quad (C3)$$

McCarthy [38] developed an analytical solution for a steady moderately sheared three-dimensional flow past wire screens. The solution expressed the velocity downstream of the screen as a function of flow resistance,  $K$ . Substituting the equation into the Fourier series leads to the expression

$$A_f \sin n\theta = \frac{1.02(1+X)}{(1+X^3)^{2/3}} \left( \gamma_o - \frac{1+6X^3}{6X^2} \right) \quad (C4)$$

where

$$X = (1+K)^{1/2},$$

$$X_o = (1+K_{\min})^{1/2}$$

and

$$\gamma_o = \frac{1+6X_o^3}{6X_o^2} + \frac{A_f(1+X_o^3)}{1.02(1+X_o)}.$$

The resistance coefficients of the support screens  $K_{\min}$  are 0.343 and 0.236 for the nine- and the ten-cycle screens, respectively. Setting the magnitude of the fundamental harmonic  $A_f = 0.2$ , the solution of this equation gives the desired variation of  $K$  with  $\theta$  as shown in Figures C1 and C2.

Various segments of screens with different resistance coefficients were overlaid to obtain an approximation of the calculated resistance variation. The approximation was determined by equally dividing the difference in area between the step changes in resistance and the desired variation. Ideally, the more step changes used in the  $K$  distribution, the better will be the approximation to a sinusoidal velocity distribution. However, due to the limitation of the available screen stock and the difficulty in cutting large spacing screens into small segments, only three- and one-step changes of  $K$  were chosen in the design of the screens. A more detailed design procedure was presented by Bruce [39].

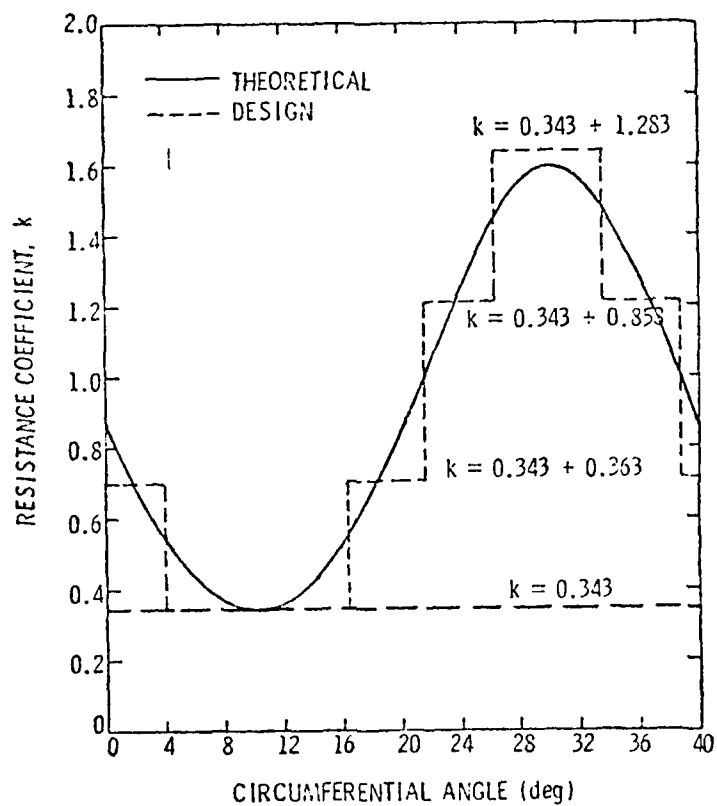


Figure C1 Theoretical and Designed Variation of Resistance Coefficient for Nine-Cycle Screen



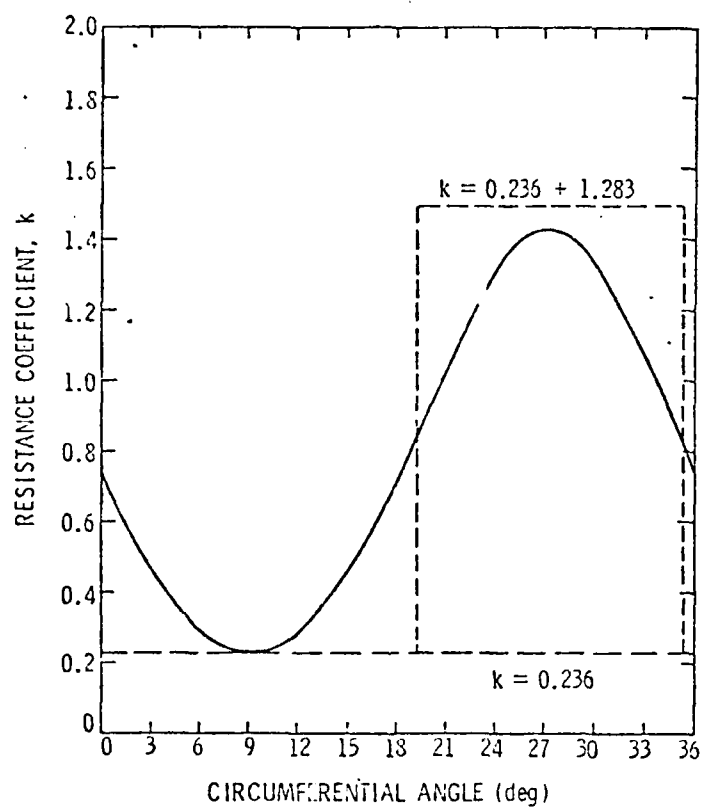


Figure C2 Theoretical and Designed Variation of Resistance Coefficient for Ten-Cycle Screen

## APPENDIX D

### SIGNAL PROCESSING CONSIDERATIONS

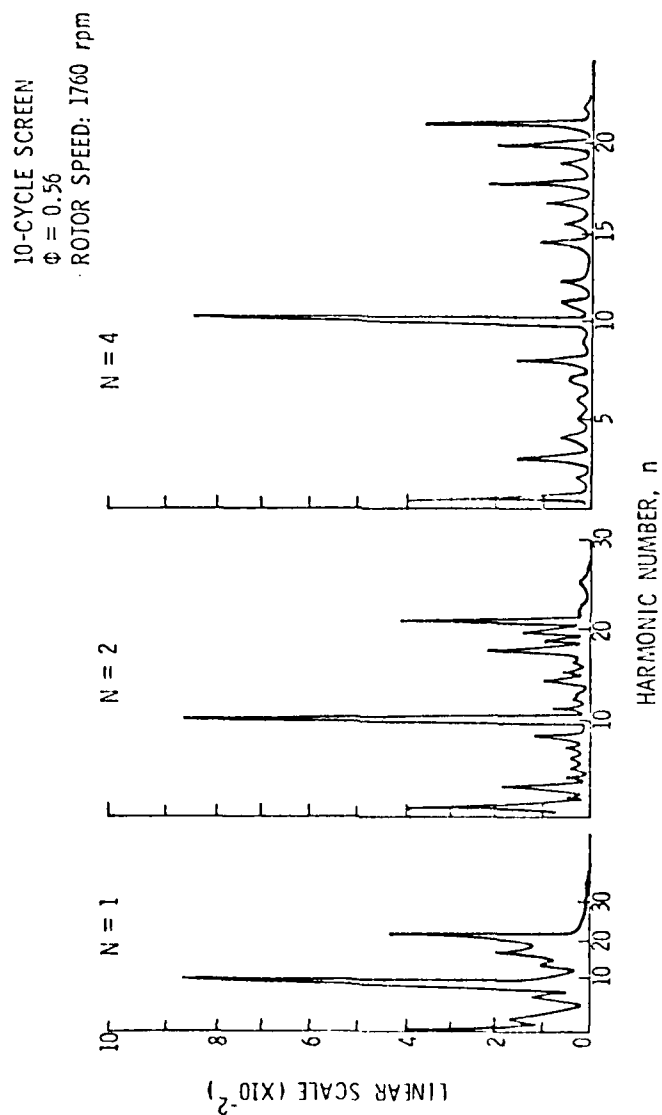
The frequency range selected on the analyzer was 500 Hz, since the value of the BPF over the test range was less than 310 Hz for all test conditions. The sampling period at this frequency range setting was 100 msec, which was a "time duration window" long enough to cover the lowest rotor speed condition, i.e., 742 rpm or 1.35 msec/rev.

The aliasing filter was disconnected in the phase-locked average tests, since a phase shift would be introduced by the filter as a function of input frequency that was undesirable. Because the aliasing frequencies were higher than 400 Hz, which is beyond the frequency range of interest for the test, no error was introduced from aliasing of the spectral analyses.

The frame size of the signal processor is 1024 for the calculation of the spectrum by the FFT in function 13. These data points were triggered by the tracking ratio tuner with a sampling frequency of  $1024/N$  times the rotor speed, where  $N$  is an integer. When  $N = 1$ , the magnitude and the phase are transformed by the averaged waveform experienced by the instrumented rotor blade in one revolution. As  $N$  increases, the sampling rate decreases and the averaged waveform shrinks in the time domain; thus, the transformed harmonics of the shaft speed will expand along the frequency axis, giving a better resolution to distinguish the fundamental harmonic and the neighboring ones. However, although there are  $N$  more revolutions in the 1024 display than when  $N = 1$ , the accuracy

is decreased since there are fewer sampling points per revolution. Figure D1 shows the effect of changes in  $N$  in the transformed plane of the unsteady lift measurement. The value  $N = 4$  was taken for the lift gage measurements to obtain better resolution when recording the data.

Note that, although better resolution of the harmonic of interest is obtained, the level of the harmonic is not affected by the  $N$  setting. Since the acoustic pressures were dominated by a pure tone at BPF, resolution was not important to separate the harmonics; thus,  $N = 1$  was taken in the acoustic measurement.

Figure D1 Effect of Tracking Ratio Tuner Divider  $N$  on Spectrum Resolution

APPENDIX E

COMPARISON OF NOISE PREDICTION SCHEME AND EXACT SOLUTION TO  
SOUND GENERATION EQUATION

Lighthill [40] first derived a general linearized equation for sound generation as:

$$\frac{\partial^2 \rho'}{\partial t^2} - c^2 \frac{\partial^2 \rho'}{\partial x_i^2} = \frac{\partial Q}{\partial t} + \frac{\partial F_i}{\partial x_i} + \frac{\partial^2 T_{ij}}{\partial x_i \partial x_j} \quad (E1)$$

The left-hand side of the equation is the wave equation, and the right-hand side can be regarded as a collection of acoustic source terms, where  $Q$ , the first term on the right-hand side, is the rate of introduction of mass per unit volume and represents the sound generated by the volume displacement effects of the blades, analogous to an acoustic monopole.  $F_i$  is the external force per unit volume acting on the fluid; thus, the second term can be interpreted as a dipole source from the fluctuating forces exerted on the rotor.  $T_{ij}$  is the stress tensor consisting of Reynolds stress and fluid pressures. The last term represents a quadrupole source arising from turbulence in the flow field.

In the generation of fan noise at low Mach number, the significant source term is the fluctuating force  $F_i$ . By putting  $p = c^2 \rho'$ , the equation can be easily converted to pressure, which is applied in its most practical form as:

$$\frac{\partial^2 p}{\partial x_i^2} - \frac{1}{c^2} \frac{\partial^2 p}{\partial t^2} = \frac{\partial F_i}{\partial x_i} \quad (E2)$$

Mani [8] considered a temporal harmonic pressure wave and replaced the unsteady force on the cascade by a row of delta functions in cylindrical coordinates. The solution of Equation (E2) was found to be:

$$p = \sum_{mn} p_{mn} E_{mn}(r) \exp i[-\omega t \pm m\theta \pm k_{mn} x + \phi_{mn}] ,$$

where

$$p_{mn} = 2\pi \int_{r_a}^{r_b} \nabla F \cdot E_{mn}(r) r dr$$

$$\text{and} \quad \nabla F = [\cos(\xi) \cdot \delta'(x) + i \sin(\xi) \frac{m}{r} \delta(x)] . \quad (E3)$$

In the expressions of Lighthill and Mani,  $F$  is a force per unit volume. In the noise prediction program used in this thesis, the force is the lift force per unit span. In Mani's formulation, the spatial divergence of the force per unit volume was obtained, resolved in the direction of the wavefront, weighted by the radial distribution of mode pressure, and integrated over the duct. In the noise prediction scheme used in this thesis, the unsteady lift per unit span was resolved in the direction of the wavefront, integrated along the span and weighted by the radial mode shape, and divided by the duct area. Composing the dimensions of the quantities used in each prediction shows that the result is a unit of pressure.

Mani:

$$\left( \frac{F}{L^2} \right) \times \left( \frac{1}{L^2} \right) \times E_{mn} \times \left( L^2 \right) = \left( \frac{F}{L^2} \right)$$

Thesis:

$$\left( \frac{F}{L} \right) \times E_{mn} \times \left( L \right) \times \left( \frac{1}{L^2} \right) = \left( \frac{F}{L^2} \right)$$

Note the unsteady lift force is assumed to couple directly in magnitude with no temporal phase shift to the acoustic wavefront.

## APPENDIX F

### THE EFFECT OF REFLECTION AND ACOUSTIC MODE DECOMPOSITION

The discontinuity of the duct at the inlet opening and the rotor blade causes sound waves to be reflected between these two faces. The measured sound pressure at a fixed position is then the net effect of the incoming wave generated at the source and the reflected waves which travel back and forth between the duct opening and the rotor blade row.

The pressure pattern of higher order modes  $(m,0)$  can be written as:

$$\begin{aligned} \text{(i) below cutoff } p &= p_{mo}(r) e^{-kx} e^{i(\omega t - \theta)} , \\ \text{(ii) at cutoff } p &= p_{mo}(r) e^{i(\omega t - \theta)} , \\ \text{(iii) above cutoff } p &= p_{mo}(r) e^{i(\omega t - akx - \theta)} . \end{aligned} \quad (F1)$$

Examining these expressions, when the frequency is below or at cutoff, the wave front is in the  $\theta$  direction, which is parallel to the duct opening, so there will be reflection in these cases. For the plane wave which always travels axially and spinning higher order modes above their cutoff frequencies which travel in a helix path, the effect of reflection must be considered.

#### F.1 Reflection of the Duct Opening

Consider an oblique incident wave with helix angle  $\alpha$ , it can be written as:

$$p_i = p_i e^{j(\omega t - k\bar{d})} , \quad (F2)$$



where  $\bar{d}$  is the wave front vector,  $\bar{d} = x \cos \alpha + y \sin \alpha$ , and  $P_i$  is the complex amplitude of the incident wave.

The angle of incidence must be equal to the angle of reflection, so the reflected wave is written as:

$$P_r = P_i e^{j(\omega t - k\bar{d}')} ,$$

where  $\bar{d}'$  is the reflected wave front vector,  $\bar{d}' = -x \cos \alpha + y \sin \alpha$ .

Morfev [11] considered a flanged annular duct opening and obtained an expression for the impedance of the  $(m,0)$  modes for the case where the annulus width is small compared with the wave length. This expression for the modal resistance  $\tau$  and reactance  $\chi$  is:

$$\tau = \mu v \bar{J}_{2m}(2\mu v) - \frac{\mu v}{\pi} [S_i \mu(1+v) - S_i \mu(1-v)] + \frac{2}{\pi} \mu v^2 \sin \mu$$

and

$$\begin{aligned} \chi = \mu v \bar{\Omega}_{2m}(2\mu v) + \frac{2\mu v}{\pi} \int_{h/4_0}^{\pi/2} \frac{\cos 2m\psi}{\sin \psi} d\psi + \frac{2v}{\pi} (\ln 2 \cdot \sin \mu + S_i \mu) \\ + \frac{\mu v}{\pi} \left[ 2C_i \mu + 2n|1-v^2| - C_i \mu(1+v) - C_i \mu(1-v) \right] , \end{aligned}$$

(F3)

where

$$v = \frac{kr_0}{m}$$

and

$$\mu = \frac{mh}{2r_0} ,$$

with

$h$  = the annulus width,

$r_o$  = the root mean square of hub and tip radii  $r_o^2 = \frac{1}{2}(r_a^2 + r_b^2)$ ,

$\bar{J}_{2m}$  = integration of the Bessel function of first kind of order  $2m$ ,

$\bar{\Omega}_{2m}$  = integration of the Weber function of order  $2m$ ,

$S_i$  = Sine integral function,

$C_i$  = Cosine integral function

and

$\ln$  = natural logarithm function.

Then, the reflection coefficient can be calculated by Equation (8.29) of Reference [41]:

$$R = \frac{P_r}{P_i} = \frac{(\tau \cos \alpha - 1) - j(\chi \cos \alpha)}{(\tau \cos \alpha + 1) - j(\chi \cos \alpha)} \quad (F4)$$

## F.2 Reflection of the Rotor Blade Row

Aimet [42] considered an obliquely incident sound wave impinging on a stationary blade row and obtained the direction and amplitude of the reflected wave as:

$$R = \left| \frac{P_r}{P_i} \right| = \frac{M \sin \alpha (2\psi \sin \theta - H^2 \sin \alpha)}{(M \sin^2 \alpha + \ell \psi) H^2}$$

and

$$\phi = \tan^{-1} \frac{2\psi \sin \theta - H^2 \sin \alpha}{2\psi \cos \theta - H^2 \cos \alpha}, \quad (F5)$$

where  $\alpha$  and  $\phi$  are the angle of incidence and the angle of reflection, respectively, relative to the blade, and where

$M$  = Mach number,

$$\psi = \cos (\theta - \alpha) - M \cos \theta,$$

$$H^2 = 1 - M^2 \cos^2 \theta$$

and

$l$  = lattice coefficient.

Writing the incident wave as:

$$p'_i = P'_i e^{i(\omega t - k\bar{d})},$$

where  $\bar{d} = -x \cos (\alpha - \xi) + y \sin (\alpha - \xi)$  is the wave front vector,

then, the reflected wave should be:

$$p'_r = RP'_i e^{i(\omega t - k\bar{d}')},$$

where

$$\bar{d}' = x \cos (\phi + \xi) + y \sin (\phi - \xi),$$

and  $\xi$  is the blade stagger angle. The following summarizes the reflection considerations for two cases:

1. Reflection at the duct opening: (a) change the sign of x-component of the wave number, (b) attenuate the pressure amplitude by a factor  $|R|$ , and (c) shift the temporal phase angle by the phase angle of the complex quantity  $\bar{R}$ .
2. Reflection at the rotor blade row: (a) the angle of reflection is not equal to the angle of incidence, i.e., the helix angle changes after the reflection, (b) the pressure amplitude is attenuated by the factor  $R$ , and (c) there is no temporal phase shift.

For the case of the AFRF operating near the cutoff frequency, Aimet's expression for reflection coefficient at the rotor blade row ( $R_r$ ) is applicable because the wavelength is long (4 ft) compared with the blade spacing (0.45 ft), and rotor chord length (0.5 ft), i.e.,

the coordinate is only slowly varying with time. The restrictions set in Morfey's [11] calculation for the reflection coefficient at the duct opening ( $R_o$ ):  $kh < 1$ ,  $h < r_o$  can also be satisfied ( $r_o = 0.692$  ft,  $h = 0.50$  ft,  $k = 1.5 \text{ ft}^{-1}$ ).

A computer program was written to calculate the sound pressure after  $N$  times of reflection between the two faces at different measurement locations  $(x, \theta)$  near the duct wall for a known acoustic pressure source. Only the plane wave and the first higher order mode (1,0) were considered. The program reads in the modal source pressure  $p_o$  and  $p_1$ , which can be obtained from the program for the unsteady lift of a cascade. The impedance of the duct opening is a function of frequency, and  $R_o$  which is calculated by Equation (F4) varies with angle of incidence. In Equation (F5),  $R_r$  is a function of the incident angle relative to the blade row for a specific duct geometry. The amplitude and phase of the resultant pressure is then the complex summation of the incident and reflected waves.

Plots of the steady state pressure distribution versus duct axial length at different operating conditions are shown in Figures F1 and F2. It can be seen that, for the plane wave and (1,0) mode whose cutoff ratio is greater than 1.1,  $N = 1$  is enough to reach a steady state or a convergent solution. This is because the averaged reflection coefficients  $R_o$  and  $R_r$  are 0.9 and 0.1 respectively, so the effect of the second reflection only has a 9 percent contribution to the resultant magnitude at most. However, for the (1,0) mode slightly above cutoff,  $N = 3$  is required to reach convergence. This occurs because the second reflection at the blade row is not negligible for a

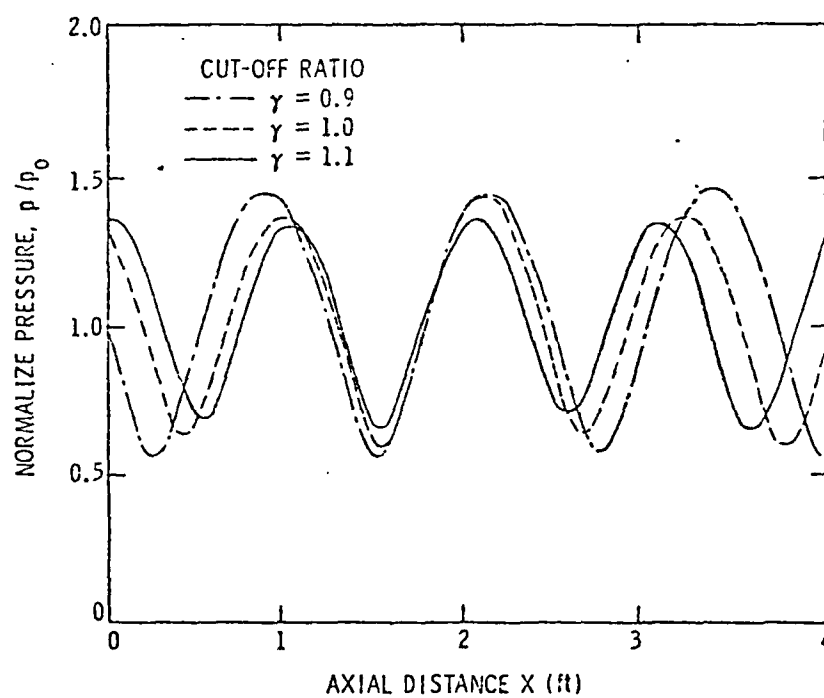


Figure F1 Steady State Wave Form After Reflections for Plane Wave

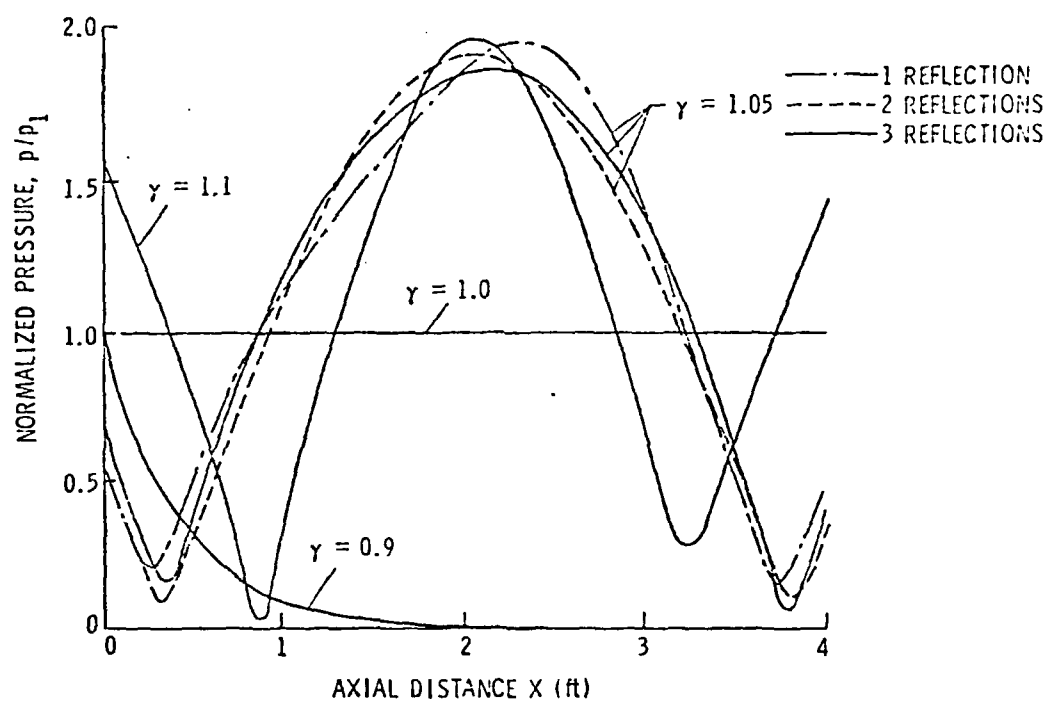


Figure F2 Steady State Wave Form After Reflections for (1,0) Mode

helix angle near 90 degrees, i.e., the incident angle is larger relative to the rotor blade row.  $R_r$  is a function of stagger angle, so it varies along the span. To examine this spanwise variation, the convergent pressure distribution was plotted against stagger angle at hub, midspan, and tip, and it was found that the greatest difference for the cases considered is 8.5 percent. A different spin direction relative to the spin direction of the rotor has a different incidence angle relative to the rotor blade row. The pressure distribution for the co-spin (8-cycle inlet distortion) and the counter-spin (10-cycle inlet distortion) has been compared. These two cases essentially result in the same standing wave, since  $R_r$  is very small compared with  $R_o$  so that, theoretically, spin direction does not have a strong influence.

### F.3 Modal Decomposition with Reflection

A data reduction program was written to calculate the source modal pressure  $p_o$  and  $p_1$  at the rotor blade row. It has been shown that, for all the cases except the  $(\pm 1, 0)$  mode, whose cutoff ratio is slightly greater than unity, one reflection is sufficient to reach a steady state solution for the experimental conditions. Thus, only the first reflection is considered.

The resultant measured pressure can be written as:

(i) below cutoff

$$p_m = p_o e^{-ikx} + R_o p_o e^{ikx} ,$$

(ii) at cutoff

$$p_m = p_o e^{-ikx} + p_1 e^{-i\theta} + R_o p_o e^{ikx} , \text{ and}$$

(iii) above cutoff

$$p_m = p_o e^{-ikx} + p_1 e^{i(-\alpha kx - \theta)} + R_o p_o e^{ikx} + R_1 p_1 e^{i(\alpha kx - \theta)}, \quad (F6)$$

where  $R_o$  and  $R_1$  are the complex reflection coefficients at the duct opening for the plane wave and  $(-1,0)$  mode, respectively.

The unknowns in case (i) are  $p_o$  and  $R_o$ , since the  $(-1,0)$  mode quickly decays. For case (ii), there are three unknowns  $p_o$ ,  $p_1$  and  $R_1$ , because there is no reflection of the  $(-1,0)$  mode whose cutoff ratio is smaller than 1.0, so only three measurement points are needed. For case (iii), there are four unknowns:  $p_o$ ,  $p_1$ ,  $R_o$ , and  $R_1$ , i.e., at least four measurement points are required to obtain a solution. The values of  $R_o$  and  $R_1$  obtained from the solution can be used as a check with the theoretically predicted reflection coefficients.



## APPENDIX G

### CALIBRATION OF UNSTEADY FORCE GAGE

As discussed in Section 2.4.2, the frequency response of the unsteady lift gage (judging by the broadband spectrum analysis) appeared to be flat over the frequency range of interest, with a resonance about 500 Hz. The result indicated that a static calibration of the lift gage could be employed over the flat portion of the frequency response. To confirm this flat response, a dynamic calibration of the blade segment was attempted with a small electro-dynamic shaker and a calibrated unsteady force gage. However, with these components attached to the blade segment, it was found that the resonance frequency was lowered to about 380 Hz.

The shaker and force gage were then detached from the blade and the voltage output was observed on an oscilloscope after tapping the blade with the end of a pencil. Measuring the distance between peaks in the decaying sine wave showed the resonant frequency to be approximately 500 Hz, which indicated that the shaker assembly was responsible for the difference. Another confirmation that the added mass lowered the resonant frequency of the system was the measurement of a resonant frequency of approximately 450 Hz when a 7 gram accelerometer was next attached to the blade and tapped as previously.

In order to avoid having any added mass on the instrumented blade segment, a seismic technique to measure the frequency response was employed. The blade was mounted on a large (50 lb<sub>rms</sub>) shaker with a 7 gram accelerometer on the rigid portion of the blade, as shown in Figure

G1. The input acceleration level was maintained constant for several frequencies over the range of interest. Since the acceleration level and the mass of the blade segment are constant, the force on the segment is also constant by Newton's second law.

A voltmeter was used to set the acceleration level that produced an output voltage from the lift gage typical of the values obtained during testing in the axial flow research fan. The frequency response for two other equivalent force levels were similarly evaluated to check linearity of the lift gage.

The results of this seismic calibration are shown in Figure G2 and indicate a flat response and linear behavior of the gage through the frequency range of interest. These results confirm that a static calibration of the lift gage can be employed and, in fact, for the very low mass blade segment employed, this is the most accurate technique to employ. The arrangement used in the static calibration is shown in Figure G3. Weights were applied in the direction of the lift force by a wire passing over a pulley mounted on a ball bearing. Simultaneously, weights were added to simulate the effect of the centrifugal force on the instrumented blade segment. Figure G4 shows the results of this calibration.

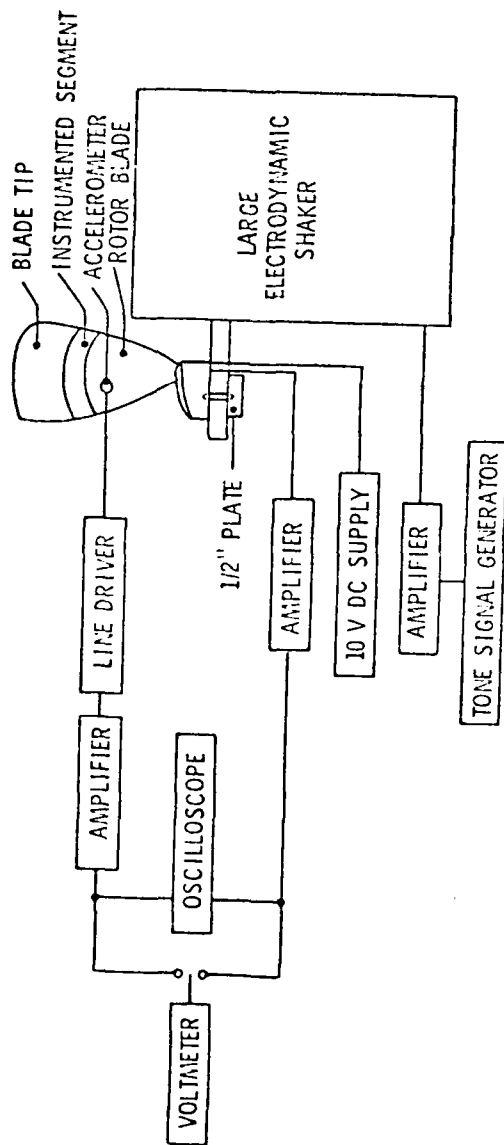


Figure C1 Instrumentation of Dynamic Calibration of Unsteady Force Cage

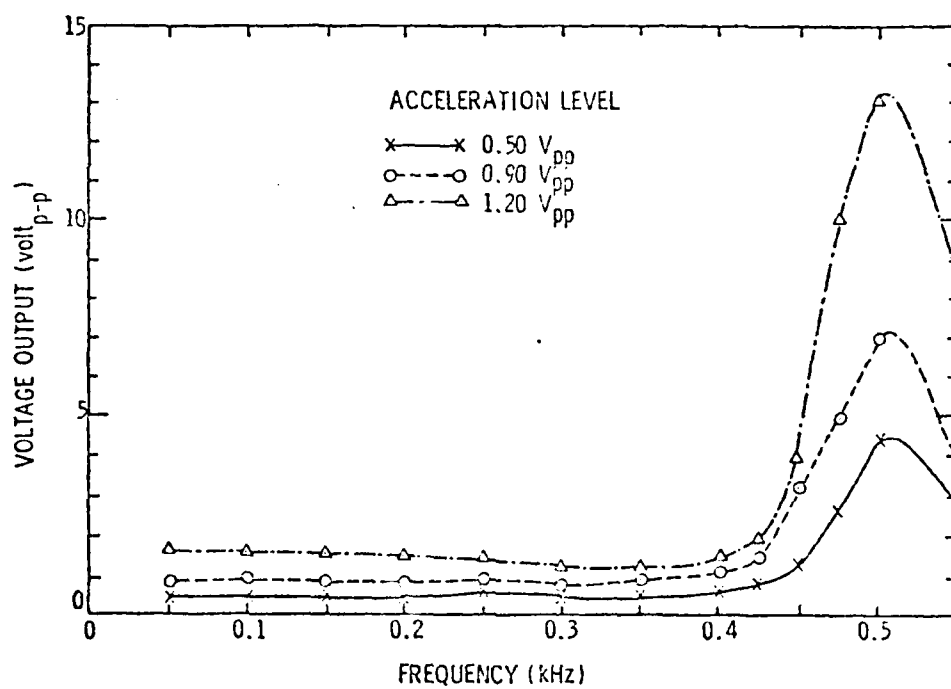


Figure G2 Dynamic Calibration of Unsteady Force Gage

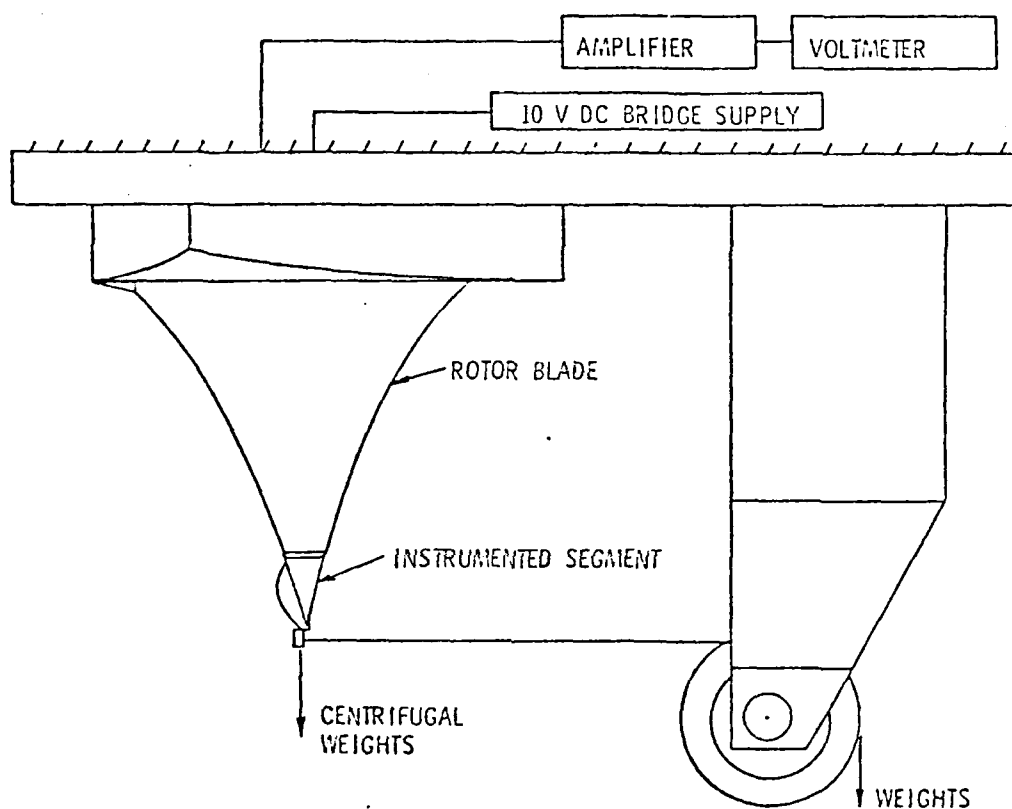


Figure G3 Instrumentation of Static Calibration of Unsteady Force Gage

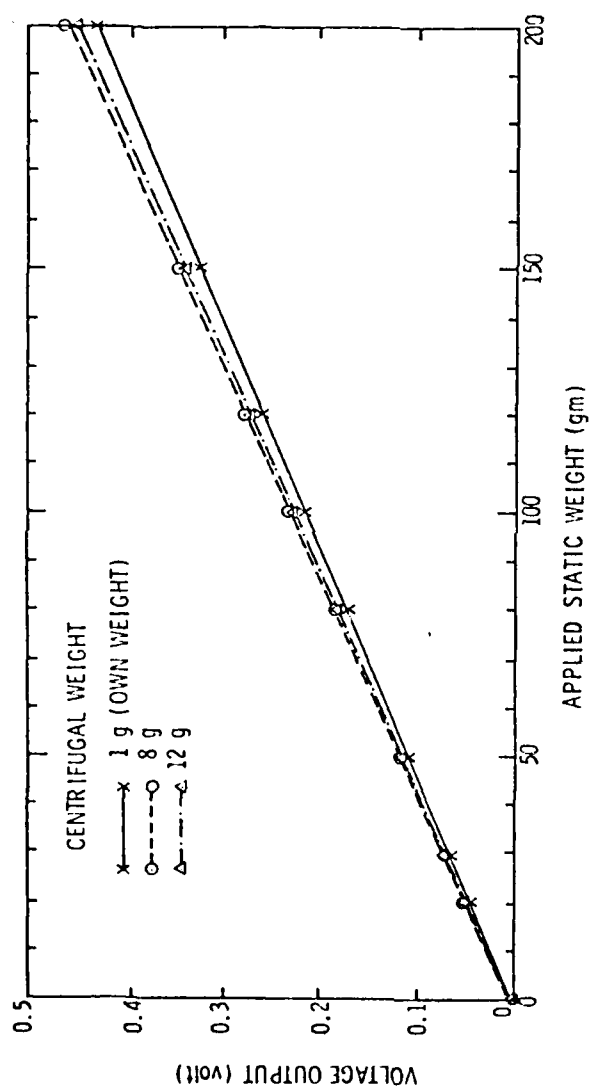


Figure G4 Static Response of Unsteady Force Gage

DISTRIBUTION LIST FOR ARL UNCLASSIFIED TM 80-188 by C. S. Lee dated  
September 15, 1980.

Commander  
Naval Sea Systems Command  
Department of the Navy  
Washington, DC 20362  
Attn: Library  
Code NSEA 09G32  
(Copy Nos. 1 and 2)

Naval Sea Systems Command  
Attn: Code NSEA 0342  
(Copy Nos. 3 and 4)

Naval Sea Systems Command  
Attn: T. E. Peirce  
Code NSEA 63R3  
(Copy No. 5)

Naval Sea Systems Command  
Attn: A. R. Paladino  
Code NSEA 05H1  
(Copy No. 6)

Naval Sea Systems Command  
Attn: F. Peterson  
Code NSEA 52P  
(Copy No. 7)

Defense Technical Information Center  
5010 Duke Street  
Cameron Station  
Alexandria, VA 22314  
(Copy Nos. 8 through 19)

Commanding Officer  
Naval Underwater Systems Center  
Newport, RI 02840  
Attn: Library  
Code 54  
(Copy No. 20)

Commanding Officer  
Naval Ocean Systems Center  
San Diego, CA 92152  
Attn: Library  
(Copy No. 21)

Commanding Officer & Director  
David W. Taylor Naval Ship R&D Center  
Department of the Navy  
Bethesda, MD 20084  
Attn: W. B. Morgan  
Code 15  
(Copy No. 22)

David W. Taylor Naval Ship R&D Center  
Attn: J. H. McCarthy  
Code 154  
(Copy No. 23)

David W. Taylor Naval Ship R&D Center  
Attn: M. Sevik  
Code 19  
(Copy No. 24)

David W. Taylor Naval Ship R&D Center  
Attn: J. Shen  
Code 195  
(Copy No. 25)

David W. Taylor Naval Ship R&D Center  
Attn: W. K. Blake  
Code 1942  
(Copy No. 26)

David W. Taylor Naval Ship R&D Center  
Attn: F. S. Archibald  
Code 1942  
(Copy No. 27)

Commanding Officer & Director  
David W. Taylor Naval Ship R&D Center  
Department of the Navy  
Annapolis Laboratory  
Annapolis, MD 21402  
Attn: J. G. Stricker  
Code 2721  
(Copy No. 28)

David W. Taylor Naval Ship R&D Center  
Attn: Y-F Wang  
Code 2740  
(Copy No. 29)

United Technologies Research Center  
400 Main Street  
East Hartford, CT 06108  
Attn: Mr. Franklin O. Carta  
(Copy No. 30)

Massachusetts Institute of Technology  
77 Massachusetts Avenue  
Cambridge, MA 02139  
Attn: Dr. E. M. Greitzer  
(Copy No. 31)

DISTRIBUTION LIST FOR ARL UNCLASSIFIED TM 80-188 by C. S. Lee dated  
September 15, 1980.

Stevens Institute of Technology  
Department of Mechanical Engineering  
Castle Point Station  
Hoboken, NJ 07030  
Attn: Professor F. Sisto  
(Copy No. 32)

ONERA  
Energie and Propulsion  
29 Avenue de la Division Leclure  
92 Chatillon sous Bagneux, FRANCE  
Attn: Mr. J. Fabri  
(Copy No. 33)

Virginia Polytechnic Institute and  
State University  
Mechanical Engineering Department  
Blacksburg, VA 24601  
Attn: Dr. Walter F. O'Brien, Jr.  
(Copy No. 34)

Purdue University  
School of Aeronautics and Astronautics  
Chaffee Hall  
West Lafayette, IN 47907  
Attn: Dr. S. Fleeter  
(Copy No. 35)

University of Salford  
Salford, M5 4WT  
ENGLAND  
Attn: Dr. John H. Horlock  
Vice Chancellor  
(Copy No. 36)

Netherlands Ship Model Basin  
P.O. Box 28  
6700 AA Wageningen  
THE NETHERLANDS  
Attn: Dr. P. van Oossanen  
(Copy No. 37)

Mut-Munchen GmbH  
8 Munchen 50  
Postfach 50 06 40  
GERMANY  
Attn: Dr. Hans Mokelke  
(Copy No. 38)

Forschungsbeauftragter für Hydroakustik  
8012 Ottobrunn B Munchen  
Walddparkstr. 41  
Munich  
GERMANY  
Attn: Dr. rer. nat. Horst Merbt  
(Copy No. 39)

Admiralty Marine Technology Establishment  
Teddington, Middlesex  
ENGLAND  
Attn: Dr. Allen Moore  
(Copy No. 40)

Whittle Turbomachine Laboratory  
Maddingley Road  
Cambridge  
ENGLAND  
Attn: Dr. D. S. Whitehead  
(Copy No. 41)

Whittle Turbomachine Laboratory  
Attn: Library  
(Copy No. 42)

Von-Karman Institute for Fluid Dynamics  
Turbomachinery Laboratory  
Rhode-Saint-Genese  
BELGUIM  
Attn: Library  
(Copy No. 43)

Turbine Research Department  
Rolls Royce Ltd.  
P.O. Box 31  
Derby  
ENGLAND  
Attn: Dr. D. S. Thompson  
(Copy No. 44)

NASA Lewis Research Center  
21000 Brookpark Road  
Cleveland, OH 44135  
Attn: C. Ball  
MS 5-9  
(Copy NO. 45)

NASA Lewis Research Center  
Attn: C. Feiler  
MS 501-4  
(Copy No. 46)

NASA Lewis Research Center  
Attn: Dr. M. Goldstein  
(Copy No. 47)

NASA Lewis Research Center  
Attn: W. M. McNally  
MS 5-9  
(Copy No. 48)



DISTRIBUTION LIST FOR ARL UNCLASSIFIED TM 80-188 by C. S. Lee dated  
September 15, 1980.

Cranfield Institute of Technology  
School of Mechanical Engineering  
Cranfield, Bedford MK 430AL  
ENGLAND  
Attn: Professor R. E. Peacock  
(Copy No. 49)

Iowa State University  
Mechanical Engineering Department  
Ames, IA 50010  
Attn: Dr. T. H. Okiishi  
(Copy No. 50)

NASA Ames Research Center  
Moffett Field, CA 94085  
Attn: Dr. S. Bodapati  
MA 227-9  
(Copy No. 51)

Allis-Chalmers Corporation  
Hydro-Turbine Division  
Box 712  
York, PA 17405  
Attn: R. K. Fisher  
(Copy No. 52)

NSW Institute of Technology  
School of Mechanical Engineering  
Broadway  
Sidney  
AUSTRALIA  
Attn: Professor J. P. Gostelow  
(Copy No. 53)

Naval Post Graduate School  
Department of Aeronautics  
Monterey, CA 93940  
Attn: Dr. M. F. Platzler  
(Copy No. 54)

Institute for Turbomachines  
Technical University  
Templergraben 55  
D-5100 Aachen  
Federal Republic of Germany  
Attn: Dr. H. Gallus  
(Copy No. 55)

HSVA Gmbh  
Bramfelde Strasse 164  
200 Hamburg 60  
Postfach 600 929  
Federal Republic of Germany  
Attn: Dr. E. Weitendorf  
(Copy No. 56)

J. M. Voith Gmbh  
Hydraulic Department  
Postfach 1940  
D-7920 Heidenheim  
Federal Republic of Germany  
Attn: Mr. Eichler  
(Copy No. 57)

Applied Research Laboratory  
The Pennsylvania State University  
Post Office Box 30  
State College, PA 16801  
Attn: D. E. Thompson  
(Copy No. 58)

Applied Research Laboratory  
Attn: B. E. Robbins  
(Copy No. 59)

Applied Research Laboratory  
Attn: W. S. Gearhart  
(Copy No. 60)

Applied Research Laboratory  
Attn: J. Cowan  
(Copy No. 61)

Applied Research Laboratory  
Attn: G. C. Lauchle  
(Copy No. 62)

Applied Research Laboratory  
Attn: R. E. Henderson  
(Copy No. 63)

LMED  
-8